2006

Spatial characteristics of the remotely-sensed surface urban heat island in Baton Rouge, LA: 1988-2003

Lynn Copeland Hardegree
Louisiana State University and Agricultural and Mechanical College, lynn.c.hardegree@sam.usace.army.mil

SPATIAL CHARACTERISTICS OF THE REMOTELY-SENSED SURFACE URBAN HEAT ISLAND IN BATON ROUGE, LA: 1988-2003

A Dissertation

Submitted to the Graduate Faculty of the
Louisiana State University and
Agricultural and Mechanical College
in partial fulfillment of the
requirements for the degree of
Doctor of Philosophy

in

The Department of Geography and Anthropology

by
Lynn C. Hardegree
B.S., University of South Alabama, 1996
M.S., University of Alabama, 1998
May, 2006

DEDICATION

This dissertation is dedicated to my husband, Timothy Hardegree, for his endless encouragement, sacrifice, and patience.

ACKNOWLEDGEMENTS

I owe thanks to many people whose assistance was indispensable in completing this research endeavor. First among these is Robert Rohli, my advisor and committee chair. I will forever be grateful for his support and guidance. Also, special thanks to the other members of my dissertation committee, Nina Lam, DeWitt Braud, Shih Hsu, and Juan Lorenzo, for generously giving their time and expertise.

The inspiration for doing my research came from the Urban Heat Island Pilot Project, a joint research effort of the National Aeronautics and Space Administration/Global Hydrology and Climate Center (GHCC) and the Environmental Protection Agency. I am appreciative to Jeff Luvall and Dale Quattrochi of the GHCC, as well as Maury Estes from the Universities Space Research Association (USRA), for giving me the opportunity to work as an appointee of the USRA during the very beginning stages of my research.

Special thanks to Peggy Glynn Davis of Baton Rouge Green for her assistance with my dissertation and for inviting me to participate in their K-12 educational outreach program. I continue to be amazed at her efforts to educate the community on the preservation, planting, and maintenance of trees and I wish her continued success.

I would also like to thank my previous advisors from my undergraduate meteorology studies at the University of South Alabama. To Glenn Sebastian, Associate Professor and Chair of the Department of Earth Sciences, and Aaron Williams, Associate Professor of Geography and Director of the Coastal Weather Research Center, thank you

both for your continued support and for setting such fine examples of professional geographers.

I would also like to acknowledge my graduate advisor from the University of Alabama, Luoheng Han, Professor of Geography and Director of the Center for Land Information Analysis and Mapping. My dissertation would simply not have been achievable without the knowledge I received in his Geographic Information Systems and Remote Sensing courses.

Finally, I would like to thank the two people who have contributed the most to my life, my parents - Sylvia and Lewis Copeland. Without them, none of this would have been possible.

TABLE OF CONTENTS

ABSTRACT

Our understanding of urban effects on local climate remains unsatisfactory due to several difficulties: 1) the inherent complexity of the city-atmosphere system, 2) lack of a clear conceptual theoretical framework for inquiry, and 3) the high expense and enormous difficulties of acquiring a sufficient quantity of high-quality, high-resolution (both spatially and temporally) observations in cities. Using remotely-sensed data, this study analyzes urban heat islands (UHI) that are manifested through an elevation in the surface thermal emissions within urban regions known as surface heat islands (SHI). The study area for this research endeavor is Baton Rouge, Louisiana. Whereas the surface air temperature-derived UHI did not portray an accurate representation of distinct changes in surface temperature across the study area, the remotely-sensed surface temperature-derived SHI proved to reveal microscale differences that the surface air temperature-derived UHI was unable to depict. This study also provided verification that altering amounts of vegetation within a given land cover over time can reveal changes in surface temperature values, thus providing a means to reconstruct and predict future SHIs. This was achieved through regression equations predicting surface temperatures from known NDVI values. Finally, the moist static energy parameter was evaluated to test for a better indicator of the UHI over time throughout the study area. A decreasing temporal trend in MSE was identified throughout the study period (1988 - 2003) whereas no significant linear trend occurred in air temperature. This is supported by change detection rates generated from a comparison of the 1988 and 2003 LANDSAT data sets,

as well as the range in 1988 and 2003 predicted surface temperatures (as a function of land cover).

CHAPTER 1. INTRODUCTION

1.1 PURPOSE OF RESEARCH

All too often forest stands are clear-cut in order to accommodate new development. The primary atmospheric impact from the loss of trees, an increase in the intensity of the local urban heat island (UHI), is very seldom brought to the public's attention. Nevertheless, urban effects on climate have been studied for over 200 years (Oke 1982). Luke Howard, a pioneer of urban climatology, first measured temperature differences across London as early as 1809 (Chandler 1968), but our understanding of urban effects on local climate is still unsatisfactory due to several difficulties: 1) the inherent complexity of the city-atmosphere system, 2) lack of a clear conceptual theoretical framework for inquiry, and 3) the high expense and enormous difficulties of acquiring a sufficient quantity of high-quality, high-resolution (both spatially and temporally) observations in cities.

The city has a myriad of microclimates that are intimately linked to the composition of its surfaces and the spatial and physical features of its structures (Terjung and Louie 1973). A number of investigators have provided evidence using thermal infrared remote sensor data that urban areas are strong daytime longwave radiators, but they have provided limited knowledge on the thermal energy responses contributed by discrete surfaces common to the urban landscape (Quattrochi and Ridd 1998). Understanding how thermal energy is portioned across a landscape, and the magnitude or variations in surface temperatures emanating from various landscape elements, is essential to defining the overall mechanisms that govern land-atmosphere interactions (Quattrochi and Luvall 1999). A remote sensing-based energy approach would be ideal in establishing a link between the surface temperature and microscale climate variability,

and would assist in overcoming the traditional difficulties in UHI analysis described in (1) through (3) above.

Although the fundamental input in urban climatology is energy, most climatological studies have focused on the output manifestations of this energy, particularly air temperature. For example, typical urban surfaces, such as concrete and asphalt, are much hotter than vegetated surfaces during the day. As these surfaces store energy during the day and release it at night, a dome of warmer air will persist over the urban area. This dome of air that is warmer than that of the surrounding countryside is known as the UHI. Thus, the daytime heating characteristics are important to understand because they drive the nocturnal peak influence of the UHI.

Several researchers have analyzed the diurnal changes in the UHI. In the case where both daytime and nighttime air temperatures were analyzed, some studies found that the UHI has similar trends regardless of time of day (Saaroni *et al.* 2000). However, other studies have found that the relative magnitude of the UHI during daytime and nighttime hours and the vertical extent of these anomalies differ (*e.g.*, Oke 1979, Noto 1996). In a study of San Francisco, the nocturnal urban air temperature anomalies are 3-5 C^o compared to 1 C^o daytime anomalies, yet the vertical extent of these anomalies is only 2 to 3 times building height at night as compared with over a kilometer during the day (Ducksworth and Sandberg 1954).

The UHI effect is particularly notable in the daytime surface temperature (Landsberg 1976), which is not identical to air temperature. Despite the fact that turbulent mixing of the atmosphere tends to obscure the influence of urban-rural daytime surface temperature differences in air temperatures, the net daytime urban impact on the atmosphere is large (Goward 1981). For example, urban daytime values of surface-emitted longwave radiation were 15-20 percent (130 Wm^{-2}) greater than corresponding rural values in Montreal (Landsberg and Maisel 1972) while,

for the same study area, urban nocturnal values of surface-emitted longwave radiation were only 5 percent (20 Wm^{-2}) greater than corresponding rural values (Oke and Fuggle 1972).

The impact of the daytime UHI is important because of its influence on other atmospheric phenomena, such as precipitation, which has been shown to increase by about 5-30 percent on an annual basis as a result of the UHI, with the maximum effect usually located within a few tens of kilometers downwind of the urban area (Jager 1983). Furthermore, in general, urban effects on frequencies of precipitation days are more apparent than on precipitation totals (Choi 1998). Besides precipitation, daytime modifications to temperature, humidity, and clouds may persist to as far as 100 km downwind, a much greater distance than at night (Jager 1993).

The impact of increased daytime urban surface temperatures can be devastating to the local population and has been the subject of UHI-related research. Increased temperatures during the daytime hours have a greater impact on both human health and comfort, as compared to increased nocturnal temperatures. For example, the mid-July 1995 heat wave in the central and eastern U.S. caused 830 deaths nationally with 525 of these in Chicago (Changnon *et al*. 1996). Outside laborers work during the hours of maximum temperatures where prolonged exposure to increased temperatures can be instrumental in the incidence of strokes, heart disease, and pulmonary disorders (Schuman *et al.* 1964).

Increased temperatures, particularly during the daytime, also contribute to increased air conditioning usage, thus raising the local energy demand and cost. In general, people use their air conditioners when the average daily air temperature exceeds 23ºC. Therefore, a cooling degree-hour (CDH) is defined as each 60-minute period that the outside temperature exceeds 23ºC by one degree (Grosskopf 2003). For example, if in a given hour, the mean hourly temperature was 35ºC, 12 CDHs would have accumulated for that hour. Running totals of CDHs

are calculated for days, months, and summer seasons. In a study to evaluate spatial variability of the CDHs over the urban landscape of Phoenix, Arizona, it was determined that different land cover types induced spatial differences of summer CDHs. In fact, the calculated energy demand was comparable to general circulation model projections of climate change for the region (Brazel *et al.* 1993).

The UHI is also worthy of investigation because of its contribution to global warming datasets. Jones *et al.* (1986) produced a gridded temperature dataset that has been widely used to analyze and identify the UHI signal in the global temperature record. Jones *et al.* (1990) concluded that the global urban warming bias is between 0.01 C^{o} and 0.10 C^{o}. If the high-end estimate is correct, the UHI bias represents nearly 25 percent of the global warming of the past century (Balling 1992). Therefore, an improved understanding of the characteristics of this warming is warranted.

While the term "global warming" is used to describe the observed surface air temperature increase in the 20th century, the concept of "warming" actually includes increases in both sensible and latent energy (energy absorbed or released during phase changes of water). Thus, although temperature alone may be an incomplete indicator of surface heat content since it only represents changes in sensible energy (Pielke 2003), temperature nevertheless represents an important component of the UHI. However, moist static energy (MSE, or surface heat content) may be the more appropriate metric to assess surface global warming (Pielke 2003). Given that increased heat storage within the urban fabric may be driven mainly by enhanced daytime surface heating, which occurs because of surface dryness (Carlson *et al*. 1981), a temporal evaluation of the MSE may offer an improved indication of the UHI intensity over time.

To evaluate the UHI accurately, numerous atmospheric measurements must be made simultaneously over the study area. For a climatological investigation of this relationship, a conclusive *in situ* measurement network must be available to supply the historical data required to study atmospheric temperature and MSE trends. Regardless of the availability of these data, the spatial resolution of the network may not provide detailed data capable of identifying areas of increased emitted surface heat between the monitoring stations within the complicated mosaic of the urban surface. Furthermore, *in situ* observations do not provide a reliable indicator of the thermal properties of distinct surface features due to the height of air temperature measurements. However, because radiant emissions from surfaces can be measured from airborne or satellite platforms, this larger number of observations enables the thermal properties of small surface features to be measured, allowing for a high-resolution investigation of urban microclimates, if the non-temperature-related effects of changes in MSE can be held constant.

1.2 OBJECTIVES AND HYPOTHESES

This study relies on the theoretical premise that increases in surface thermal emissions are directly related to increases in near-surface atmospheric temperatures, a relationship that weakens with height (Carlson *et al*. 1977). Even though UHIs can be measured as either atmospheric or surface phenomena, this study will analyze the heat islands that are manifested through an elevation in the surface thermal emission of urban regions known as surface heat islands (SHI, Roth *et al.* 1989) using remotely-sensed data. Therefore, objectives of this study are:

1. To determine whether surface air temperature and MSE depict a similar temporal pattern of UHI-related warming.

2. To compare the spatial pattern of a surface air temperature-derived UHI (assuming that temperature provides an adequate means of representing the UHI) to a remotely-sensed, surface temperature-derived SHI.
3. To compare the spatial resolution of a surface air temperature-derived UHI to a remotely-sensed, surface temperature-derived SHI.
4. To identify regression equations for predicting surface temperature based on vegetative cover, represented by the Normalized Difference Vegetation Index (NDVI), for various land cover categories, and to use these derived relationships to identify the extent of the UHI in the past and to forecast UHI intensity in the future under various deforestation scenarios.
5. To provide an exploratory analysis to quantify the contribution of deforestation to increasing surface temperature within the urban environment, by determining a "thermal efficiency" of urban land features, using a case study approach.
6. To provide an exploratory analysis to quantify the contribution of increasing tree canopy to mitigating surface temperature, using a case study approach.

Hence, the research hypotheses are:

1. A temporal evaluation of the MSE of surface air will provide a more appropriate indicator of the UHI presence over time than surface air measurements.
2. The spatial pattern of the remotely-sensed, surface temperature-derived SHI will be similar to the surface air temperature-derived UHI.
3. The spatial resolution of the remotely-sensed, surface temperature-derived SHI will reveal microscale differences that the surface air temperature-derived UHI is unable to depict.

4. Altering amounts of vegetation within a given land cover over time will reveal changes in surface temperature values, thus providing a means to reconstruct and predict future SHIs.

1.3 GENERAL OVERVIEW OF DATA AND STUDY AREA

This study uses a combination of remotely-sensed and *in situ* data to evaluate the UHI of Baton Rouge, Louisiana. Baton Rouge sits on the east bank of the Mississippi River in south central Louisiana at 30°27'29"N, 91°8'25"W, and occupies approximately 200 km^2 of East Baton Rouge Parish (1225 km^2). Baton Rouge is chosen because it represents a medium-sized Sunbelt city that has experienced steady, moderate growth over the past 20 years. Furthermore, the relative "greenness" of East Baton Rouge Parish, with 45 percent of the parish covered by tree canopy (Ball 2003), suggests that deforestation and other land cover changes may have great potential to alter temperatures in the future.

Airborne and satellite multispectral data were collected from the Advanced Thermal and Land Application Sensor (ATLAS) and LANDSAT satellites, respectively. GIS mapping data and color infrared orthophotography of Louisiana are acquired from the Louisiana Oil Spill Coordinators Office (LOSCO). Meteorological data from the Louisiana Department of Environmental Quality and the Baton Rouge area network of automated and Cooperative Observer Program (COOP) weather stations are also utilized.

1.4 METHODOLOGY OVERVIEW

Various aspects of the UHI of Baton Rouge, Louisiana, are evaluated in this study. The utilization of a surface heat content parameter is explored as a means to evaluate the nature of

surface warming more accurately, by identifying long-term trends in both surface air temperature and MSE at the Baton Rouge Metropolitan Airport. Then, the spatial pattern and resolution of the remotely-sensed, surface temperature-derived SHI are compared to that portrayed by the less-spatially-complete surface air temperature-derived UHI. From the 1998 ATLAS dataset, surface temperature is analyzed as a function of land cover and corresponding NDVI values for each land cover are calculated. Regression equations are derived for each land cover type based on coincident NDVIs and surface temperature values. These equations are then used to estimate surface temperatures for the same land cover types based on NDVIs calculated from 1988 and 2003 LANDSAT datasets collected over the same location. As the amount of vegetation within the study area changes over time, corresponding surface temperature values will also be altered, thus revealing changes in the spatial extent and intensity of the SHI over time. Case studies, both within the study area, investigate the thermal efficiency of urban land use and the potential impact of tree growth to the SHI over time.

1.5 OUTLINE OF THE DISSERTATION

This dissertation is organized as a series of chapters referred to as the "traditional style". Chapters 2 through 5 consist of the literature review, methodology, results, and conclusions, respectively. Chapters 6 and 7 consist of case studies, each containing their separate methodologies, results, and conclusions.

CHAPTER 2. BACKGROUND: LITERATURE REVIEW AND REMOTE SENSING THEORY

2.1 GENERAL CHARACTERISTICS OF URBAN HEAT ISLANDS

Urban heat islands (UHIs) are convex domes of relatively warm air emanating from the urban fabric of concrete and steel (Ford 1979). While many factors contribute to the UHI, a primary causative factor is the deforestation and replacement of the land surface by materials that are largely impervious and do not return as much water to the atmosphere as the natural surface (Lo *et al.* 1997). Impervious surfaces concentrate the receipt of solar radiation at the surface and may minimize the transfer of such energy upward (through reflection and convection), downward (through conduction), or laterally (through advection and conduction).

The UHI has long been the subject of much site-specific research. Since Howard's 1809 (Chandler 1968) original studies on the urban climate of London, many studies have concentrated on some aspect of land cover as it relates to local UHI formation and characteristics.

2.1.1 The Role of Land Surfaces

Modification of the urban climate results from concentration of population, the expansion of living space onto, above, and under the ground, and the modification of earth's surface constituent materials (Yamashita and Sekine 1991). These modifications, or land-cover changes within urbanized areas, comprise a major component of regional and local warming. For example, during the twentieth century over an area extending from east of the Cordillera in northwestern Canada to Texas, long-term surface temperature increases have been observed where extensive land-cover changes (such as the clearing of forests) have occurred (Skinner and

Majorowicz 1999). Kalnay and Cai (2003) estimated that over the past fifty years in the continental U.S., land-cover changes have resulted in a 0.27 Cº mean surface warming per century, which is at least twice as high as previous estimates based on urbanization alone. Narisma and Pitman (2003) observed similar impacts of land cover change on increases in local maximum air temperatures throughout regions of Australia. Other studies have also analyzed the impact of changing land surfaces on local UHIs (Kim 1992, Quattrochi and Ridd 1994, Asaeda et al. 1996, Schlatter and Wilson 1997, Condella 1998, Unger et al. 2001, Belaid 2003, and Weng 2003). In general, these studies suggest that changing land surfaces can cause increases in local temperatures on the order of 1.67-2.22 Cº for large urban areas in summer to 5.6 Cº for large urban centers in winter, in comparison with the surrounding countryside. Although literature exists on the impact of deforestation on global temperature, a review of that literature is beyond the scope of this dissertation. Furthermore, little research has isolated the contribution of global deforestation for urbanization to global temperature rise.

Other studies have examined the impact of land cover change on the UHI in terms of thermal properties other than temperature. For instance, the impact on local albedo, heat conductivity, and thermal capacity of the surface following the replacement of farms and fields with buildings and roads has been examined for northern China by Zhao and Zeng (2002), for New Orleans by Sailor and Fan (2002), and for an idealized maritime city by Atkinson (2003). Collectively, these studies show that the building materials of the urban environment are very effective at absorbing solar radiation and re-radiating energy back into the lower levels of the atmosphere, thus raising the temperature of the surrounding air. Much work remains to be done on the impacts of albedo, heat conductivity, and thermal capacity on local, regional, and global scales.

In addition, the heterogeneity and complexity of composition, pattern, and spatial extent of the mosaic of land covers in the urban area have also been noted as contributors to the local UHI characteristics in London (Clarke and Peterson 1972), Hokkaido, Japan (Shudo *et al.* 1997), Germany (Blankenstein and Kuttler 2004), and Hong Kong (Giridharan 2004). Chandler (1968) noted that the mosaic of land surfaces also indirectly affects the UHI because of changes in the local airflow patterns that occur with a reduced diffusion of heat from paved surfaces and courtyards, and the anthropogenic waste heat generated from industrial and domestic activities. Chandler's pioneering research was supplemented by work by Wong and Dirks (1978) on local airflow modifications in St. Louis, Missouri, by Comrie (2000) in Tucson, Arizona, by Lemonsu and Masson (2002) in Paris, and by Fujibe (2003) in Tokyo. Subsequent studies have also verified and elaborated on Chandler's statements on the impact of paved surfaces (Asaeda and Ca 1993, Chudnovsky *et al.* 2004) and waste heat (Fedotov 1991, Saitoh *et al.* 1996, Ca *et al.* 1999, Khan and Simpson 2001, Chen *et al*. 2003, Hinkel *et al.* 2003, Fan and Sailor, 2005) on the urban heat island intensity. To some extent, all of the above thermal variables contribute to elevated surface temperatures over urbanized areas. Collectively, then, the distinction between urban and nonurbanized biophysical environments "…is a function of their relatively different surface structure, which ultimately affects the climate over these areas" (Quattrochi and Ridd 1998). Literature isolating the impacts of urban land cover heterogeneity on regional- and global-scale heat/energy and motion in the climate system is particularly sparse, perhaps because approximately 70 percent of the Earth's surface is covered by the homogeneous ocean. However, studies at various scales have collectively shown that cities, in relation to their impact on local and regional climates, are not monolithic surfaces of pavement and buildings (Quattrochi and Ridd 1998). Indeed, each land cover type potentially has its own atmospheric

energy budget characteristics. Urban energy budget studies are fundamental to the understanding of the casual mechanisms behind the UHI (Sakakibara 1996, Arnfield 1998). Therefore, the UHI is primarily the result of the alteration of land surfaces, which affects the heat balance of the urbanized space.

2.1.2 The Role of Water

Another important factor impacting the UHI is water. The movement of water from the subsurface and surface to the atmosphere is an important control of the UHI because that portion of the surface-absorbed solar radiant energy that is converted into latent heat (*i.e.*, energy "used" to evaporate water or to melt or sublimate ice) cannot be used to raise the temperature as "sensible heat". Indeed, evaporation is the only process that is a component of both the energy balance equation and the water balance equation. Several studies have analyzed the role of the hydrologic cycle in the atmospheric energy balance over urban locations such as Jerusalem, Israel (Shafir and Alpert 1990), and Mexico City (Oke *et al*. 1999). Collectively, these studies suggest that the amount of energy involved in latent heating is dependent on the availability of water at the surface to drive the evaporation process.

2.1.3 The Role of Vegetation

Vegetation has a direct correspondence with the radiative, thermal, and moisture properties of the Earth's surface that determine land surface temperatures (Weng *et al*. 2004). Whereas the climate exerts the dominant control on the spatial distribution of the major vegetation types on a global scale, vegetation cover in turn affects local and regional climate via alteration of the physical characteristics of the land surface (Brovkin 2002). Because plants can

move water effectively from the subsurface to the atmosphere via transpiration, vegetation is efficient at maximizing the conversion of incoming energy to latent heat and minimizing sensible heating. Because a sparse and/or decreasing canopy cover can be especially problematic in a rapidly-growing metropolitan area, it is recommended that cities set a canopy goal of 40 percent overall, which is the equivalent of 20 large trees per acre (Moll 1997).

Through a combination of shading and evaporative cooling, vegetation can be used to mitigate some of the anthropogenic heating and polluting effects generated by the development of urban areas (*e.g.*, Grimmond *et al*. 1996, Ca *et al*. 1998, Spronken-Smith and Oke 1998). For example, as long as trees are actively growing, their rate of CO_2 sequestration through photosynthesis exceeds their release of that gas through respiration, and the net result is a reduction of CO_2 in the atmosphere (McPherson 2000), thereby mitigating the anthropogenically-enhanced greenhouse effect. However, the link between vegetation and available water cannot be underestimated. Indeed, without water, trees cannot transpire and the foliage can actually contribute to an increase in air temperature (Laverne and Lewis 2000).

Vegetation has other impacts on the local urban atmosphere, such as in the minimization of local heating and cooling requirements of buildings (*e.g.*, Heilman and Gesch 1991), dispersion and filtering of pollutants (Rao *et al*. 2004), and storm water management (Avissar 1996). For example, in Atlanta, the 60 percent loss of the natural tree cover over the last 20 years has caused a $2 billion increase in storm water management costs (Moll 1997). In Baltimore, it was determined that a neighborhood with 40 percent tree cover could reduce storm water runoff by about 60 percent more than a neighborhood without trees (Moll 1997). Even though vegetation can affect the wind and precipitation regime of urban areas which can in turn affect thermal properties, little scholarly research has quantified these relationships.

2.1.4 The Role of Population

The holistic impacts of surface cover, water, and vegetation discussed above have *climatological* in addition to *meteorological* implications on the urban atmosphere at various scales, and all of these factors are tied to population growth and impacts. There is no question that population growth impacts local climatology (Tso 1996, Jauregui *et al*. 1997, Tayanc and Toros 1997, Brandsma *et al*. 2003, Chung *et al*. 2004, Mihalakakou *et al*. 2004, Stallings 2004, Zhou 2004). UHI intensity tends to increase with increasing city size and/or population (Park 1986, Yamashita *et al*. 1986, Jones *et al*. 1989, Chow 1992, Hogan and Ferrick 1998, Magee *et al*. 1999, Philandras *et al*. 1999, Torok *et al*. 2001, Hinkel *et al*. 2003) and as cities grow, they increasingly contribute to climate change at scales beyond just locally. For North American and European cities, Oke (1973) developed a regression model that successfully explained 97 percent of the variability in UHI intensity with the single predictor variable of population size. An analysis of urban temperature changes in the U.S. based on population (Karl *et al*. 1988) showed a local increase of approximately 1 C° per 100,000 people due to urbanization. Also at the regional scale, Kukla *et al*. (1986) noted a rise of 0.12 C° per decade in U.S. urban temperatures between 1941 and 1980. More recent studies corroborate these pioneering studies. For example, in a model to predict future warming for cities of 200,000 or more in the U.S., Viterito (1991) predicted that a warming of 0.19 C° will accompany population growths through the year 2035.

2.2 UHI AND CLIMATE CHANGE

It could be argued that UHIs represent the most significant form of irreversible anthropogenically-forced climatic change (Arnfield 2003) not only at the local scale, but also at regional and even global scales. As humans alter the character of the natural landscape in the

city-building process, the long-term local energy exchanges that take place within the boundary layer are affected. Modification of the landscape through urbanization alters the natural channeling of energy through the atmospheric, terrestrial, and hydrological systems (Pinho and Orgaz 2000, Khan and Simpson 2001, Dixon and Mote 2003, Rozoff *et al*. 2003). Surface conditions, natural or human-made, are of paramount importance in the atmosphere's various energy budgets and by changing these conditions, people have inadvertently affected atmospheric properties (Chandler 1976). This is especially true in the surface boundary layer (SBL) where motions and properties of the air are closely controlled by the nature of the Earth's surface. Therefore, modification of the landscape influences the local (micro) scale, mesoscale, and even the macroscale climate through a "cascade of linkages" (Terjung 1976). It has even been suggested that global warming may be "…attributable not to the greenhouse effect but to the heat island effect caused by increased urbanization of areas where temperatures are recorded" (Hudson 1996). Although Hudson's assertion may be overstated, some of the regional and global temperature rise of the past 100 years can be attributed to the warming associated with the buildup of cities (Balling 1992).

Although regional and global-scale impacts of UHIs are significant and worthy of further investigation, this research will only examine impacts of local land-use changes on the local UHI of Baton Rouge, Louisiana. Therefore, henceforth, only the techniques associated with analysis of local UHIs will be examined.

2.3 CASE STUDIES OF THE LOCAL UHI USING REMOTE SENSING

Site-specific studies have increasingly utilized remote sensing and GIS modeling techniques to analyze the local UHI in recent years (*e.g.*, Vukovich 1983, Balling and Brazel

1988, Weng 2001, Streutker 2002, Xu and Chen 2004). Remote sensing has been used over urban areas to assess the magnitude of the UHI (Johnson 1994, Nichol 1996, Weng 2003), perform land cover classifications related to the UHI (Kim 1992, Lo and Quattrochi 2003, Hawkins *et al*. 2004, Weng and Yang 2004), and provide input for models of urban surface-atmosphere exchange (Hafner and Kidder 1999, Borghi *et al*. 2000, Hirano *et al*. 2004).

Simulation of urban-rural land surface climate processes using boundary layer climate models requires accurate input of surface thermal and radiative remote sensing data. For example, when tested through a spatial surface energy balance simulation of an urban-rural landscape in eastern Nebraska, incorporation of satellite-derived surface physical parameters greatly improved the simulation of spatial land surface climate processes (Yang 2000).

In a review of thermal remote sensing in the study of urban climates, Voogt and Oke (2003) noted that:

> "Improvements in the spatial and spectral resolution of current and next-generation satellite-based sensors, in more detailed surface representations of urban surfaces and in the availability of low cost, high resolution portable thermal scanners are expected to allow progress in the application of urban thermal remote sensing to study the climate of urban areas."

Thermal remote sensing at a spatial resolution capable of delineating streets, roofs, and walls permits definition of yet another UHI in addition to the urban boundary layer (UBL) and urban canopy layer (Oke 1976), namely that of the ground surface (Arnfield 2003). At such resolution, multiple UHIs exist and display different atmospheric characteristics that are controlled by different assemblages of energy exchange processes (Terjung and Louie 1973, Aniello *et al*. 1995, Bottyan and Unger 2003, Dousset and Gourmelon 2003). As noted by

BenDor and Saaroni (1997) in Tel Aviv, Israel, very high thermal and spatial resolution will allow for the depiction of surface microstructures and therefore the delineation of microclimates.

Remote sensing of local UHIs has traditionally used a variety of vegetation indices to estimate the land surface temperature-vegetation relationship (Gallo *et al*. 1993, Friedl and Davis 1994, Gallo and Owen 1999, Gallo *et al*. 2002). In fact, urban and rural differences in normalized data vegetation index (NDVI) have generally explained an even greater amount of the variation observed in temperature differences than past analyses that utilized urban population data alone (Gallo *et al*. 1993). Several studies have shown the inverse relationship of local vegetation cover to surface temperature using NDVI (*e.g.*, Nichol 1994, Gallo and Tarpley 1996, Owen *et al*. 1998, Quattrochi and Ridd 1998). Results from all of these studies depend upon theoretical decisions in remote sensing methodology. The selection of inappropriate collection parameters, inadequate classification schemes, and/or incorrect analysis processes would compromise the accuracy of their conclusions.

2.4 THEORETICAL PRINCIPLES IN REMOTE SENSING

Because thermal remote sensing principles are indispensable in this dissertation, it is essential that these principles be reviewed here. In its simplest definition, remote sensing is the capture of data about an object without physically touching that object. Remote sensors measure electromagnetic radiation (EMR) returned by the earth's natural and cultural features. Aerial photography and satellite imagery are both forms of passive remotely-sensed data, meaning that they merely monitor and record EMR from other sources (*i.e.*, the earth's surface and the sun) rather than produce their own energy (such as in radar and sonar).

EMR is energy transmitted through space, in a direction perpendicular to the direction of propagation, in the form of electromagnetic waves that vary in several important characteristics (discussed below) (Figure 2.1). Both electric and magnetic waves travel in a harmonic sinusoidal pattern at the speed of light where the frequency (υ) of a wave – the number of peaks passing a fixed point in space per unit time (s^{-1}) is inversely proportional to its wavelength (λ) – the distance between successive wave peaks (m). Specifically,

$$C = \upsilon * \lambda$$

where c = the speed of light, 2.998*108 m s^{-1}

In remote sensing, the most common way to characterize electromagnetic waves is by their wavelengths. The electromagnetic spectrum (EMS) represents the continuum of EMR from shortest to longest wavelengths (Figure 2.2). In this example, wavelengths are measured in micrometers (μm), or millionths of a meter (1 μm = 10^{-6} m). All types of land cover (rock types, water bodies, vegetation, man-made structures, *etc.*) absorb EMR along a particular portion of the EMS. Thus, each land cover type possesses a distinguishable signature of EMR. Each remote sensing device is designed to monitor EMR from a specific portion of the EMS. The near-infrared and middle-infrared regions of the EMS are sometimes referred to as the shortwave infrared region (SWIR). Thus, this area is distinguished from the thermal region, which is often referred to as the longwave infrared region (LWIR).

Incident radiation (E_I) is the total flux density of energy (in W m^{-2}) that strikes the surface of the earth. When EMR interacts with the earth's surface, one of three reactions occurs: it is reflected (P_λ), absorbed (α_λ), or it is transmitted (T_λ). Therefore,

$$(E_I) = P_{(\lambda)} + \alpha_{(\lambda)} + T_{(\lambda)}$$

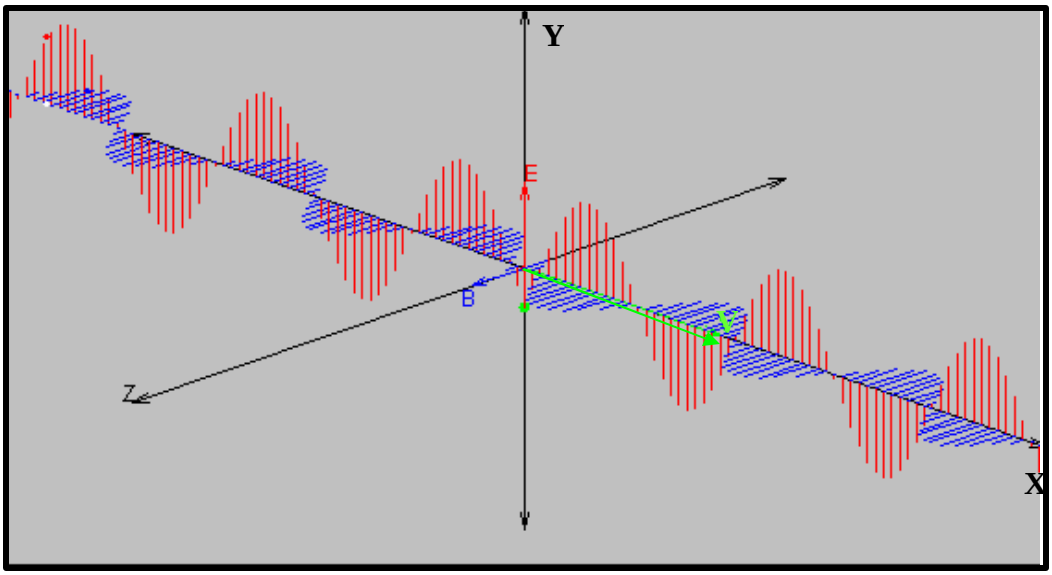

Figure 2.1: Propagation of Electromagnetic Wave
Electric Field (E), Magnetic Field (B), and Velocity Vector (V)
(Hwang 2004)

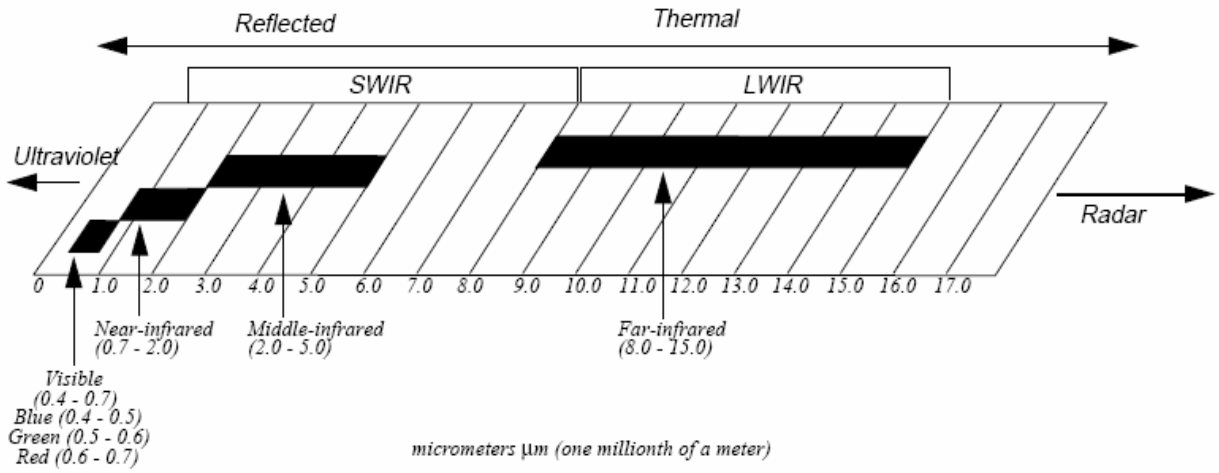

Figure 2.2: The Electromagnetic Spectrum (Suits 1983)

To distinguish land cover types or classify features within image data, it is necessary to understand how vegetation, soils, water, and other land covers reflect and absorb EMR. Differences in reflection and absorption amounts make it possible to identify and assess a broad

range of surface features and their conditions. When sunlight (the illumination source for SWIR imagery) strikes a target, wavelengths that are neither absorbed nor transmitted are reflected back to the remote sensor. Measured shortwave reflectance values are reported as discrete digital numbers (or digital values) recorded by the sensing device and represent the degree of efficiency of reflection from the source object. These grayscale values fit within a certain bit range, such as 0 to 255, which is 8-bit data. The use of SWIR imagery for target discrimination, whether the target is mineral, vegetation, cultural, or even the atmosphere itself, is based on the reflectance spectrum of the material of interest. Every material has a characteristic spectrum based on the chemical composition of the material.

The ability of a surface to absorb incident energy is also an important means of identifying objects remotely, and this feature depends on the chemical composition of the material. As an object absorbs energy, the object's temperature will increase and it will radiate (emit) longwave EMR back into the atmosphere. Remote sensing devices capable of imaging the LWIR measure the emitted energy of an object and record this value as a digital number. All matter at temperatures greater than absolute zero (0 Kelvin, -273.16°C, or –459.69°F) continuously emits EMR.

Blackbodies are objects that act as perfect absorbers and emitters of EMR. However, the degree to which an object behaves as a blackbody may be wavelength-dependent. For example, atmospheric gases tend to display blackbody features at selective wavelengths; such gases behave as discontinuous emitters/absorbers of EMR. All EMR incident on a blackbody (at that wavelength) is re-emitted back into the atmosphere. Because Kirchoff's Law states that perfect absorbers are also perfect emitters, a direct relationship exists between the temperature of a

blackbody and the intensity of EMR that it emits. Planck's Radiation Law gives the spectral radiance of a blackbody ($E_{?B}$) as a function of its temperature:

$$E_{lB} = \frac{c_1}{l^5 \left(\exp^{\frac{c_2}{lT}} - 1 \right)}$$

where, c_1 = 3.74×10^8 W m^{-2} μm^4, which is twice the value of the product of Planck's Constant and the square of the speed of light

c_2 = 1.44×10^4 K μm, which is the product of Planck's Constant and the speed of light, divided by the Stefan-Boltzmann Constant

T is Kelvin temperature

and $E_{?B}$ is in W m^{-2}, at wavelength ? (in μm).

Therefore, remote sensing techniques can use monochromatic radiance or irradiance to infer the surface temperature of a blackbody. According to Stefan-Boltzmann's Radiation Law, the total amount of energy emitted from a blackbody (E_B) increases very rapidly with the blackbody's temperature:

$$E_B = \int_0^\infty E_{lB} \, dl = s \, T^4$$

where E_B = the full spectrum blackbody emittance (W m^{-2})
σ = the Stefan-Boltzmann constant 5.67×10^{-8} m^{-2} K^{-4}
T = Kelvin temperature

Therefore, full-spectrum emittance of a blackbody (detected via remote sensing techniques) can also be used to infer the surface temperature of that body. While most surfaces are not blackbody emitters, at any wavelength they emit some fraction of the amount of thermal radiation that a blackbody would emit. This ratio between emittance from an object in relation to emittance from a blackbody object at the same temperature fraction is known as emissivity (e).

Therefore, blackbody emitters have an e equal to 1 at the wavelength(s) in which they behave as blackbodies, and all other objects have $0 \leq e \leq 1$. Because the Stefan-Boltzmann Radiation Law only holds true for blackbodies, an extension of this equation is needed to correct for all other objects. Specifically,

$$M = e\, s\, T^4$$

where M represents the total radiant emittance of a non-blackbody (in W m^{-2}). Thermal remote sensing devices record M, and therefore indirectly measure the object's radiant (apparent) temperature. To convert this apparent temperature (T_{rad}) into a kinetic (internal) temperature (T_{kin}), the extension of the Stefan-Boltzmann Radiation Law is commonly represented as:

$$T_{kin} = T_{rad}\, e^{-\frac{1}{4}}$$

As LWIR emitted upward by the earth travels through the atmosphere, some of it is entirely absorbed by atmospheric gases and some of it travels through the atmosphere largely unaffected. The wavelength regions of the EMS away from the absorption bands of the atmospheric gases are most useful for measuring surface emission. These transparent regions are known as atmospheric windows. The 8-13 µm region of the EMS is of particular interest since it not only includes an atmospheric window, but also contains the peak energy emissions for most surface features. Emissivity is considered to be constant for a given object in this wavelength region.

The balance between energy absorbed by an object and energy radiated and reflected back into space is fundamental in determining how warm or cool an object's surface becomes. From a radiation standpoint, albedo is the ratio of the EMR reflected from an object to the total

amount incident upon it, for a particular wavelength of the EMS. Albedo ranges between 0 (no reflectance) and 1 (complete reflectance). As the earth's surface constantly changes as a result of phenology, snowfall, moisture changes, urbanization, and other forms of non-natural land use change, so does the albedo of the earth surface. An increase of energy absorption at the surface (low albedo), and therefore increase of energy emittance, corresponds to an increase in surface temperatures.

2.5 CHAPTER SUMMARY

In this chapter, previous studies on the causes of the UHI, and impacts of the UHI at local, regional, and global scales were reviewed, along with those that utilize remote sensing technology and theory to characterize the local UHI. Theoretical principles involved in such remote sensing technology were then reviewed, because these principles are to be used in the next chapter, which describes the data and methods utilized for analyzing the properties of the SHI in Baton Rouge, Louisiana.

CHAPTER 3. DATA AND METHODS

3.1 DATA OVERVIEW

To address the hypotheses listed in Chapter 1, airborne and satellite multispectral data are collected from the Advanced Thermal and Land Application Sensor (ATLAS) and LANDSAT satellites, respectively. Meteorological data from the Louisiana Department of Environmental Quality (LDEQ) and the Baton Rouge area network of automated and Cooperative Observer Program (COOP) weather stations are also utilized. GIS mapping data and color infrared orthophotography of Louisiana are acquired from the Louisiana Oil Spill Coordinator's Office (LOSCO). A detailed description of additional data required and methodology employed for each case study is discussed in the specific case study chapters, Chapters 6 and 7.

3.1.1 Airborne Multispectral Data

The airborne imagery utilized in this study was acquired by Lockheed Martin Stennis Operations as ATLAS Mission M9811. The objective of the mission was to collect medium-resolution ATLAS imagery over the entire Baton Rouge, Louisiana, study area (Figure 3.1). NASA's Stennis LearJet 23 housed the ATLAS (Figure 3.2). The data were collected for the Global Climate and Hydrology Center (GCHC) at NASA's Marshall Space Flight Center in Huntsville, Alabama, between 1538 and 1937 GMT on 11-12 May 1998. Three flights comprising 23 flight lines were flown at 5.0 km above ground level (AGL) to acquire 10-m data. Of the 23 flight lines flown, 21 were acquired on 11 May 1998 and the remaining two flight lines were collected the following day (Table 3.1). Weather conditions during the flights are discussed in Section 3.2.2.

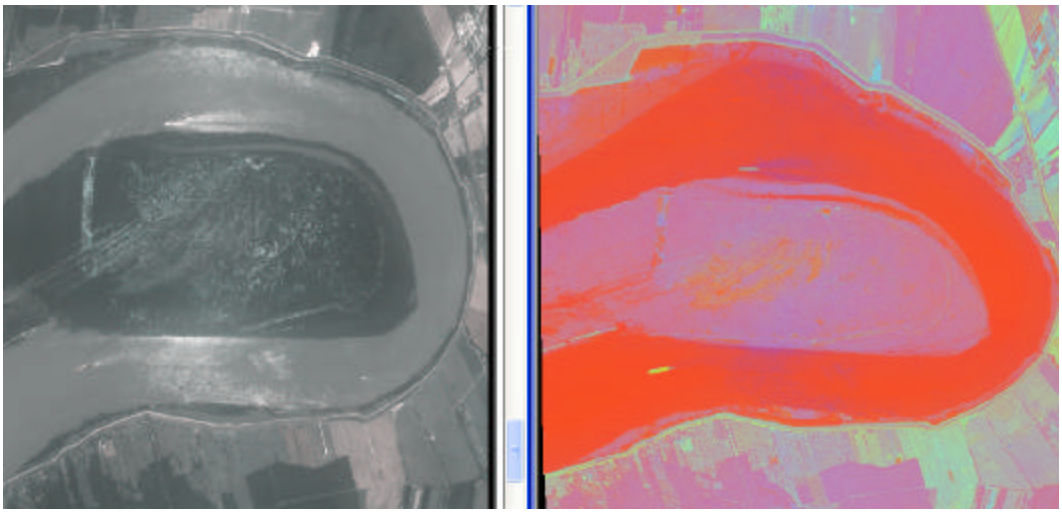

Figure 3.1: Example of the Visible (left) and Thermal Infrared (right) Images of the Baton Rouge Dataset

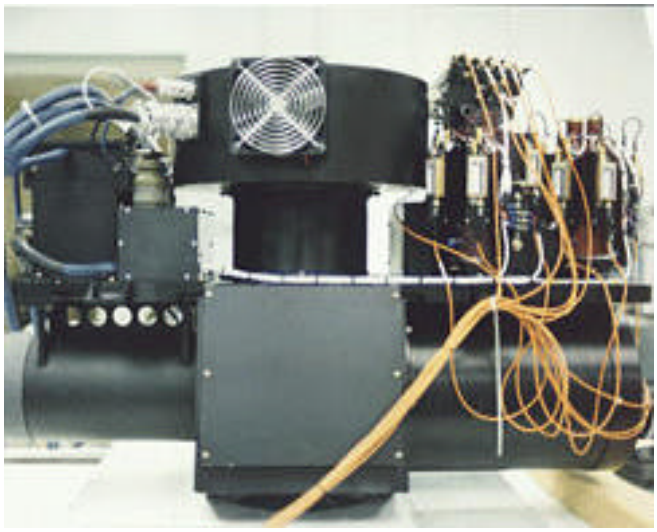

Figure 3.2: Side View of the ATLAS Scanner (Luvall et al. 2005)

Table 3.1: ATLAS Flight Lines over Baton Rouge, LA

Flight	Day	Time (GMT)
1	05/11/98	15:38 -17:04
2	05/11/98	17:56 -19:37
3	05/12/98	15:55 -16:36

The ATLAS is a 15-channel imaging system with a spectral range of 0.45 – 12.2 μm (Table 3.2). The sensor collects multispectral radiation channels across the thermal (Figure 3.3), near infrared, and visible (Figure 3.4) portions of the electromagnetic spectrum. Its spatial resolution can range between 2.0 - 20 m, depending on altitude, and senses at approximately a 30 degree swath width to each side of the aircraft. The ATLAS sensor collects 640 pixels with three additional calibration source pixels per line at a rate of 6-50 scans per second. The position and orientation of the aircraft and the sensor orientation are all recorded at least once per second. For geometric corrections, an internal Global Positioning System (GPS) with a 1.5 m root mean square accuracy (corrected) is utilized. Ground data collection at the time of the overflights included the establishment of GPS ground control points, surface temperature measurements at selected sites throughout the city, and concurrent radiosonde launches.

Prior to analysis of the ATLAS data, the data are first processed through known algorithms for initial georeferencing. Raw data collected by the sensor in 8 bit digital numbers (DN) are corrected for the attenuation effect of the atmosphere. This is achieved by applying the MODTRAN4 program developed by the United States Air Force Geophysics Laboratory, which estimates atmospheric transmittance and radiance for a given atmospheric path at moderate spectral resolution over the operational wavelength region (Berk *et al*. 1999). The wavelength region ranges from 0.25 to 28.5 μm and is calculated in $1cm^{-1}$ frequency intervals. The input parameters for the MODTRAN4 program are the radiosonde data of atmospheric profiles collected during the ATLAS overflights.

The data are calibrated to produce accurate temperature measurements. This is achieved by using onboard low and high temperature blackbodies, which were referenced at the beginning and end of each scan line. With known emittance values for blackbodies, Planck's Law is

Table 3.2: ATLAS Channels

Channel	Band width limits (μm)
1	0.45 – 0.52
2	0.52 – 0.60
3	0.60 – 0.63
4	0.63 – 0.69
5	0.69 – 0.76
6	0.76 – 0.90
7	1.55 – 1.75
8	2.08 – 2.35
9	3.35 – 4.20
10	8.20 – 8.60
11	8.60 – 9.00
12	9.00 – 9.40
13	9.60 – 10.2
14	10.2 – 11.2
15	11 .2 – 12.2

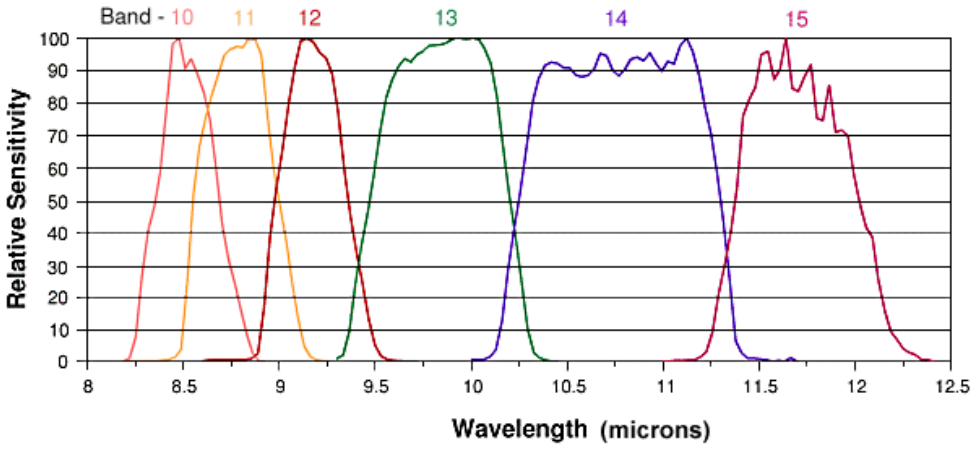

Figure 3.3: ATLAS Spectral Bands 10-15 (Luvall et al. 2005)

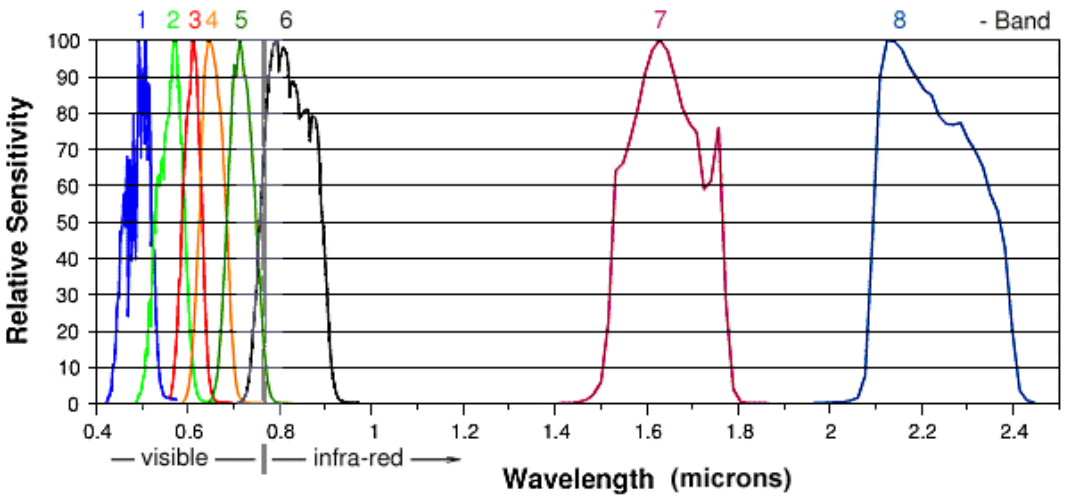

Figure 3.4: ATLAS Spectral Bands 1-8 (Luvall *et* al. 2005)

applied to calculate the ATLAS reference blackbody radiance for each channel of the sensor system.

The outputs of the MODTRAN4 (the high and low blackbodies temperature calibration of the ATLAS sensor system) are combined. The Earth Laboratory Applications Software (ELAS) then computed the system transfer equation within channel normalization, atmospheric correction, and the conversion of the 8-bit digital number of each pixel of the image data into 32-bit atmospheric radiance (Beverley and Penton 1989 and Graham *et al*. 1986). A graphical depiction of the overall process flow for the ATLAS data processing is shown in Figure 3.5 (Luvall *et al*. 2005).

3.1.2 Satellite Multispectral Data

To evaluate land cover change in Baton Rouge before and after the ATLAS collection, multispectral datasets from 1988 and 2003 are acquired. These multispectral data are collected from LANDSAT 5 (26 May 1988) and LANDSAT 7 (28 May 2003) satellites. The LANDSAT Project is a joint initiative of the U.S. Geological Survey (USGS) and NASA to gather Earth

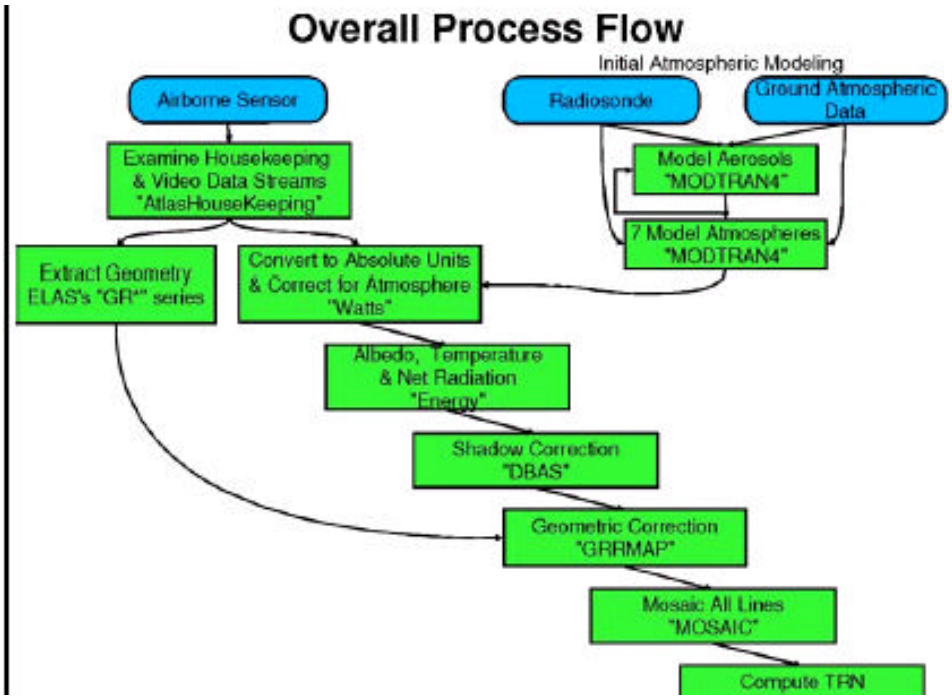

Figure 3.5: ATLAS Data Processing Flow to Produce Atmospheric, Radiometric and Geometrically Corrected Data Sets (Luvall *et* al. 2005)

resource data using a series of satellites. LANDSATs 5 and 7 currently orbit at an altitude of 705 km and collect data over a 185-km swath. Each satellite is sun-synchronous and provides a 16-day, 233-orbit cycle. The two satellite orbits are offset, allowing an 8-day repeat coverage.

Launched on 1 March 1984, LANDSAT 5 collects data from both its multispectral scanner (MSS) and its Thematic Mapper (TM). These onboard sensors detect reflected, scattered, and emitted energy from the Earth in the visible and infrared wavelengths. TM Bands 1-5 and 7 collect both reflected and scattered energy while Band 6 collects emitted energy. The TM sensor has a spatial resolution of 30 m for the six reflective bands and 120 m for the thermal infrared band. Six of the fifteen channels that comprise NASA's ATLAS sensor mirror the bandwidths of the TM sensor (Table 3.3). LANDSAT 7, launched on 15 April 1999, carries the Enhanced Thematic Mapper Plus (ETM+) sensor. The ETM+ offers 30-meter spatial resolution

for the visible and IR bands, a 60-m spatial resolution for its thermal band, and an additional 15-m panchromatic band (Table 3.4).

Table 3.3: LANDSAT 5 TM

LANDSAT 5	Wavelength (μm)	Resolution (m)	Corresponding ATLAS Channels
Band 1	0.45-0.52	30	Channel 1
Band 2	0.52-0.60	30	Channel 2
Band 3	0.63-0.69	30	Channel 4
Band 4	0.76-0.90	30	Channel 6
Band 5	1.55-1.75	30	Channel 7
Band 6	10.40-12.50	120	N/A
Band 7	2.08-2.35	30	Channel 8

3.1.3 *In Situ* Data

Meteorological data from the Baton Rouge area network of automated and COOP weather stations and the LDEQ are utilized in this study. The Automated Surface Observing Systems (ASOS) program is a joint effort of the National Weather Service NWS), the Federal Aviation Administration (FAA), and the Department of Defense (DOD). The ASOS system serves as the nation's primary surface weather observing

Table 3.4: LANDSAT 7 ETM+

LANDSAT 7	Wavelength (μm)	Resolution (m)	Corresponding ATLAS Channels
Band 1	0.45-0.52	30	Channel 1
Band 2	0.53-0.61	30	Channel 2
Band 3	0.63-0.69	30	Channel 4
Band 4	0.78-0.90	30	Channel 6
Band 5	1.55-1.75	30	Channel 7
Band 6	10.40-12.50	60	N/A
Band 7	2.09-2.35	30	Channel 8
Band 8	.52-.90	15	N/A

network by detecting significant meteorological changes and disseminating hourly and special observations via its network. ASOS collects a variety of weather variables including sky condition, visibility, present weather, obstructions to vision, surface pressure, ambient temperature, dew point temperature, wind (direction, speed, and character), and precipitation accumulation, and also includes selected significant remarks about the weather conditions.

The NWS COOP was formally created in 1890 under the Organic Act and has become the backbone of the U.S. climatological database. Its mission is to provide observational meteorological data, usually consisting of daily maximum and minimum temperatures, snowfall, and 24-hour precipitation totals, required to define the climate of the U.S. and to help measure long-term climate changes. These observational meteorological data are also used to support forecasts, warnings, and other public service programs of the NWS. To provide accurate and complete weather data, the NWS requires observations seven days per week, 365 days per year. Typically, the COOP station consists of a set of maximum/minimum thermometers, or a Max/Min Temperature System (MMTS), and a rain gauge. The temperature sensor of the COOP station is mounted 1.5 m (5 ft) above the ground at a level, open clearing so that the thermometers are freely ventilated by air flow. Whenever possible, COOP shelters are positioned no closer to an obstruction than four times the height of that obstruction and are at least 30 m (100 feet) from any paved or concrete surface.

Other surface meteorological data are available from non-NWS sites. Specifically, in accordance with the 1990 Clean Air Act Amendments, the Environmental Protection Agency (EPA) has required extensive monitoring of tropospheric ozone (O_3) and its precursors in areas with persistently high O_3 levels (mostly large metropolitan areas), including Baton Rouge. In

these areas, the states have established ambient air monitoring sites called Photochemical Assessment Monitoring Stations (PAMS) which collect and report detailed data for volatile organic compounds, nitrogen oxides, O_3, and meteorological parameters. Analyses of these data are providing an improved understanding of the underlying causes of O_3 pollution, to devise effective remedies, and to measure environmental improvement. All such stations must measure O_3, NO_x, and surface meteorological parameters (including temperature) on an hourly basis. These temperature data are used in this study to improve upon the spatial resolution provided by the NWS sites. Within the geographic scope of the ATLAS acquisition, four meteorological stations provide daily maximum temperature recordings (Figure 3.6). This is a network of one weather station per approximately 650 km^2.

3.1.4 Geographic Information System (GIS) Data Layers

A regional data set depicting the polygon boundaries of the 64 parishes of Louisiana is utilized in this study. This data set was derived from many data sources and conveys the best available representation of the parishes of Louisiana (LOSCO 1999). This data set portrays nominal and statistical attributes for each parish. Horizontal positions are specified in geographic coordinates, that is, latitude and longitude, in decimal degrees. The horizontal datum used is North American Datum (NAD) of 1983 and the ellipsoid used is the Geodetic Reference System (GRS) of 1980.

3.1.5 Color Infrared Orthophotography

Color infrared (CIR) orthophotographs produced from aerial photography are utilized for the ground truth/accuracy assessment portion of this study. The source imagery for production

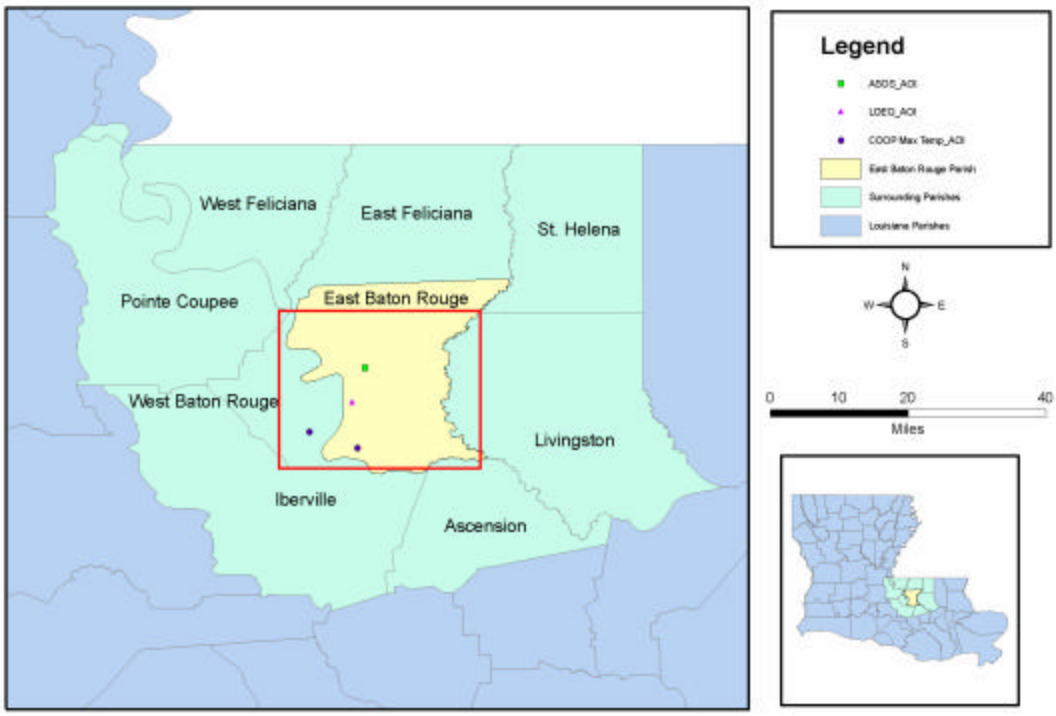

Figure 3.6: Stations Reporting Daily Maximim Surface Air Temperature within the ATLAS Coverage Area

of these orthophotos was flown in 1998 and 2004. An orthophoto is planimetrically correct because the distortions of scale due to elevation differences and aircraft orientation inherent in raw aerial photography have been removed as part of the orthophoto production process. Because the area covered by each image is approximately one quarter of the area of a standard 1:24000 scale (7.5 minute) USGS quadrangle map, they are sometimes referred to as Digital Orthophoto Quarter Quadrangles or DOQQs. Each pixel in an orthophoto represents an area of one square meter on the ground. CIR orthophotos are created from color infrared aerial photography film which is manufactured to be sensitive to red, green, and near-infrared wavelengths. This type of film makes near-infrared reflected energy visible to the human viewer by capturing that energy and representing it as a visible color. The dyes that are used in the film render green objects as blue images, red objects as green images, and objects that primarily reflect infrared as red images. Because healthy vegetation reflects strongly in the near-infrared,

vegetated areas appear red or pink. The appearance color for water in CIR imagery is highly variable and dependent on the water depth and amounts of floating vegetation and suspended matter; it can range in color from olive drab through turquoise, deep blue, and to black. Barren areas can be highly reflective at all wavelengths, and thus frequently appear very bright in a CIR image.

Because of the file size of each individual image in its original form, a 50:1 compression technique was implemented by the ortho-production company. The image compression technology selected for these data was the Multi Resolution Seamless Image Database (MrSID). MrSID compresses imagery displays as a smooth, non-resampled image at any display scale. When source imagery is in color, as is the imagery utilized in this study, compression levels of 50:1 produce images with a visual quality very nearly the same as the original. The MrSIDs utilized in this study were delivered in the Universal Transverse Mercator (UTM) projection Zone 15, referenced to the North Atlantic Datum 1983 using the Geodetic Reference System (GRS) 1980 spheroid, with mapping units of meters. A subset of the CIR orthophotography with a 50:1 compression ratio is shown in Figure 3.7.

Figure 3.7: Example of CIR Orthophotography
for Louisiana (LOSCO 2000)

3.2 STUDY AREA

3.2.1. The Baton Rouge Metropolitan Area

Baton Rouge sits on the east bank of the Mississippi River in south central Louisiana at 30°27'29" N, 91°8'25"W, and occupies approximately 200 km^2 of East Baton Rouge Parish (1225 km^2). The population of the Baton Rouge Metropolitan Statistical Area (MSA) in the 2000 Census was 604,084, representing a 14.1 percent increase since 1990 and a 22.0 percent increase since 1980. The Baton Rouge MSA is comprised of the parishes of Ascension (12.7 percent of the area's population in 2000), East Baton Rouge (68.4 percent), Livingston (15.3 percent), and West Baton Rouge (3.6 percent). According to the Metro Area Fact Sheet produced by the Federation for American Immigration Reform (2004), a NumbersUSA study in 2001 weighed urban sprawl factors in large metropolitan areas and concluded that 48.8 percent of the additional 262 km^2 consumed by the Baton Rouge urban area between 1970-90 was attributable to increased population.

3.2.2 Weather Conditions during the ATLAS Data Collection

For the entire month of May 1998, a persistent mid-tropospheric ridge centered over the southern states from New Mexico eastward to Georgia and Florida dominated the upper-air pattern across the United States. An equally persistent upper-air trough over the Pacific coast was also in place. The upper-air ridge prevented cold fronts associated with mid-latitude cyclones crossing the upper South from penetrating as far south as normal. Three cold fronts did reach Louisiana during the first half of the month: on the 3rd, the 9th, and 10th. However, these fronts were weak and produced very scattered, light showers. For Baton Rouge, the passage of the cold front on 10 May 1998 resulted in a drop in the maximum daily temperature of 4 C° from

the previous day. On 11-12 May 1998, daily maximum temperatures were back to 29°C and 31°C, respectively. As recorded on the ATLAS Post-Mission Flight Report (McKellip 1998), during the time of ATLAS data acquisition on 11 May 1998, visibility was reported to be 16 km, northeast winds of 1.3 – 2.6 m s^{-1} were recorded, and no clouds were present. For the remaining data collected on 12 May 1998, visibility was reported as 11 km, south winds of 1.8 – 4.5 m s^{-1} were recorded, and the first line of data flown contained 10 percent cloud coverage.

3.3 METHODOLOGY

3.3.1 Overview

Various aspects of the UHI of Baton Rouge, Louisiana, are evaluated in this study. The utilization of a surface heat content parameter is explored as an improved means of evaluating the nature of surface warming, by identifying long-term trends in both surface air temperature (T_a) and MSE (moist static energy, or surface heat content) at the Baton Rouge Metropolitan Airport. Then, the spatial pattern and resolution of the remotely-sensed, surface temperature-derived SHI are compared to that portrayed by the less-spatially-complete T_a-derived UHI. From the 1998 ATLAS dataset, surface temperature and corresponding NDVI values for each land cover type analyzed in this study are calculated. Regression equations are derived for each land cover type based on coincident NDVI and surface temperature values. These equations are then used to estimate surface temperature for the same land cover types based on NDVIs calculated from 1988 and 2003 SWIR datasets collected over the same location. As the amount of vegetation within the study area changes over time, corresponding surface temperature values will also be altered, thus revealing changes in the spatial extent and intensity of the SHI over time.

3.3.2 Surface Heat Content

To analyze surface warming based on surface meteorological data accurately, the MSE (Haltiner and Williams 1980) is determined by:

$$MSE = C_p T + L_v q$$

where C_p = specific heat of air at constant pressure (1004 J $kg^{-1}K^{-1}$)
T = air temperature (K)
L_v = latent heat of vaporization (2.45 x 10^6 J kg^{-1})
q = specific humidity (dimensionless)

The latent heat of vaporization at 0°C is 2.5008 x 10^6 J kg^{-1} and at 40°C is 2.406 x 10^6 J kg^{-1} (Hsu 1988). Given that the average daily maximum temperature in Baton Rouge ranges from 15.6-32.7°C (Figure 3.8), a latent heat of vaporization value of 2.45 x 10^6 J kg^{-1} is used in this study.

The ASOS of the National Weather Service provides a variety of surface meteorological data. The Baton Rouge ASOS is located at Ryan Airport, some 13 km (8 mi) north of the downtown area (Figure 3.9). Its actual location is 30°32'N, 91°09'W and 20 m (64 ft) above sea level. Elevations in East Baton Rouge Parish range from near 8 m (25 ft) to over 30 m (l00 ft) above sea level. Although the time period of this study spans 15 years, from May 1988 through May 2003, the Baton Rouge ASOS was not operational until 1 May 1993. To avoid discontinuity in the middle of the study period (from human-observations to ASOS), MSE calculations are generated only from 1 May 1993 through 31 May 2003.

For the purpose of this research, maximum daily T_a data (occurring at 1500 CST) along with corresponding surface pressure (p) and relative humidity (RH) values are obtained from the ASOS. From these variables, MSE is derived. Specifically, saturation vapor pressure (e_s) at the surface is calculated as a function of T_a using the Clausius-Clapeyron equation:

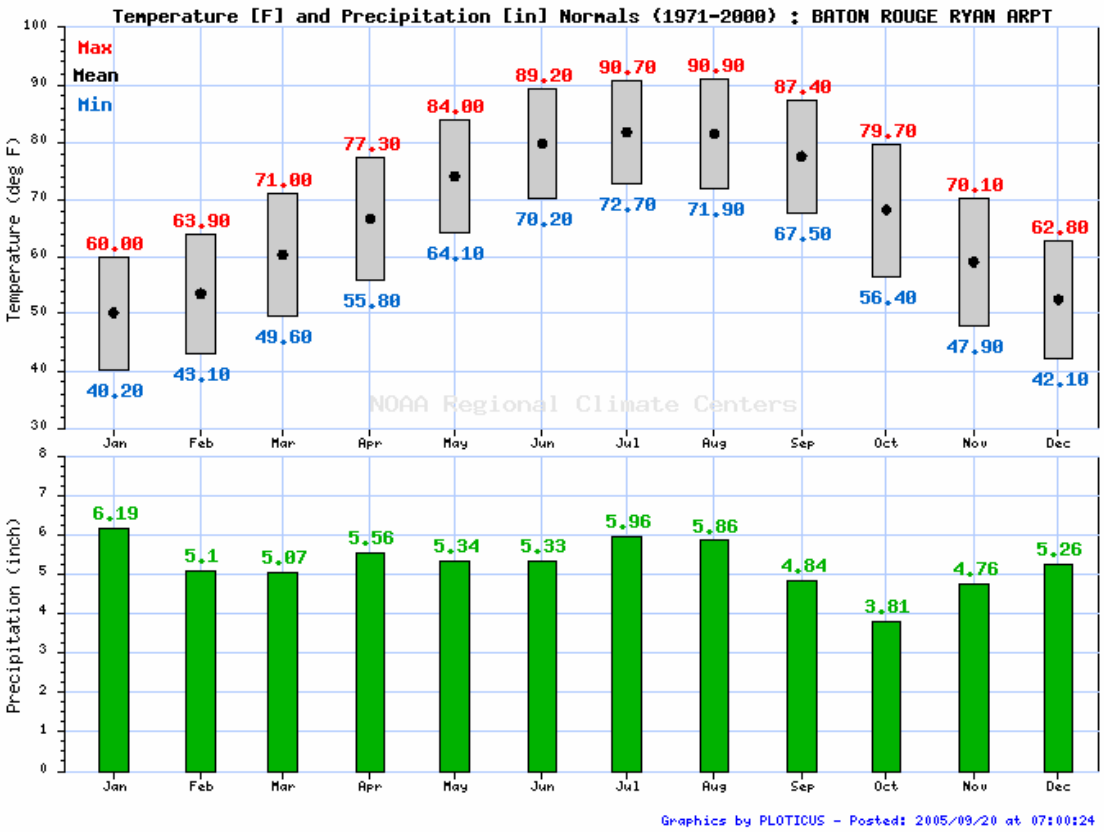

Figure 3.8: Climograph for Baton Rouge ASOS
(Southern Regional Climate Center, 2005)

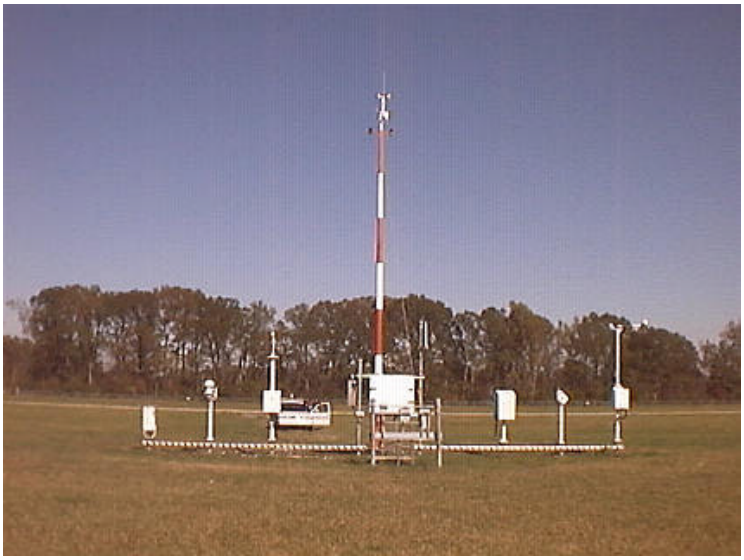

Figure 3.9: Baton Rouge Airport ASOS
(NOAA 2004)

$$e_s = 611\,Pa \quad \exp\left[\frac{L\,M_v}{R^*}\left(\frac{1}{273K} - \frac{1}{T_a}\right)\right]$$

where M_v represents the molecular weight of water vapor (.018015 kg mole^{-1}) and R* represents the universal gas constant (8.314 J mole^{-1} K^{-1}). Then surface vapor pressure (e) is calculated from

$$e = RH\ e_s$$

and q is computed from

$$q = \frac{e\,e}{p}$$

where e is the ratio of the molecular weight of water vapor to the molecular weight of dry air (0.622).

From these equations, MSE can be calculated using only readily-available surface meteorological data. Pearson's correlation coefficient and paired t-tests are used to test the relationship between MSE and temperature of surface air, and Spearman's Test for Trend analyzes temporal trends in both surface air temperature and MSE. The two variables are likely to be similar, particularly since T_a is a component, but MSE is hypothesized to be a better indicator of the UHI. Of course, a violation of the assumption of independence of the independent variables occurs in this part of the analysis, so results should be interpreted with caution.

3.3.3 Spatial Analysis of the UHI *vs*. SHI

3.3.3.1 Creating the UHI Surface

The UHI surface (T_a-derived UHI) is derived from a spatial interpolation of the meteorological data from the network of COOP weather stations and the ambient air monitoring

sites from LDEQ. Within the ATLAS area of coverage, in addition to the Baton Rouge Airport ASOS, two COOP stations and one ambient air monitoring site provide maximum daily temperature. The Brusly station (COOP #161246) is located at 30°24'N, 91°16'W at an elevation of 6.1 m (20 feet) above sea level and began collecting data on 1 March 1987. The LSU Ben Hur Farm station (COOP #165620) is located at 30°22'N, 91°10'W at an elevation of 6.1 m (20 feet) above sea level and began collecting data on 1 December 1987. Among the LDEQ sites, the Baton Rouge Capitol site (AIRS #220330009) is located at 30º27'43.5"N, 91º10'36.9"W and began collecting meteorological data in 1991. During the 1993-2003 study period, there was no significant missing data for any of the sites.

Surface interpolation functions create a continuous (or prediction) surface from sampled point values. For this study, the continuous surface representation of a raster data set represents maximum daily temperature data from the above sites, recorded during the ATLAS collection period. The Inverse Distance Weighted (IDW) function is the chosen method of interpolation. IDW estimates cell values by averaging the values of sample data points in the neighborhood of each processing cell. The closer a point is to the center of the cell being estimated, the more influence (or weight) it has in the averaging process. This method assumes that the variable being mapped decreases in influence with distance from its sampled location. The IDW method is referred to as a deterministic interpolation method because it assigns values to locations based on the surrounding measured values and on specified mathematical formulas that determine the smoothness of the resulting surface. The interpolated surface of the UHI (T_a-derived UHI) can subsequently be compared to that of the continuous surface of the surface temperature-derived SHI.

3.3.3.2 Creating the Surface Temperature-derived SHI

To compare the spatial pattern of the T_a-derived UHI to that of the remotely-sensed, surface temperature-derived SHI, the ATLAS data set must first be imported within ERDAS IMAGINE. The actual ATLAS aircraft data are in ELAS format, which is a Band Interleaved by Line (BIL) format with a 1024 byte header. The data are floating point, stored in IEEE standard format, and are single precision real. There are 21 flight lines of ATLAS data covering the spatial extent of this study. For every flight line, there are three types of ATLAS data files utilized; the full fifteen channel composite, a fifteen band file of radiance values, and a four-band georeferenced energy file. To import the ATLAS data into ERDAS IMAGINE, the generic binary format within the Import Module is selected. This format is chosen because the ATLAS formatted data is not a common, standardized dataset. Parameters for each flight line, as noted within each ELAS file header, must be manually input in order to set the import routine.

Aircraft data reference names are built from the processing status, year, a serial reference number, number of times the aircraft took off, a flight path reference number and an attempt number. For example, Table 3.5 indicates how to read the file named "ref9811f1.11". This particular image, “ref9811f1.11”, represents fifteen channels of raw aircraft data with Channel 1 edited to correct defects in geometry housekeeping. File format parameters from its associated ELAS header file “REF9811F1.11.ELASHeader.TXT” are entered into the ERDAS IMAGINE import routine (Figure 3.10) resulting in the creation of the “ref9811f111.img” file (Figure 3.11).

Also for Flight Line 1, the fifteen-band radiance file is imported into ERDAS IMAGINE using the parameters noted in the “BR_F1.11.WATS.ELASHeader.TXT” header file (Figure 3.12). This file, “br_f1.11.wats”, represents the output from the program Watts (Luvall *et* al.

2005) of which the input file was "Ref9811f1.11" and the units are W cm^{-2} μm^{-1}. The resulting file, "br_f1_11wats.img", is noted in Figure 3.13.

Table 3.5: ATLAS Nomenclature

ATLAS Code	Definition
Ref	Data has been formatted into ELAS format, a computer compatible format.
98	Request was for data acquisition in 1998
11	Mission request is 11th one filed for the ATLAS scanner
F	Data are from an aircraft flight
1	This is the first time the aircraft took off to acquire data for this year and mission number.
1	This is line 1 of the requested flight lines
1	This is attempt 1 to get the flight line.

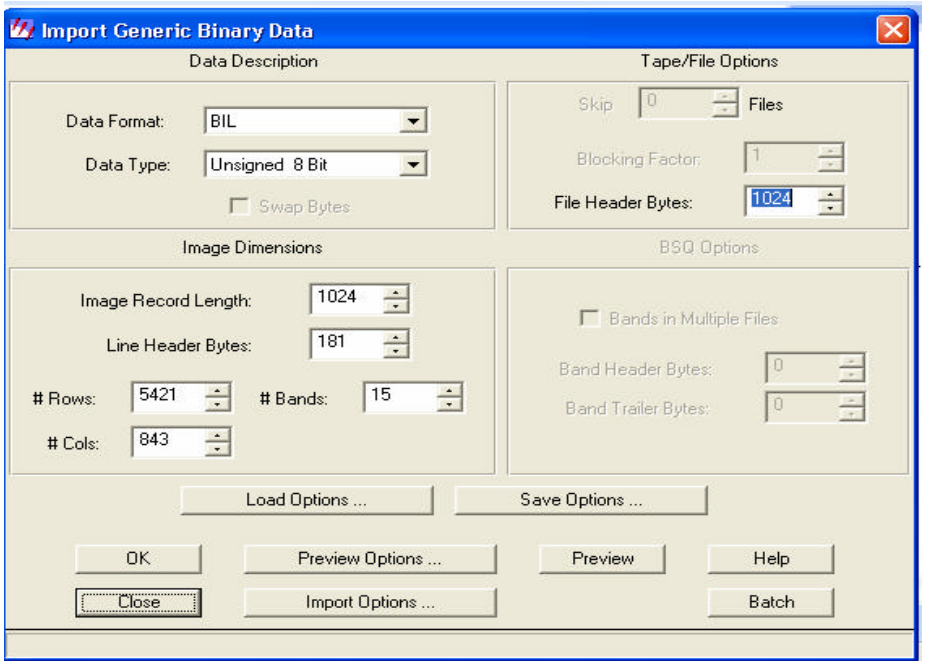

Figure 3.10: ATLAS Import Routine for "ref9811f1.11"

Figure 3.11: The 15 Channel "ref9811f1.11.img" File

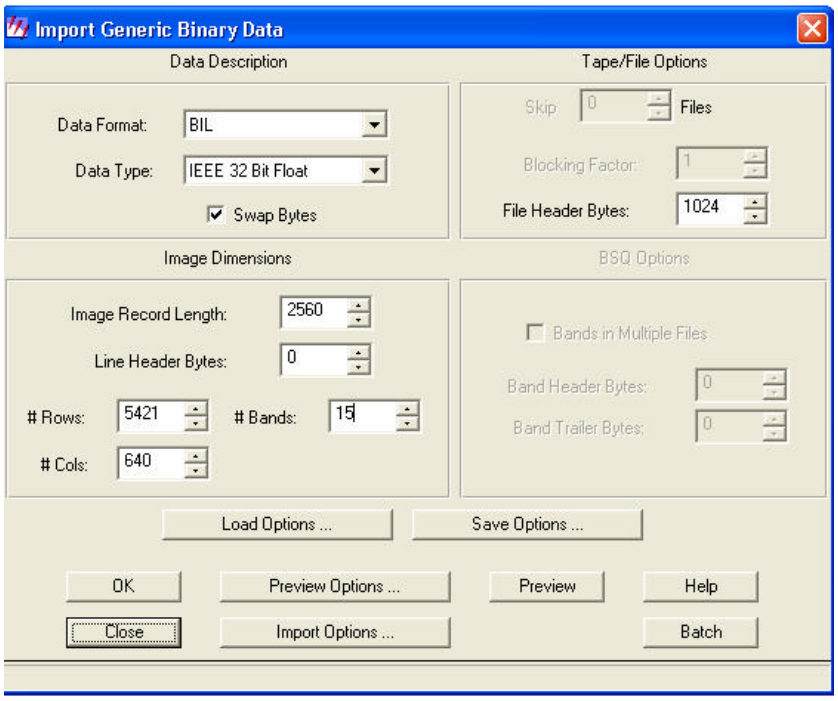

Figure 3.12: ATLAS Import Routine for "br_f1.11.wats"

Figure 3.13: Creation of the15 Band
"br_f1_11wats.img" Radiance File

The third ATLAS data set for Flight Line 1 is the four-channel energy file. This file is imported into ERDAS IMAGINE using the parameters noted in the "BR_F1.11.ENERGY.GEO.ELASHeader.TXT" header file (Figure 3.14). These data, "br_f1.11.energy.geo", represent the output from the program Energy (Luvall *et* al. 2005) of which the input file was "br_f1.11.wats" and the resultant channels correspond to 1) albedo, 2) surface temperature, 3) surface temperature via Anderson's method (Anderson 1992), and 4) net radiation within bandpass. The resulting file, "br_f111energy_geo.img", is noted in Figure 3.15.

3.3.3.3 Comparing the T_a-derived UHI Surface to the Surface Temperature-derived SHI

The ATLAS area of coverage extends to approximately 2600 km^2 at a spatial resolution of 10 m. Within this coverage, four meteorological stations provide daily maximum T_a

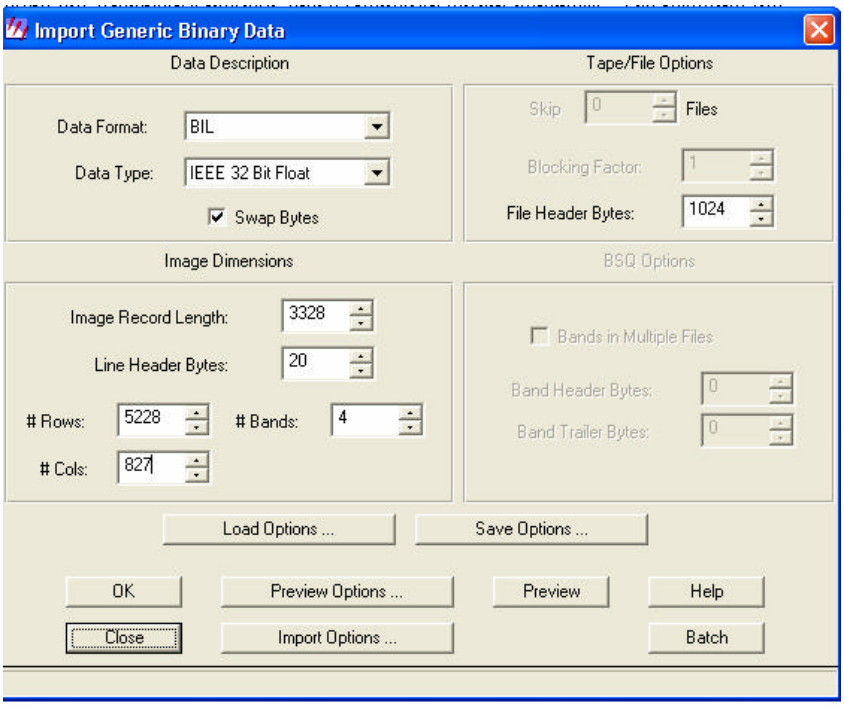

Figure 3.14: ATLAS Import Routine for "br_f1.11.energy.geo"

Figure 3.15: Creation of the 4 Band "br_f111energy_geo.img" Energy File

recordings. A spatial interpolation of T_a is performed to compare the spatial pattern and resolution of the T_a-derived UHI to that of the remotely-sensed, surface temperature-derived SHI.

3.3.4 Temporal Analysis of the of the UHI vs. SHI

3.3.4.1 Overview

A classification scheme is required for the 1998 ATLAS dataset in order to assign surface temperatures and NDVIs to specific land cover types. Established linear regression equations for each land cover type, relating 1998 ATLAS NDVIs to surface temperature, can then be applied to other SWIR multispectral data sets of the same spatial extent capable of classifying land cover types. In this study, multispectral LANDSAT images from 1988 and 2003 are utilized to offer NDVIs and land cover types for the study area prior to and after the 1998 ATLAS collection. Based on their NDVIs and established regression equations, corresponding surface temperature values are assigned to the land cover polygons from each data set (1988 and 2003). A change detection of surface temperature values, as a function of land cover, offers both a temporal and spatial evaluation of the Baton Rouge SHI on case study days during a decade of urbanization.

3.3.4.2 LANDSAT Data Preparation for Classification Process

Because the blue band of LANDSAT images contains too much noise and ultimately leads to a poor representation of ground reflectance values within that channel, and due to the high between-group correlation of the reflectance values of the LANDSAT Visible Bands 1, 2, and 3 (1-blue, 2-green, and 3-red), it was determined that Bands 5, 4, and 3 would be used for the

unsupervised classification routine. Band 5 allows for the addition of near-infrared reflected data and therefore helps with the delineation of vegetation throughout the study area. Bands 3 and 4, both representing the visible portion of the spectrum, are less affected by atmospheric attenuation than other visible bands and will therefore aid in the delineation of the urban environment.

The LANDSAT data sets utilized in this study, from LANDSAT 5 and 7, are created by the U.S. Geological Survey (USGS) and contain radiometrically and geometrically corrected data files in Geographic Tagged Image-File Format (GeoTIFF). GeoTIFF defines a set of publicly-available TIFF tags that describe cartographic and geodetic information associated with TIFF images. GeoTIFF is a format that enables referencing a raster image to a known geodetic model or map projection. By using the GeoTIFF format, both metadata and image data can be encoded into the same file.

Both LANDSAT data sets (1988 and 2003) are delivered in the Universal Transverse Mercator (UTM) Projection Zone 15, referenced to the North Atlantic Datum 1983 using the Geodetic Reference System (GRS) 1980 spheroid, with mapping units of meters. Both data sets were delivered as a grayscale, uncompressed, 8-bit string of unsigned integers in separate data bands. The GeoTIFF Bands 3, 4, and 5 from both data sets were imported into ERDAS IMAGINE and converted into IMAGINE (.img) data files (Figures 3.16 and 3.17). Through the ERDAS IMAGINE layer stack command, the three bands (3, 4, 5) were then merged to produce a combined data file for each year (Figures 3.18 and 3.19).

Through the ERDAS IMAGINE subset command, the stacked data files were cropped to spatially coincide with the ATLAS area of coverage as specified in Table 3.6 below. This yields two LANDSAT datasets (1988 and 2003) each comprising approximately 2600 km^2 (Figures 3.20 and 3.21).

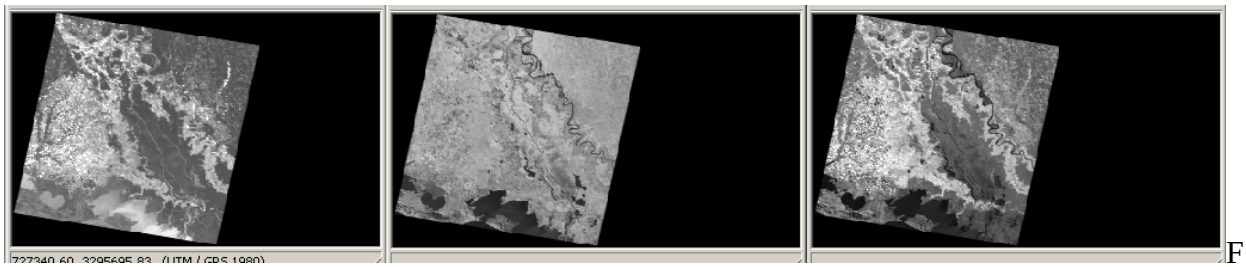

Figure 3.16: LANDSAT 1988 Bands 3, 4, 5

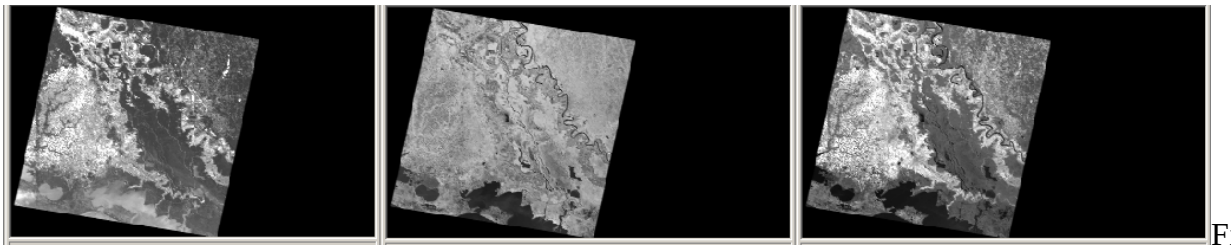

Figure 3.17: LANDSAT 2003 Bands 3, 4, 5

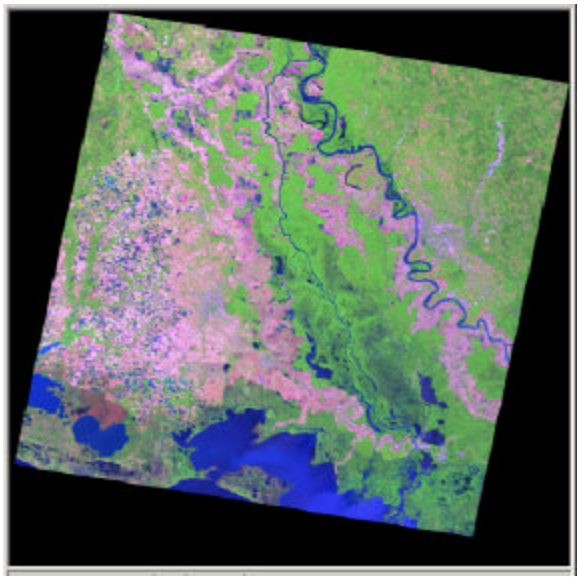

Figure 3.18: LANDSAT 1998

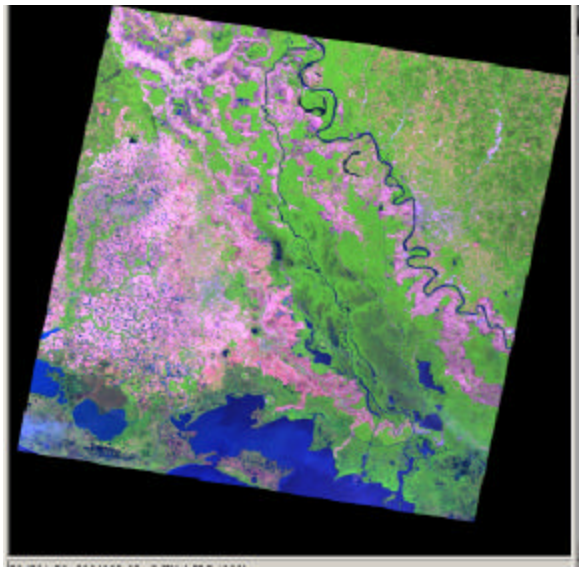

Figure 3.19: LANDSAT 2003

Table 3.6: ATLAS Area of Coverage (UTM Zone 15)

Upper Left X (ULX)	Upper Left Y (ULY)	Lower Right X (LRX)	Lower Right Y (LRY)
656221.48 meters	3401312.06 meters	708554.15 meters	3351248.27 meters

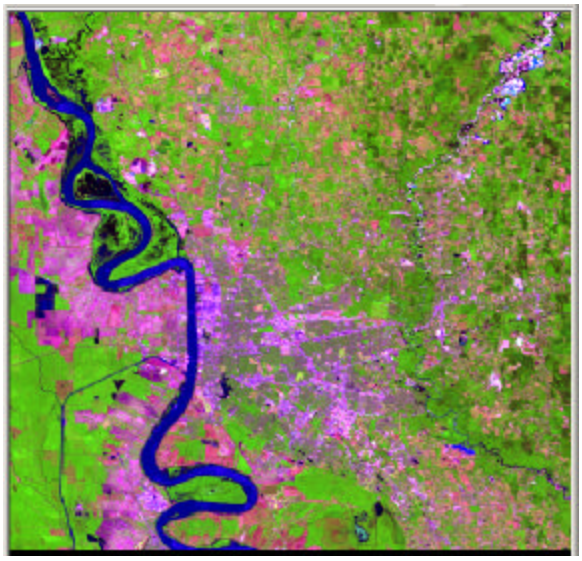

Figure 3.20: LANDSAT 1998 Cropped Image

Figure 3.21: LANDSAT 2003 Cropped Image

3.3.4.3 Classification Theory and Selection

Image classification is the grouping of image pixels into categories or classes to produce a thematic representation. It can be performed on single or multiple image channels (multispectral) to separate areas according to their different scattering or spectral characteristics. Multispectral classification involves the process of sorting pixels into a finite number of individual classes, or categories of data, based on their data values. If a pixel satisfies a certain set of criteria, the pixel is assigned to the class that corresponds to those criteria.

There are two parts to the image classification process: training and classifying. Training is the process of defining criteria by which patterns can be recognized. The training process is either supervised (using *a priori* data to determine classes) or unsupervised (computer automated determination). Due to a very general classification scheme required for this study, only the unsupervised process is utilized. The detection of statistical patterns inherent in the study data results in a set of signatures that defines a training sample, or cluster. Each signature

within a cluster corresponds to a class, and is used with a decision rule to assign the pixels in the image file to that class. The decision rule is a mathematical algorithm that, using data contained in the signature, performs the actual sorting of pixels into distinct class values.

Unsupervised training is often termed "clustering" because it is based on the natural groupings of pixels in image data when they are plotted in feature space. In this study, clusters are defined with the Iterative Self-Organizing Data Analysis (ISODATA) technique (Tou and Gonzalez 1974). This clustering method uses spectral distance as in the sequential method, but classifies the pixels iteratively, redefines the criteria for each class, and classifies again, so that the spectral distance patterns in the data gradually emerge (Jensen 1996). ISODATA is iterative in that it repeatedly performs an entire classification (outputting a thematic raster layer) and recalculates statistics.

The ISODATA method requires certain user-specified parameters: the maximum number of clusters to be considered (n), a convergence threshold (t) indicating the maximum percentage of pixels for which class values are allowed to be unchanged between iterations, and the maximum number of iterations (m) to be performed (Tou and Gonzalez 1974). Because each cluster is the basis for a class, (n) becomes the maximum number of classes to be formed. The ISODATA process begins with a specified number of arbitrary cluster means and then it processes repetitively, so that those means shift to the means of the clusters in the data. On the first iteration of the ISODATA algorithm, the means of (n) clusters can be determined arbitrarily. After the first iteration, a new mean for each cluster is calculated, based on the actual spectral locations of the pixels in the cluster, instead of the initial arbitrary calculation. The spectral distance between the candidate pixel and each cluster mean is then calculated. The pixel is assigned to the cluster whose mean is the closest. These new means are used for defining

clusters in the next iteration. The process continues until there is little change between iterations, or the convergence threshold is reached. It is possible for the percentage of unchanged pixels to never converge (i.e., never reach (t)). Therefore, it is beneficial to monitor the percentage, or specify a reasonable maximum number of iterations (m) so that the program does not run indefinitely. This clustering procedure allows the study area to be subdivided into categories based on spectral characteristics. When later used with a decision rule, this procedure will delineate land cover features.

Upon completion of the unsupervised training process, each pixel is analyzed independently. The measurement vector for each pixel is compared to each signature, according to the decision rule. Pixels that satisfy the criteria that are established by the decision rule are then assigned to the class for that signature. Data can be classified both parametrically with statistical representation, and nonparametrically as objects in feature space. Figure 3.22 shows the flow of an image pixel through the classification decision-making process in ERDAS IMAGINE (Kloer 1994).

The nonparametric decision rule utilized in this study is the parallelepiped. This decision rule is useful for a first-pass, broad classification, as it quickly narrows down the number of possible classes to which each pixel can be assigned. This is an important task before the more time-consuming parametric calculations are made, thus minimizing overall processing time. In this decision rule, the data file values of the candidate pixel are compared to upper and lower limits. The high and low limits are for every signature in every band and these remain constant for each band. In this study, the limits are the mean of each band, plus or minus one standard deviation. When a pixel's data file values are between the limits for every band in a signature, then the pixel is assigned to that signature's class.

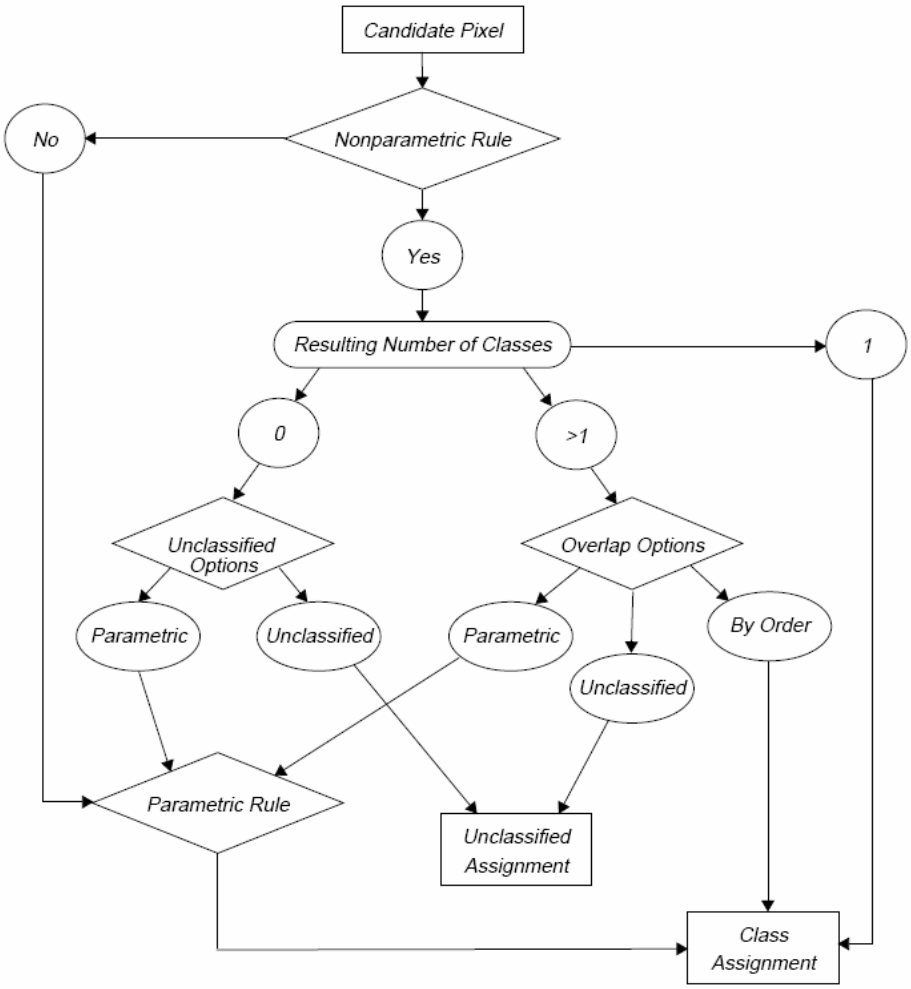

Figure 3.22: The Image Classification Process

The parametric decision rule utilized in this study is the maximum likelihood. This algorithm is the most accurate of the classifiers in the ERDAS IMAGINE software package because it takes variability of classes into account by using the covariance matrix. The maximum likelihood decision rule is based on the probability that a pixel belongs to a particular class. The basic equation assumes that these probabilities are equal for all classes, and that the

input bands have normal distributions. The candidate pixel is assigned to the class, c, for which D is the lowest:

$$D = \ln(A_c) - 0.5 \ln|Cov_c| - 0.5 (X - M_c) T (Cov_c - 1) (X - M_c)$$

where D = weighted distance (likelihood)
c = a particular class
X = the measurement vector of the candidate pixel
M_c = the mean vector of the sample of Class c
A_c = percent probability that any candidate pixel is a member of Class c (defaults to 1.0, or is entered from *a priori* knowledge)
Cov_c = the covariance matrix of the pixels in the sample of Class c
$|Cov_c|$ = determinant of Cov_c (matrix algebra)
Covc-1= inverse of Cov_c (matrix algebra)
ln= natural logarithm function
T= transposition function (matrix algebra)

3.3.4.4 Accuracy Assessment for the LANDSAT Land Cover Classification

The purpose of any land classification scheme is to produce the most accurate land cover classification for a study area. This is qualified through a ground truth routine resulting in an accuracy assessment of the classification process. Based on the size of the study area and the number of classes, 200 training points are auto-generated throughout the study area. Classification polygons for urban, bare land, vegetation-forest, vegetation-non forest, and water are validated against actual land cover as depicted in Digital Ortho Quarter Quads (DOQQs) for the study area.

3.3.4.5 Applying the ATLAS Surface Temperature Data

The land cover classification scheme for this study consists of five categories: urban, bare land, water, vegetation-forest, and vegetation-other. Representative land cover polygons from a selected flight line are digitized from the 1998 ATLAS dataset and corresponding surface temperature values are extracted for each land cover. The purpose of digitizing representative

land cover polygons from one flight line is to assure that the surface temperature for each land cover was acquired during the same time with the same atmospheric conditions.

3.3.4.6 Use of the NDVI

Because chlorophyll reflects very little radiation in the red portion of the electromagnetic spectrum (EMS) but reflects most infrared radiation incident upon it, and because non-natural and most non-vegetated surfaces have very similar relative reflectance values in both the red and infrared portions of the EMS, the NDVI is an approximation of the percentage of vegetation coverage within a pixel of the image dataset. From the SWIR bands of the ATLAS sensor, NDVIs are computed to yield the percentage biomass within the study area. The NDVI is calculated as the ratio of energy reflected from the area of interest in the near-infrared portion of the EMS to that reflected in the visible red portion of the EMS.

$$NDVI = \frac{IR - red}{IR + red}$$

where IR = infrared band (usually near-infrared) and
red = visible red band of the EMS

The NDVI calculation produces a new image map containing NDVI values. NDVI values range from –1.0 to +1.0, indicating the amount of vegetation (percentage of biomass) that is found in each dataset pixel. Therefore, a visual interpretation of this image indicates the presence of vegetation within the study area. Average NDVI values are assigned to corresponding land cover polygons within the 1998 ATLAS data set and the 1988 and 2003 LANDSAT data sets.

3.3.4.7 The ATLAS Surface Temperature and NDVI Regression

The relationship between the surface temperature of each land cover type and the amount of its corresponding NDVI is calculated and Pearson correlation coefficients are determined. In the case of a nonlinear relationship between surface temperature and vegetation, the eta (η) coefficient, or the correlation ratio (Hinkle *et al*. 1994), is used. The interpretation of the eta (η) coefficient is the same as for the Pearson *r*. That is, the square of the coefficient (η^2) represents the proportion of the variance in the Y variable that can be attributed to the variance in the X variable.

Regression equations are developed to predict surface temperature from known NDVIs of land cover polygons within the 1998 ATLAS data set. Based upon computed NDVI values for land cover polygons within both the 1988 and 2003 land cover classification layers, and by using the1998 regression equations, land cover polygons from each data set (1988 and 2003) are assigned corresponding surface temperature values.

3.3.4.8 Mapping the 1988 and 2003 Baton Rouge SHI

An assessment of the change in the spatial extent and intensity of the Baton Rouge SHI is achieved by an overlay of computed 1988 and 2003 surface temperature values as a function of land cover. A linear temporal increase in MSE, RH, and pressure, calculated from daily T_a from 1993 to 2003, serves as verification of the expected increase in the intensity of the Baton Rouge SHI over the same time period. Furthermore, changes within the Baton Rouge SHI from 1988 to 2003 are tested against spatially-interpolated T_a data from the meteorological stations for 1988 and 2003.

3.4 CHAPTER SUMMARY

In this chapter, data acquired and methodology utilized for analyzing the properties of the SHI in Baton Rouge, Louisiana, are discussed. Specifically, LANDSAT 5 and LANDSAT 7 multispectral scanner data from 1988 and 2003 (respectively) were used to supplement airborne (ATLAS) multispectral data from 11-12 May 1998 for Baton Rouge. Color infrared orthophotographs were used for ground truth/accuracy assessment. Spatial analysis of air temperature and surface heat content across Baton Rouge was done by using meteorological data to represent the urban heat island and the remote sensing-based data to represent the SHI. Then a land cover classification was performed to assign surface temperatures and NDVIs to specific land cover types based on the 1998 dataset. The purpose is to reconstruct the spatial aspects of the SHI in 1988 and 2003 based on the satellite data. The ISODATA algorithm was chosen for the unsupervised clustering procedure. The classification resulted in five categories: urban, bare land, water, vegetation-forest, and vegetation-other. Regression-based procedures were then implemented to predict surface temperatures from known NDVIs of the land cover polygons within the 1998 ATLAS dataset. The following chapter describes the results of such analysis.

CHAPTER 4. RESULTS

4.1 OVERVIEW

This chapter will describe the major results of the tests of the research hypotheses described in Chapter 1. The relationship between the T_a and MSE variables is tested using a Spearman correlation coefficient. A spatial interpolation of the 1998 surface UHI (T_a-derived UHI) is performed in order to compare its spatial resolution and pattern to that of the 1998 surface temperature-derived SHI. A land classification scheme consisting of five categories (urban, bare land, water, vegetation-forest, and vegetation-other) is carried out on two LANDSAT data sets from 1988 and 2003. Corresponding surface temperature and NDVI values for these five land cover categories are extracted from the 1998 ATLAS data set in order to compute regression equations. Once established, these equations are used to predict surface temperatures from known NDVIs of corresponding land cover polygons within the 1988 and 2003 LANDSAT classification data sets. The major implications of these results are discussed to provide a better understanding of the spatial and temporal properties of the Baton Rouge SHI.

4.2 SURFACE AIR TEMPERATURE AND MOIST STATIC ENERGY

For the purpose of this research, daily maximum air temperature (T_a) data (occurring at 1500 CST) along with corresponding sea level pressure (SLP) and relative humidity (RH) values are obtained from the ASOS within the study area. From these variables, corresponding moist static energy (MSE) values are derived for each reported T_a. For the time period of May 1993 to May 2003, a total of 3633 data pairs were available. Descriptive statistics are calculated for both

T_a (Table 4.1) and MSE (Table 4.2).

Table 4.1: T_a Descriptive Statistics (^oF)

			Statistic	Std. Error
Temp	Mean		75.91	.219
	95% Confidence Interval for Mean	Lower Bound	75.48	
		Upper Bound	76.34	
	5% Trimmed Mean		76.59	
	Median		78.00	
	Variance		173.783	
	Std. Deviation		13.183	
	Minimum		31	
	Maximum		103	
	Range		72	
	Interquartile Range		19	
	Skewness		-.693	.041
	Kurtosis		-.127	.081

Because the normality assumption of the Pearson correlation is violated, the Spearman's rho (r) is utilized for this study. Results indicate a Spearman correlation coefficient of 0.901 (p-value < 0.01) between T_a and MSE. The paired samples test confirms a relationship between these variables (Table 4.3). It is not surprising that the two variables are highly correlated, particularly since T_a is a component of MSE.

To analyze linear temporal trends in both T_a and MSE in Baton Rouge from 1993 to 2003, a Spearman correlation between T_a and observation number is compared to that of MSE and observation number. Results identify a significant linear temporal decrease in MSE (r = -0.07, p-value = 0.00005), but no significant linear trend in T_a (r = -0.02, p-value = 0.22)).

Table 4.2: MSE Descriptive Statistics (J kg^{-1})

			Statistic	Std. Error
MSE	Mean		326809.1683	309.04822
	95% Confidence Interval for Mean	Lower Bound	326203.2430	
		Upper Bound	327415.0936	
	5% Trimmed Mean		327388.9394	
	Median		329603.6073	
	Variance		346990747.903	
	Std. Deviation		18627.68767	
	Minimum		277432.83	
	Maximum		390597.98	
	Range		113165.15	
	Interquartile Range		30239.49	
	Skewness		-.417	.041
	Kurtosis		-.875	.081

Table 4.3: Paired Samples Test

		Paired Differences					T	Df	Sig. (2-tailed)
		Mean	Std. Deviation	Std. Error Mean	95% Confidence Interval of the Difference				
					Lower	Upper			
Pair 1	Temp – MSE	326733.26027	18615.70141	308.84936	327338.79569	326127.72486	1057.905	3632	.000

Therefore, the maximum T_a-defined UHI of Baton Rouge has not changed significantly over the study period, and urban growth has actually appeared to be associated with linear decreases in MSE over the 1993-2003 period (although no cause-effect relationship can be inferred from this result). Perhaps other feedbacks are accounting for the lack of observed warming with increasing urbanization.

To analyze the temporal trends of both T_a and MSE further, the monthly average of both variables is plotted for the study period (Figure 4.1). A visual interpretation confirms that both variables simultaneously experience seasonality effects from monthly temperature changes. This too is not surprising since T_a is a component of MSE.

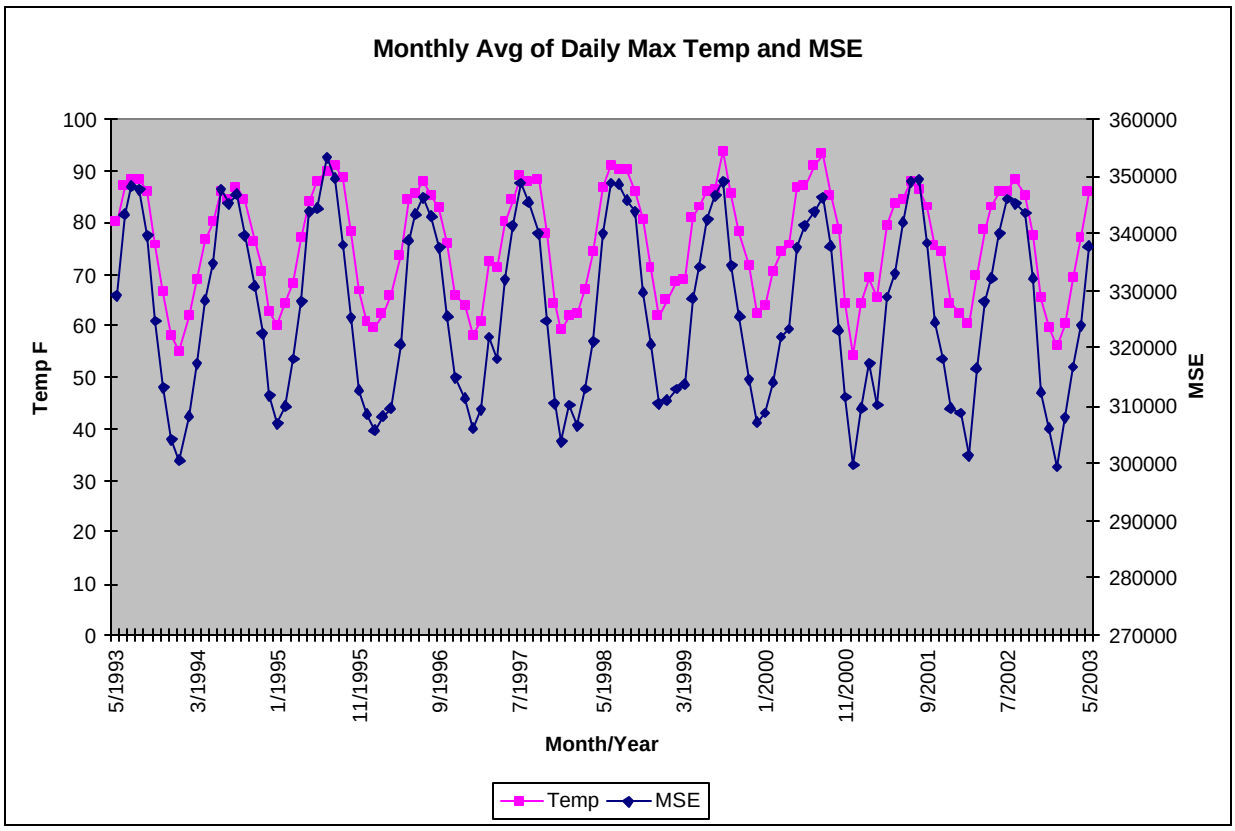

Figure 4.1: Monthly Average of Daily Maximum Air Temperature and MSE

Therefore, the remainder of the study is conducted based on the acknowledgment that any deforestation coincident with development may have had a negligible effect on the UHI of Baton Rouge thus far. However, it is also possible the deforestation has had an impact that was offset by other factors that are not investigated in this dissertation. Furthermore, even if deforestation has not had an impact on the UHI of Baton Rouge during the study period, there is nothing to suggest that further deforestation in the future will not have an effect. Thus, results of this study

remain important for urban and environmental planners, particularly since so much forested area remains to be lost to profligate and careless land-use practices.

4.3 SPATIAL ANALYSIS OF THE UHI

4.3.1 Spatial Interpolation of the Surface UHI (T_a-derived UHI)

The ATLAS data set was collected within a two-day period, 11-12 May 1998. The surface UHI (T_a-derived UHI) originates from daily temperature point data and therefore two data sets are required to match the temporal scale of the ATLAS data. The daily maximum temperatures recorded at the surface monitoring sites (ASOS, COOP, and LDEQ) are averaged to produce one surface temperature file in a database format (.dbf). The .dbf file is imported into ArcMap and converted into a shapefile. This point shapefile is spatially interpolated in order to produce a continuous surface (raster) comparable to that of the ATLAS data. Within the ArcMap's Spatial Analyst extension, the Inverse Distance Weighted (IDW) method is used to interpolate the shapefile into a raster data set. The average maximum temperature is selected as the "z" field and a variable search radius is selected. The raster image depicting the continuous surface of the average maximum daily temperature for the study area during 11-12 May 1998 is noted in Figure 4.2.

4.4 TEMPORAL ANALYSIS OF THE UHI AND SHI

4.4.1 Land Cover Classification for the LANDSAT Data Sets

From a land classification viewpoint, there are two main goals of this research endeavor: to evaluate the SHI as a function of land cover and to investigate the thermal efficiency of urban land cover with respect to the potential impact of tree growth within the study area.

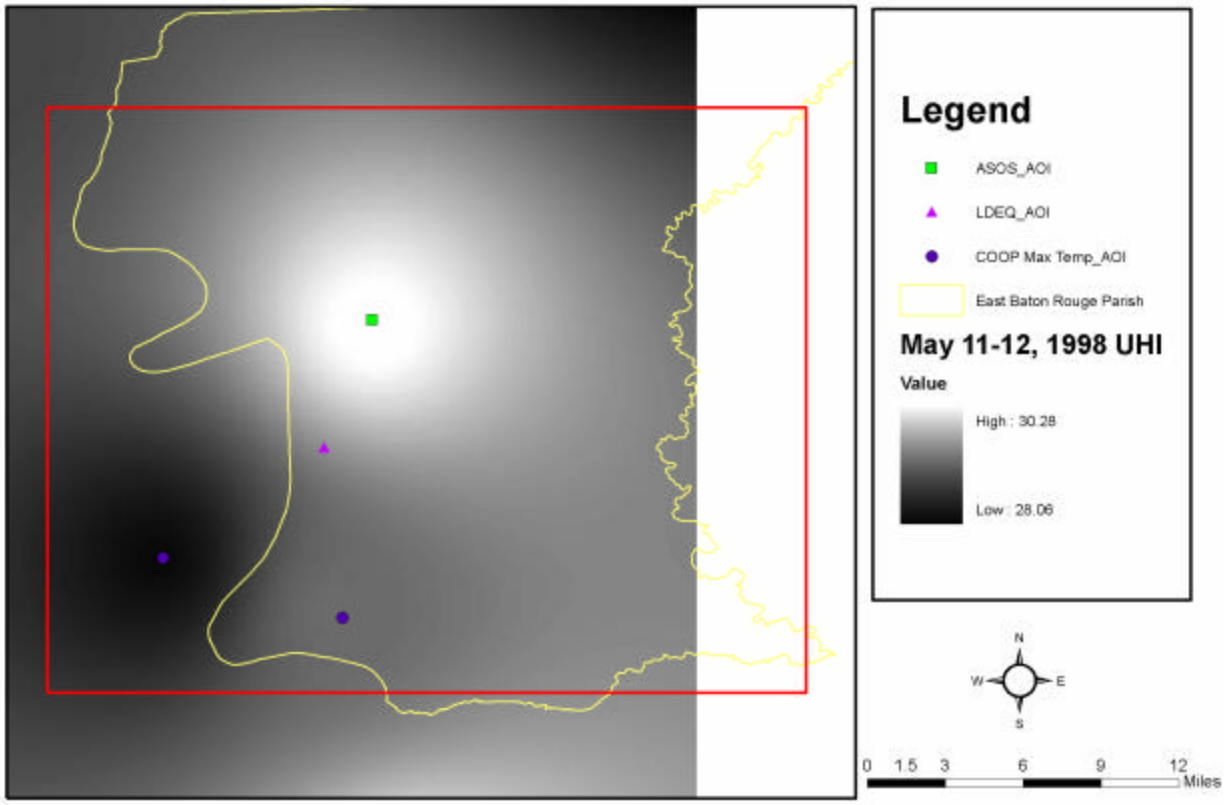

Figure 4.2: IDW Spatial Interpolation for Surface Temperature Data 11-12 May 1998

Therefore, it is imperative that the land classification scheme for the study area include the categories of "urban" and "vegetation-forest". Upon initial visual inspection of the LANDSAT imagery, it is evident that many non-urban areas (such as bare soils) can produce similar reflectance values to that of urban areas. It is also noted that throughout the study area that vegetation exists in many forms. Therefore, five land classification categories are delineated within the study area: urban, bare land, vegetation-forest, vegetation-non-forest, and water.

Within the ERDAS IMAGINE interpreter module (spectral enhancement-indices), a NDVI is calculated for each LANDSAT image. For LANDSAT TM imagery, the NDVI calculation [(band4 – band 3) / (band 4 + band 3)] is used and the result for 2003 is depicted in Figure 4.3. Although the NDVI provides the initial means to differentiate vegetation from non-vegetation, a more precise separation can be achieved by applying a general contrast to the

NDVI histogram, more specifically histogram thresholding of the NDVI image. By altering the histogram through level slicing (only two levels required, representing either vegetation or non-vegetation), the breakpoints of the NDVI histogram are adjusted using the shift/bias tool (Figure 4.4). The exact separation between vegetation and non-vegetation is validated by flickering back to the LANDSAT (3, 4, 5) image. Once the value for the separation is determined, the new histogram is saved to a lookup table (LUT) for the corresponding NDVI file.

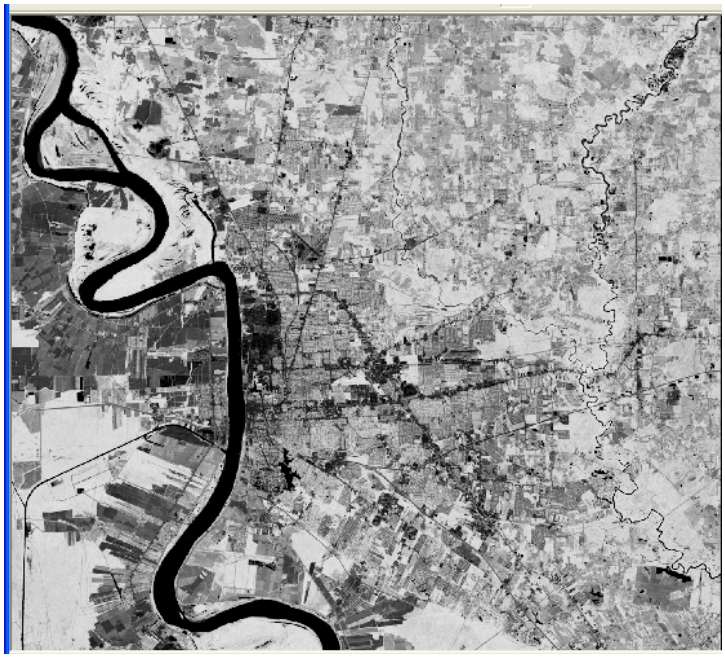

Figure 4.3: LANDSAT 2003 NDVI

To permanently divide the LANDSAT NDVI images into two main categories (vegetation and non-vegetation), the continuous data set must be converted to thematic data layers and recoded so that pixels within the new layer will have a value representing either vegetation or non-vegetation. This is achieved through the ERDAS IMAGINE interpreter module (radiometric enhancement-LUT stretch). The pixel values of the NDVI image are assigned a value of 1 for non-vegetation and 2 for vegetation. In Figure 4.5 for the LANDSAT 1988 data set, non-vegetation is depicted as black and vegetation is depicted as green.

Figure 4.4: Vegetation Delineation for LANDSAT 2003

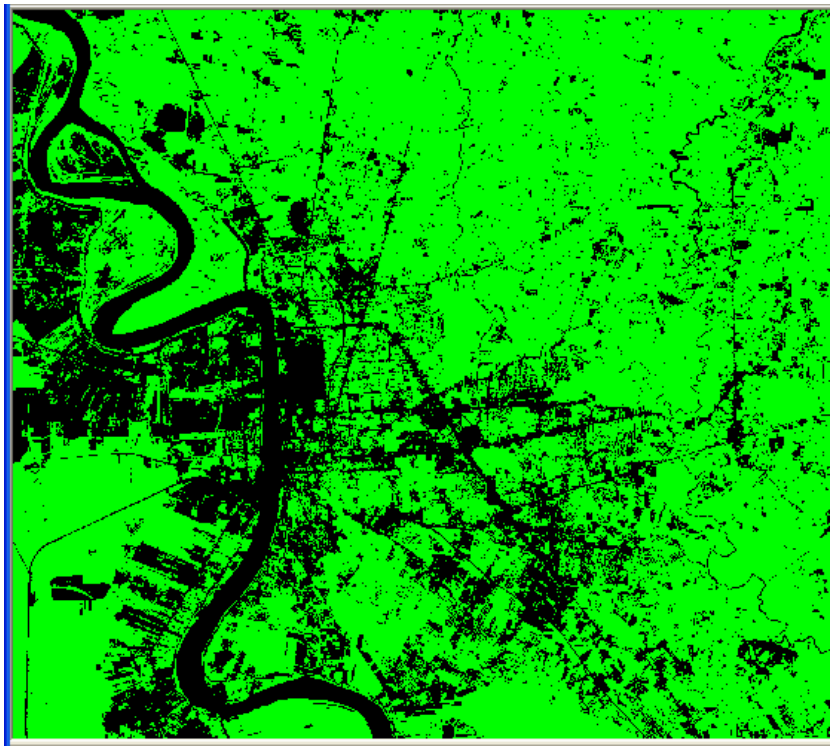

Figure 4.5: LANDSAT 1988 Vegetation and Non-Vegetation Thematic Layer

Once again, abundant vegetation is shown throughout the study region, suggesting that Baton Rouge is more heavily forested than most cities its size. The purpose of the above step is to allow for the creation of masks for both vegetation and non-vegetation. Within the raster

attributes of the above data set, the vegetation class only is selected and saved as an area of interest (AOI) raster layer. This allows for the creation of a vegetated mask for future processing. For example, when viewing the LANDSAT 1988 (3, 4, 5) image and applying the vegetated mask, all vegetation within the (3, 4, 5) image should be masked out and therefore viewed as the color white (Figure 4.6).

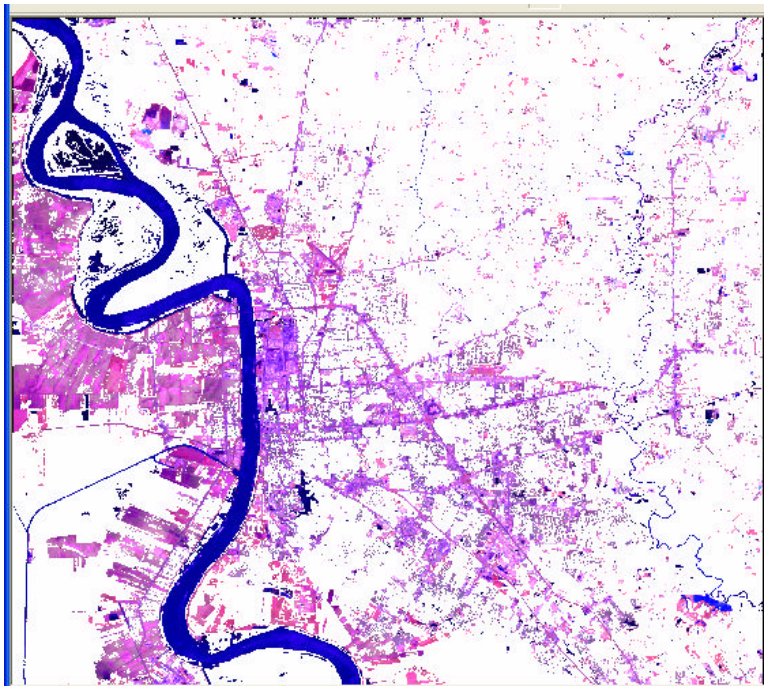

Figure 4.6: LANDSAT 1988 Vegetated Mask

To delineate vegetation-forest and vegetation-non-forest within the overall vegetated raster layer, the vegetated mask is applied to the LANDSAT (3, 4, 5) image. This results in an unsupervised classification process on the vegetated pixels only. Within the ERDAS Classifier Module, an unsupervised classification is performed. Seventy-five classes with a maximum iteration of 25 and a convergence threshold of 0.97 are utilized. The cluster file is ignored in this process. Instead, the signature file is saved as it will be processed through a parametric decision rule to force a better classification. Before this can be achieved, each signature (one signature for each of the 75 classes) is checked to assure that it is homogeneous. Descriptive statistics for

each class are generated and the standard deviation for each band, for each class, is noted to determine whether it is less than 10 percent of the mean. For example, the signature file for the LANDSAT 1988 unsupervised classification to distinguish vegetation-forest from vegetation-non-forest is noted in Figure 4.7. The notation next to "class 3" signifies that once the "statistics" button is selected, the standard deviation for the three bands (3, 4, 5) representing the pixels assigned to that class are calculated (Figure 4.8).

Class #	>	Signature Name	Color	Red	Green	Blue	Value	Order	Count	Prob.	P	I	H	A	FS
1		Class 1		0.005	0.072	0.005	1	1	2910	0.002	X	X	X		
2		Class 2		0.074	0.172	0.074	3	2	1267	0.001	X	X	X		
3	>	Class 3		0.171	0.128	0.171	4	3	2772	0.002	X	X	X		
4		Class 4		0.137	0.099	0.137	5	4	2083	0.002	X	X	X		
5		Class 5		0.172	0.152	0.172	6	5	2168	0.002	X	X	X		
6		Class 6		0.215	0.165	0.215	7	6	1672	0.001	X	X	X		
7		Class 7		0.289	0.148	0.289	8	7	1844	0.002	X	X	X		
8		Class 8		0.239	0.202	0.239	9	8	2326	0.002	X	X	X		
9		Class 9		0.299	0.164	0.299	10	9	5186	0.004	X	X	X		
10		Class 10		0.265	0.228	0.265	11	10	3447	0.003	X	X	X		
11		Class 11		0.347	0.240	0.347	12	11	3311	0.003	X	X	X		
12		Class 12		0.359	0.210	0.359	13	12	6300	0.005	X	X	X		
13		Class 13		0.421	0.206	0.421	14	13	5870	0.005	X	X	X		
14		Class 14		0.274	0.327	0.274	15	14	5230	0.004	X	X	X		
15		Class 15		0.391	0.259	0.391	16	15	9280	0.008	X	X	X		
16		Class 16		0.503	0.230	0.503	17	16	11562	0.010	X	X	X		
17		Class 17		0.419	0.343	0.419	18	17	13603	0.012	X	X	X		
18		Class 18		0.459	0.287	0.459	19	18	9062	0.008	X	X	X		
19		Class 19		0.495	0.276	0.495	20	19	15987	0.014	X	X	X		

Figure 4.7: LANDSAT 1988 Unsupervised Classification-Vegetation Only Signature File

Univariate

Layer	Minimum	Maximum	Mean	Std. Dev.
1	34.000	50.000	43.885	2.416
2	57.000	76.000	64.752	3.630
3	26.000	52.000	42.803	3.411

Figure 4.8: LANDSAT 1988 Unsupervised Classification-Vegetation Only Signature File Standard Deviations for Class 3

Also for each class, the histogram for each band is checked to determine whether a normal distribution exists. For example, Figures 4.9-4.11 depict the histograms of the pixels for each LANDSAT (3, 4, 5) band within Class 3 of the unsupervised vegetation classification.

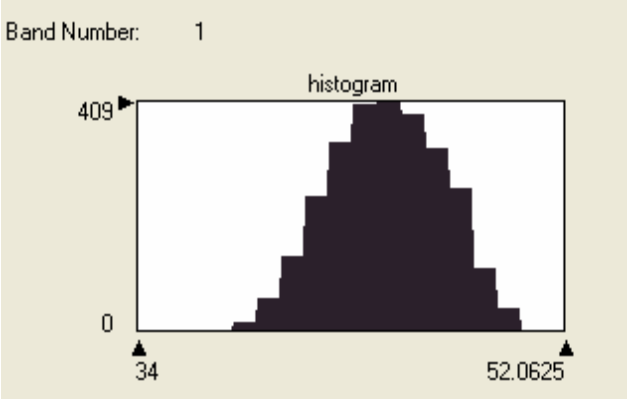

Figure 4.9: LANDSAT 1988 Unsupervised Classification-Vegetation Only Signature File Histogram for Band 1 of Class 3

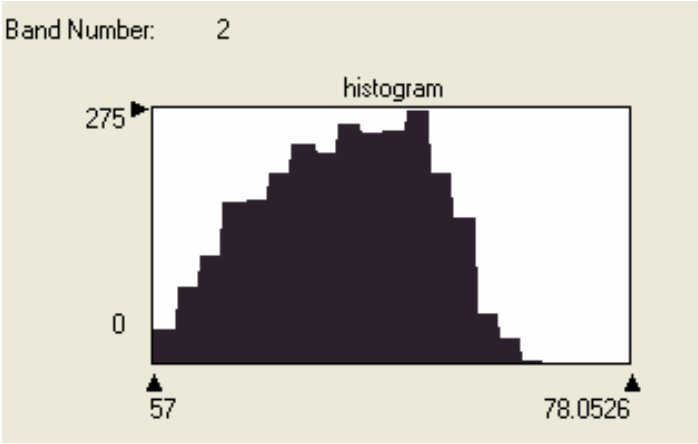

Figure 4.10: LANDSAT 1988 Unsupervised Classification-Vegetation Only Signature File Histogram for Band 2 of Class 3

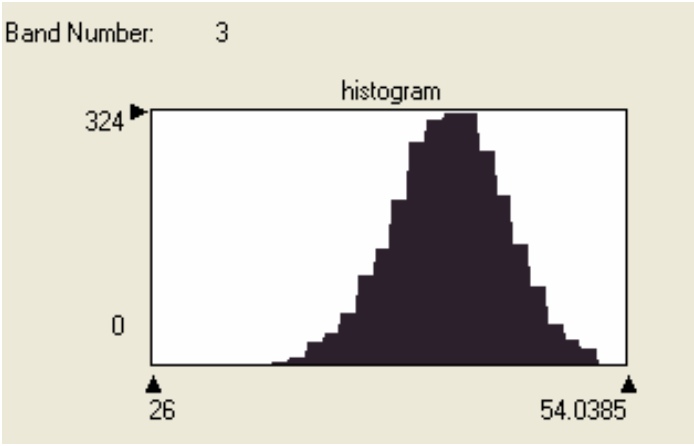

Figure 4.11: LANDSAT 1988 Unsupervised Classification-Vegetation Only Signature File Histogram for Band 3 of Class 3

Once it is determined that the signatures are homogeneous, the signature file is processed through the maximum likelihood parametric decision rule. The count column (representing the number of pixels assigned to each class) is copied into the probability column (see Figure 4.7), and the probabilities are normalized. This allows for the parametric rule to be utilized. The vegetated mask is applied to assure that only vegetated land cover is processed through this isodata classification routine. The results are depicted in Figure 4.12.

Each of the 75 classes generated from the classification performed within the vegetation mask is analyzed to determine whether it is either vegetation-forest or vegetation-non-forest. This is achieved by comparing the vegetated classification layer to that of CIR photography of the same location. In Figure 4.13 below, the viewers within ERDAS IMAGINE are geographically linked.

From the utility drop-down selection within the viewer window, the "inquire" cursor function is used to provide the class value of each identified pixel (Figure 4.14). This allows for the determination of either vegetation-forest or vegetation-non-forest to be noted within the raster attributes of the classified layer. It is determined that class 27 is a vegetation-forest class. Its class color is changed to red (Figure 4.15) to signify that all pixels within this class, throughout the image, are all forested land cover (Figure 4.16). This process is continued for all 75 classes within the vegetated land cover classification. Figure 4.17 depicts the final classified product where vegetation-forest is represented as dark green and vegetation-non-forest is represented as light green. To permanently divide this image into the two vegetation categories, class values representing vegetation-non-forest are assigned a value of 3 and vegetation-forest classes are assigned a value of 4.

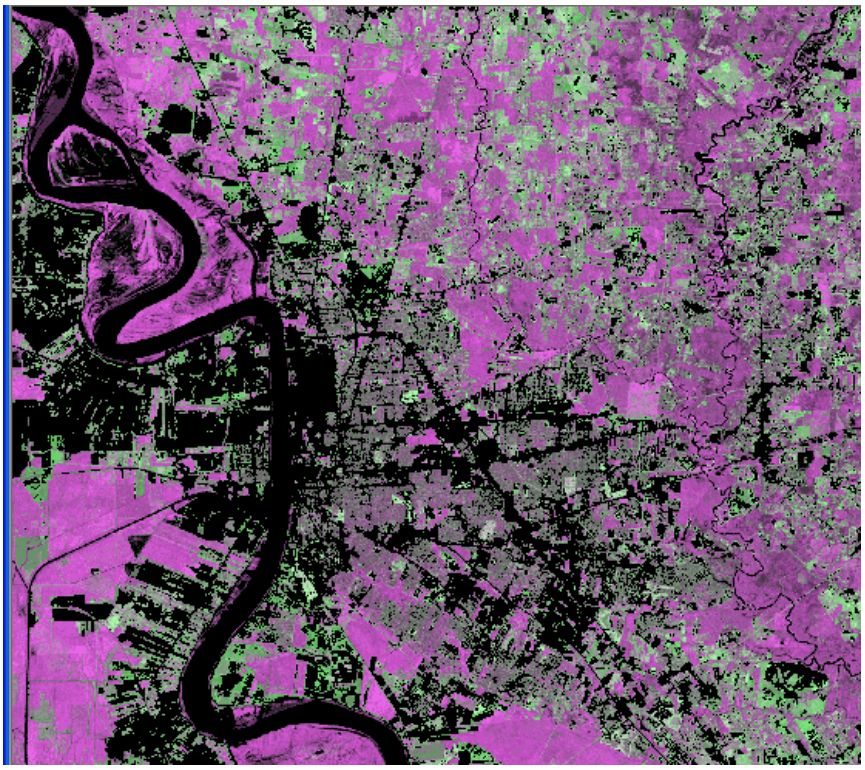

Figure 4.12: LANDSAT 1988 Vegetation Only Classification

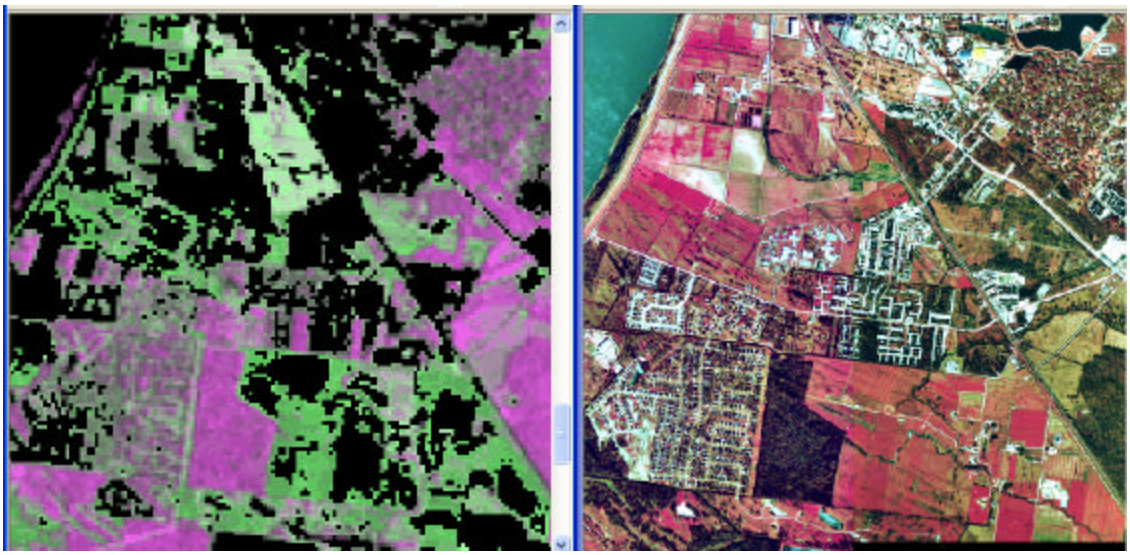

Figure 4.13: Comparison of LANDSAT 1988 Classification of Vegetated Land Cover To Corresponding Color-Infrared Photography

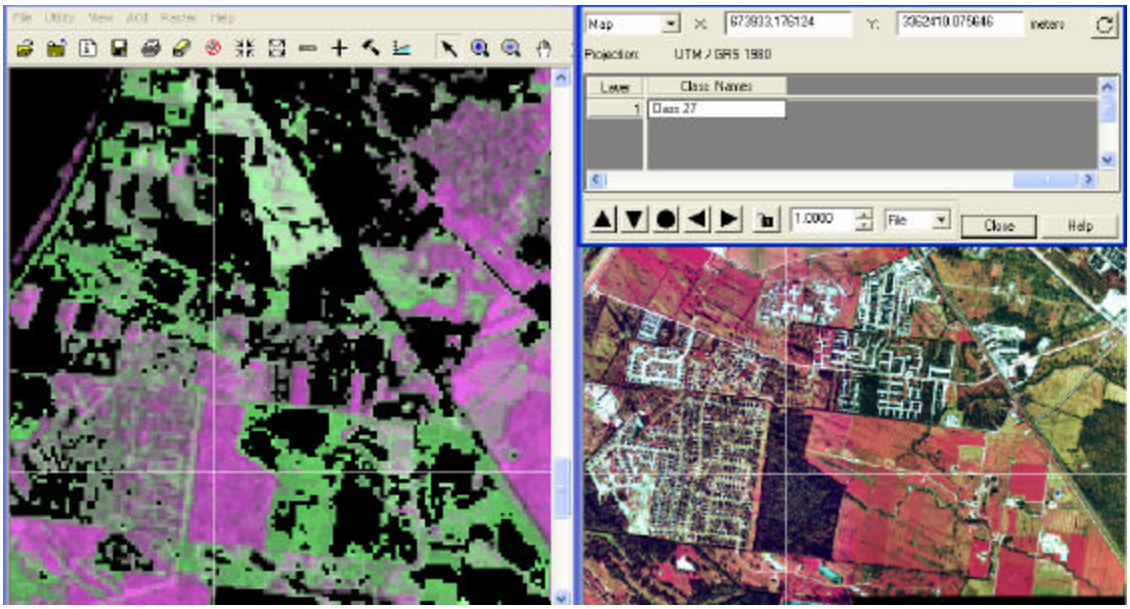

Figure 4.14: Determination of the Vegetation-Forest or Vegetation-Non-Forest From the LANDSAT 1988 Classification of Vegetated Land Cover

Row	Histogram	Color	Red	Green
21	16064		0.54	0.32
22	22514		0.55	0.31
23	23296		0.6	0.27
24	30668		0.61	0.34
25	36730		0.64	0.31
26	37861		0.69	0.29
27	66291		1	0
28	50868		0.76	0.31
29	64469		0.81	0.35
30	25906		0.91	0.4
31	23696		0.76	0.39

Figure 4.15: Raster Attributes of the LANDSAT 1988 Vegetated Land Cover Classification

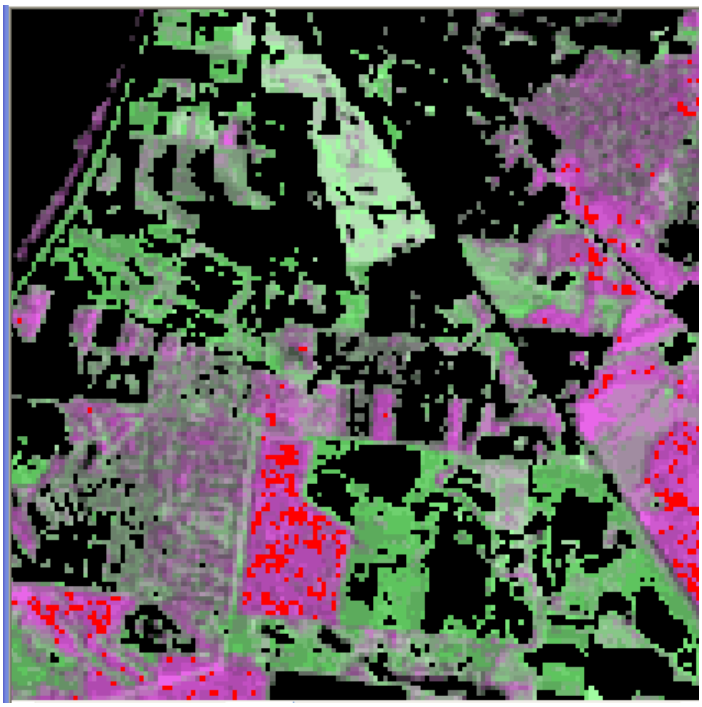

Figure 4.16: Re-coloring of Class 27 throughout the LANDSAT 1988 Vegetated Land Cover Classification

Analogous to the vegetation/non-vegetation categorization produced as a result of the NDVI calculation, a combined category of urban, bare land, and water is created. As explained earlier, masks are needed in order to set processing limits. Therefore, within the raster attributes of the NDVI thematic layer, the non-vegetation class only is selected and saved as an AOI raster layer. This allows for the creation of a non-vegetated mask. For example, when viewing the LANDSAT 1988 (3, 4, 5) image and applying the non-vegetated mask, all non-vegetation within the (3, 4, 5) image are masked out and therefore viewed as the color white (Figure 4.18).

Following the same procedure and using the same parameters as outlined previously, Figure 4.19 depicts the resultant classification performed on the non-vegetated pixels within the 1988 LANDSAT (3, 4, 5) image. Following the same procedure as outlined for the vegetated land cover lasses, each of the 75 classes generated within the non-vegetation mask are analyzed to determine whether they are either water, urbanized land, or bare land.

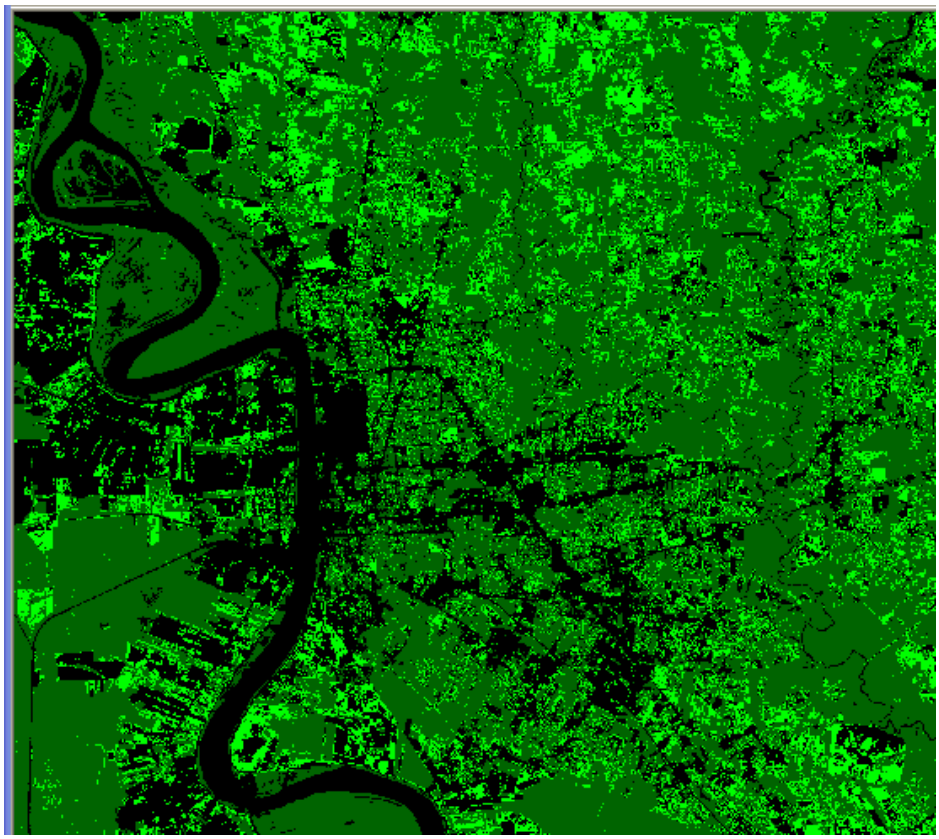

Figure 4.17: Final Classification of Vegetation within the LANDSAT 1988 Data Set

To permanently divide this image into the three non-vegetated categories, class values representing water are assigned a value of 5, urban classes are assigned a value of 6, and bare land classes are assigned a value of 7. Figure 4.20 depicts the final classified product, representing water as blue, urban as red, and bare land as tan.

4.4.2 Accuracy Assessment for the LANDSAT Land Cover Classifications

An accuracy assessment allows for the evaluation of classified imagery when it is represented as a thematic raster layer. Within the ERDAS IMAGINE classifier module, the accuracy assessment CellArray is used to compare the classification with ground truth data.

Figure 4.18: LANDSAT 1988 Non-vegetated Mask

For this study, classification polygons for urban, bare land, vegetation-forest, vegetation-non forest, and water are validated against actual land cover as depicted in 1998 and 2004 Digital Ortho Quarter Quads (DOQQs) for the 1988 and 2003 study area, respectively. Figure 4.21 shows 200 randomly-selected points within the study area overlaid on the 1988 classified LANDSAT data set. The cell array lists two sets of values for these points: class and reference values. Class values are automatically assigned to the random points as they are selected, and reference values are user-defined. An example of the cell array for the 1988 LANDSAT classification is shown in Figure 4.22.

Figure 4.23 shows a zoomed view depicting ID point #80. Class values are determined by the 1988 LANDSAT classification scheme. A visual interpretation of the corresponding DOQQ (Figure 4.24) determines the reference value, or true class, for ID point #80. In this example, both the class and reference values indicate water.

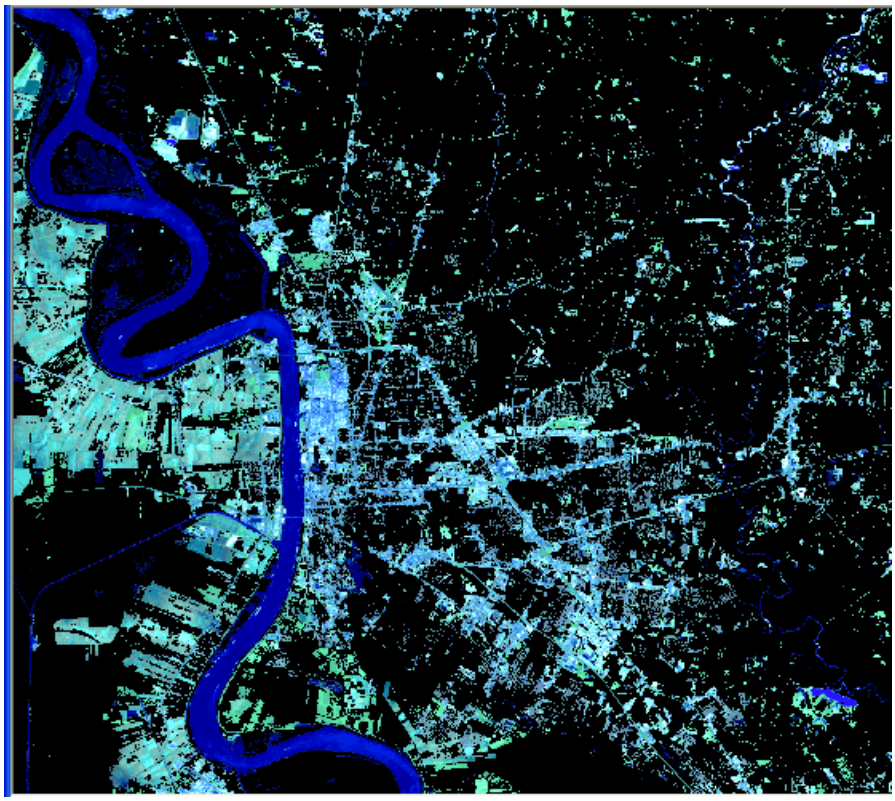

Figure 4.19: LANDSAT 1988 Non-Vegetation Only Classification

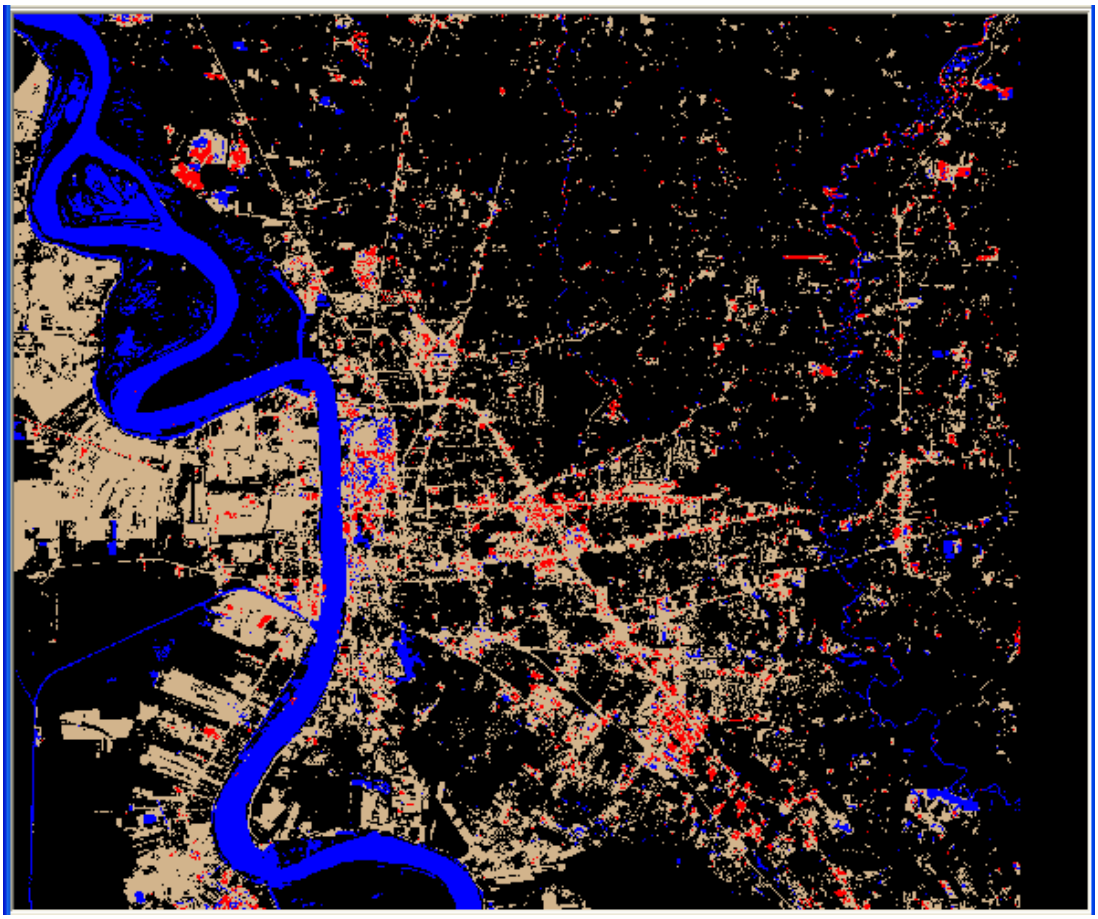

Figure 4.20: Final Classification of Non-Vegetation within the LANDSAT 1988 Data

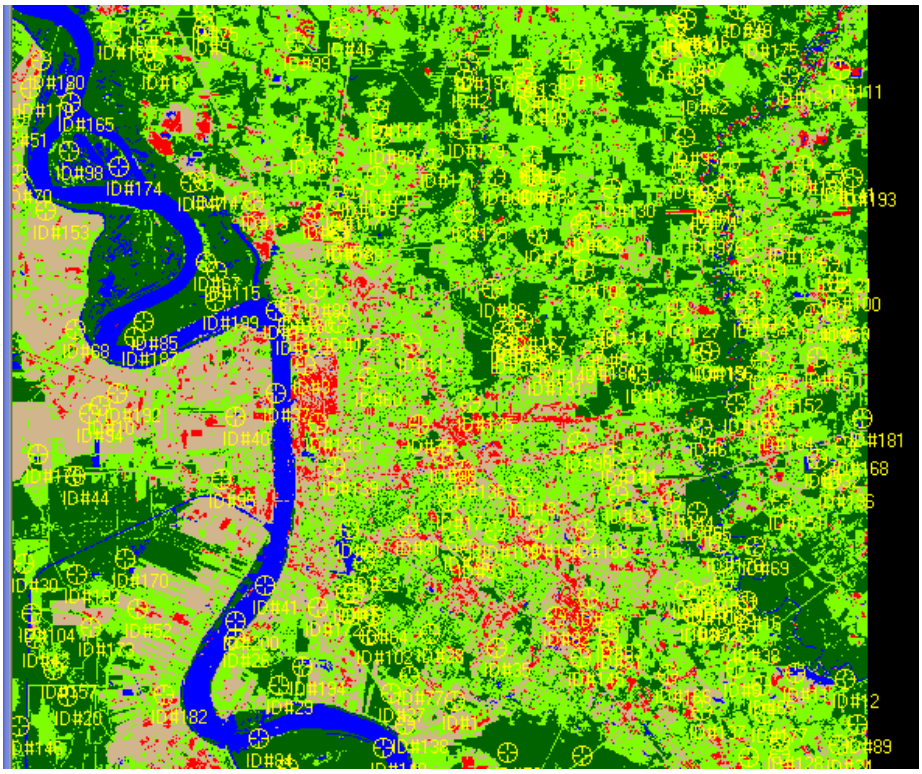

Figure 4.21: Randomly Selected Ground Truth Locations for the Final Classification of the 1988 LANDSAT Data Set

Once both class values are determined, an accuracy report is generated within the ERDAS IMAGINE Accuracy Assessment tool. First, an error matrix compares the reference class values to the assigned class values in a c x c matrix, where c is the number of classes (including class 0). The accuracy totals report then calculates statistics of the percentages of accuracy, based upon the results of the error matrix. An overall classification accuracy of 87.5 and 83 percent was achieved for the 1988 and 2003 LANDSAT classification datasets, respectively.

Point #	Name	X	Y	Class	Reference
1	ID#1	681317.000	3359460.000	4	4
2	ID#2	681797.000	3388890.000	4	4
3	ID#3	674267.000	3375390.000	7	6
4	ID#4	689777.000	3371130.000	3	3
5	ID#5	688457.000	3376650.000	3	3
6	ID#6	693047.000	3372420.000	4	4
7	ID#7	676517.000	3364620.000	3	3
8	ID#8	694697.000	3361020.000	3	3
9	ID#9	669407.000	3391410.000	3	3
10	ID#10	664487.000	3373440.000	7	7
11	ID#11	697517.000	3360840.000	5	5
12	ID#12	699887.000	3360510.000	4	4
13	ID#13	690077.000	3374940.000	4	4
14	ID#14	688877.000	3377670.000	4	3
15	ID#15	676127.000	3364560.000	3	3
16	ID#16	695237.000	3364230.000	4	4
17	ID#17	681047.000	3368940.000	4	4
18	ID#18	667067.000	3389760.000	3	3
19	ID#19	671837.000	3383160.000	7	7
20	ID#20	662957.000	3359730.000	4	4
21	ID#21	666587.000	3391620.000	5	5
22	ID#22	677027.000	3366030.000	4	4
23	ID#23	687557.000	3382170.000	3	3
24	ID#24	699587.000	3357420.000	3	3
25	ID#25	673397.000	3356280.000	4	4
26	ID#26	670907.000	3362430.000	4	4
27	ID#27	678317.000	3359820.000	7	7
28	ID#28	680177.000	3362670.000	4	4
29	ID#29	672947.000	3360240.000	4	4
30	ID#30	660887.000	3366000.000	3	7
31	ID#31	694097.000	3365190.000	3	3
32	ID#32	695867.000	3375630.000	3	3
33	ID#33	687677.000	3364350.000	3	3
34	ID#34	695267.000	3356850.000	3	3
35	ID#35	683357.000	3361980.000	3	3
36	ID#36	683087.000	3378960.000	3	3
37	ID#37	672827.000	3374010.000	5	5
38	ID#38	695177.000	3362670.000	4	4

Figure 4.22: Cell Array for the Random Points Generation of the 1988 LANDSAT Classified Data Set

4.4.3 Applying the ATLAS Regression Equations

The land cover classification scheme for this study consists of five categories: urban, bare land, water, vegetation-forest, and vegetation-other. Representative land cover polygons for each category are created through onscreen digitizing from flight line #5 of the 1998 ATLAS data set. Corresponding ATLAS surface temperature and NDVI values are extracted for each land cover polygon and are used to derive regression equations for each land cover category. Regression equations from the 1998 ATLAS data set are developed to predict surface temperature from known NDVIs of corresponding land cover polygons within the 1988 and 2003 LANDSAT classification data sets. For example, the left image in Figure 4.25 represents the

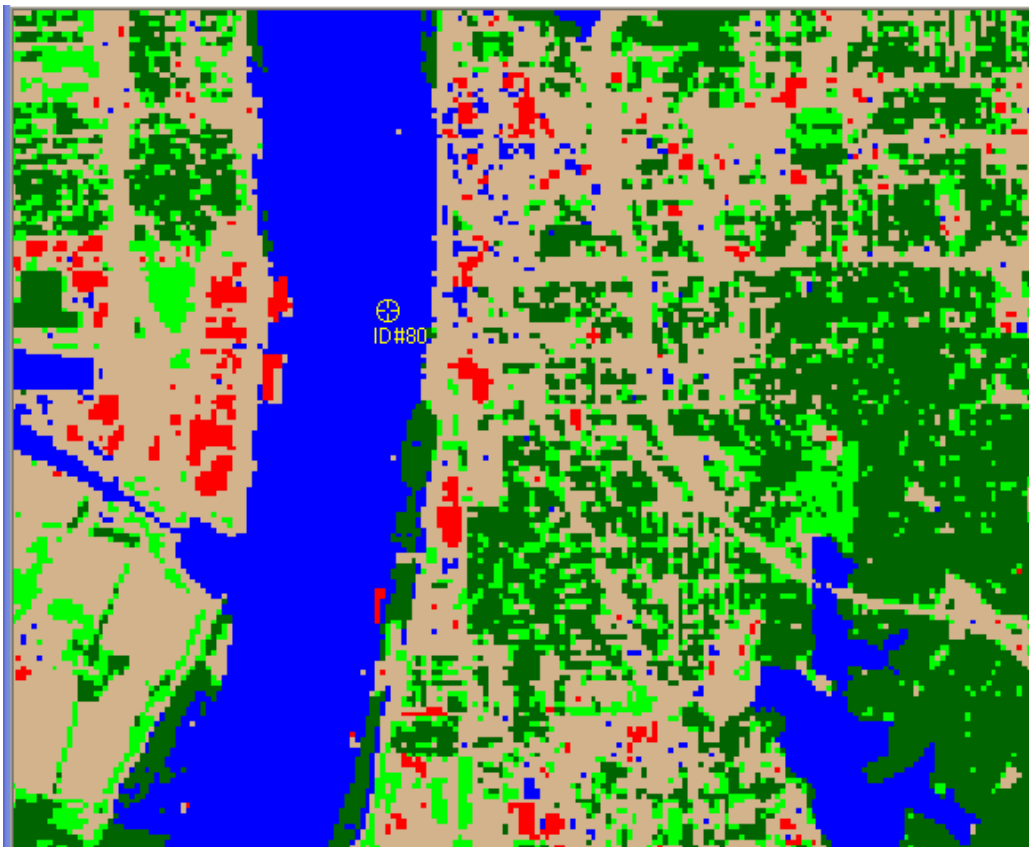

Figure 4.23: Example of a Class Value ID Point within the 1988 LANDSAT Classified Data Set

1988 land classification scheme of which urban polygons are highlighted in red. The urban polygons are selected as an AOI raster layer within the overall classification image, thus providing a mask to subset corresponding NDVI values from the 1998 LANDSAT NDVI image. This allows for the creation of a 1988 urban land cover NDVI image (Figure 4.25, right image). This process is carried out for all land cover categories for both the 1988 and 2003 LANDSAT data sets.

Utilizing the 1998 regression equation for urban land cover ($y = -9.2569(x) + 47.64106$), the average surface temperatures (y) for corresponding 1988 urban land cover are predicted based upon 1988 urban land cover NDVI values (x). This is made possible with ERDAS

Figure 4.24: Example of a Reference Value ID Point within the 1988 LANDSAT Classified Data Set

IMAGINE Spatial Modeler (Figure 4.26). The 1988 predicted surface temperatures for urban land cover are shown in Figure 4.27. All land cover polygons from each LANDSAT data set (1988 and 2003) are now assigned corresponding predicted surface temperature values.

4.5 CHAPTER SUMMARY

This chapter described the major results of the tests of the research hypotheses outlined in Chapter 1. First, a Spearman correlation coefficient of 0.901 confirmed a relationship between the T_a and MSE variables. Additional analysis identified a significant linear temporal decrease in MSE, but no significant linear trend in T_a. Although any deforestation coincident with development may have had a negligible effect on the UHI of Baton Rouge, an evaluation of the

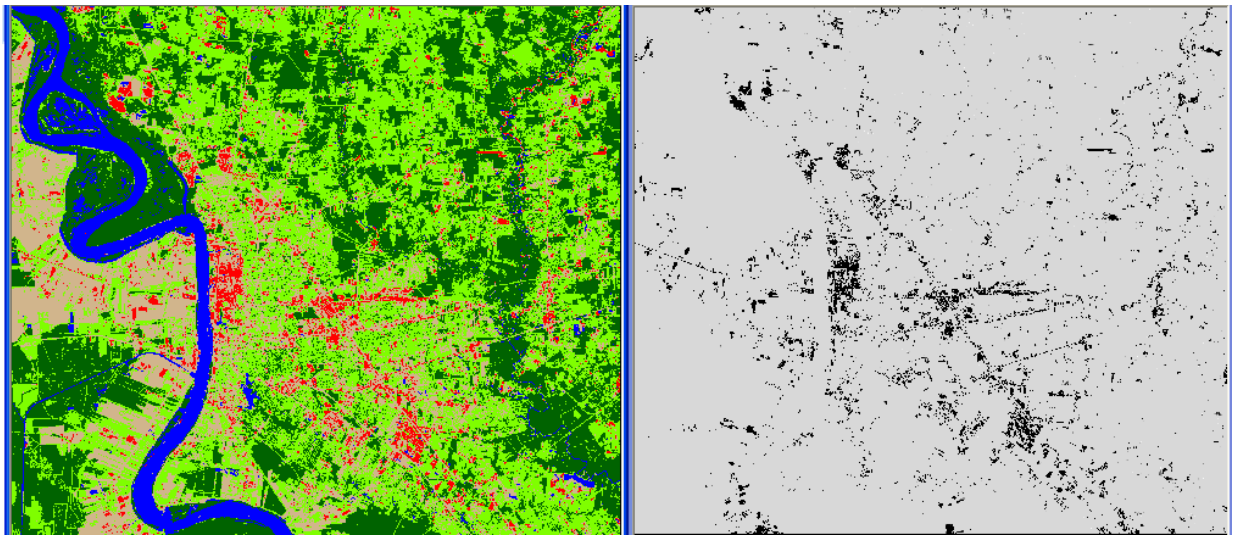

Figure 4.25: 1988 LANDSAT Classification and Urban NDVI Values

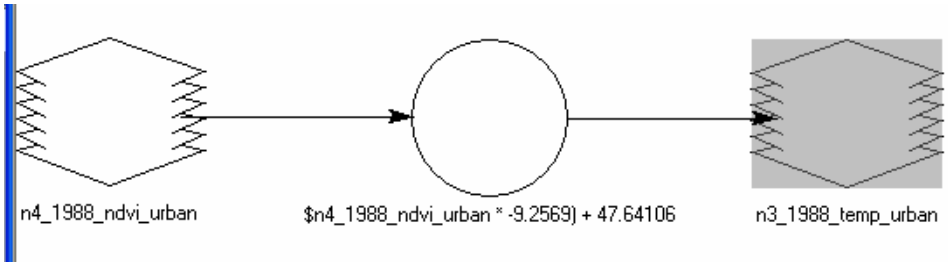

Figure 4.26: 1988 LANDSAT Classification and Urban NDVI Values

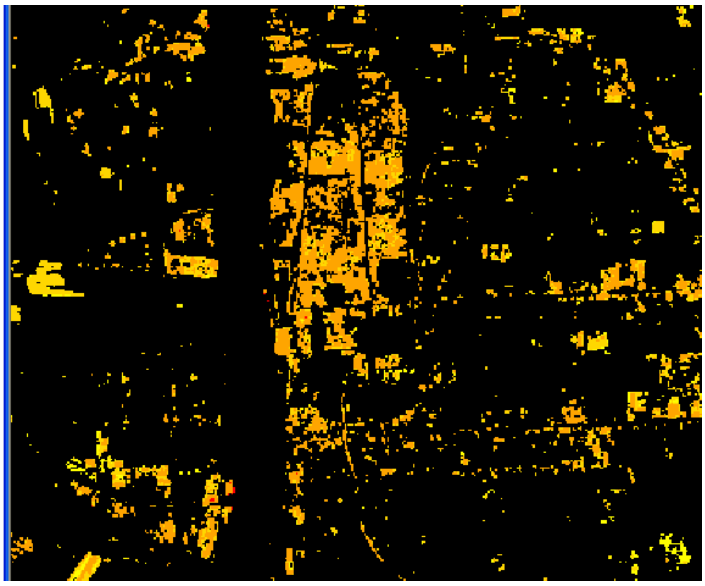

Figure 4.27: 1988 Predicted Surface Temperature for Urban Land Cover

SHI as a function of land cover throughout the study period was performed. A land classification scheme was carried out on two LANDSAT data sets from 1988 and 2003. The land cover classification scheme for this study consisted of five categories: urban, bare land, water, vegetation-forest, and vegetation-other. Corresponding surface temperature and NDVI values for these five land cover categories were extracted from the 1998 ATLAS data set. Regression equations were developed to predict surface temperature from known NDVIs of corresponding land cover polygons within the 1988 and 2003 LANDSAT classification data sets. The following chapter describes the conclusions of this analysis.

CHAPTER 5. CONCLUSIONS

5.1 OVERVIEW

This chapter will summarize the conclusions of the tests of the research hypotheses described in Chapter 4. The major implications of these conclusions are also discussed to provide a better understanding of the spatial and temporal properties of the Baton Rouge SHI.

5.2 SURFACE AIR TEMPERATURE AND MSE

For the time period of May 1993 to May 2003, ASOS maximum daily T_a data, along with corresponding derived MSE values, are analyzed for the study area. A Spearman correlation coefficient of 0.901 between T_a and MSE is computed. It is not surprising that the two variables are highly correlated, particularly since T_a is a component of MSE. To investigate temporal trends, T_a and observation number are correlated, along with daily MSE and observation number. A significantly decreasing linear temporal trend in MSE ($r = -0.07$, p-value = 0.00005) was identified from 1993 to 2003, but no significant linear temporal trend in T_a ($r = -0.02$, p-value = 0.22) occurred. To analyze this relationship further, the monthly average of both variables is plotted for the study period. A visual interpretation confirms that both variables simultaneously experience seasonality effects from monthly temperature changes.

In conclusion, the maximum T_a-defined UHI of Baton Rouge has not changed significantly over the study period. Given that the study area was indeed undergoing land cover changes during the study period, it is possible that a single ASOS location is not indicative of surface temperature changes throughout the entire study area. Although the local forest cover may mask the UHI and SHI effect, local micro-climates are not being accurately depicted

between meteorological stations. This claim is further substantiated in the following sections, in which the spatial resolution of a remotely-sensed, surface temperature-derived SHI reveals microscale differences that the surface air temperature-derived UHI is unable to depict.

The study area, especially because of its availability of nearby surface water, has a unique climate. Therefore, although these results suggest that the MSE is a more appropriate indicator of the UHI presence over time than surface air measurements, it is important to note these findings are specific to the Baton Rouge area.

5.3 SPATIAL ANALYSIS OF THE UHI *VS*. SHI

The ATLAS data set was collected within a two-day period, 11-12 May 1998. The T_a-derived UHI originates from daily temperature point data and two data sets are required to match the temporal scale of the ATLAS data. The point shapefile representing the UHI is spatially interpolated to produce a continuous surface (raster) comparable to that of the ATLAS data. Within ArcMap's Spatial Analyst extension, the Inverse Distance Weighted (IDW) method is used to interpolate the shapefile into a raster data set in order for contours to be generated. It is important to acknowledge the limitation of the IDW method. Although IDW assigns more weight to nearby points than to distant points, the weighting method can be easily affected by uneven distributions of data points since an equal weight will be assigned to each of the points even if it is in a cluster (Lam 1983). Figure 5.1 is the raster image depicting the continuous surface of the average maximum daily temperature for the study area during 11-12 May 1998. The T_a-derived UHI represents only a two 2 C° change and only indicates two surface hot spots across the entire study area.

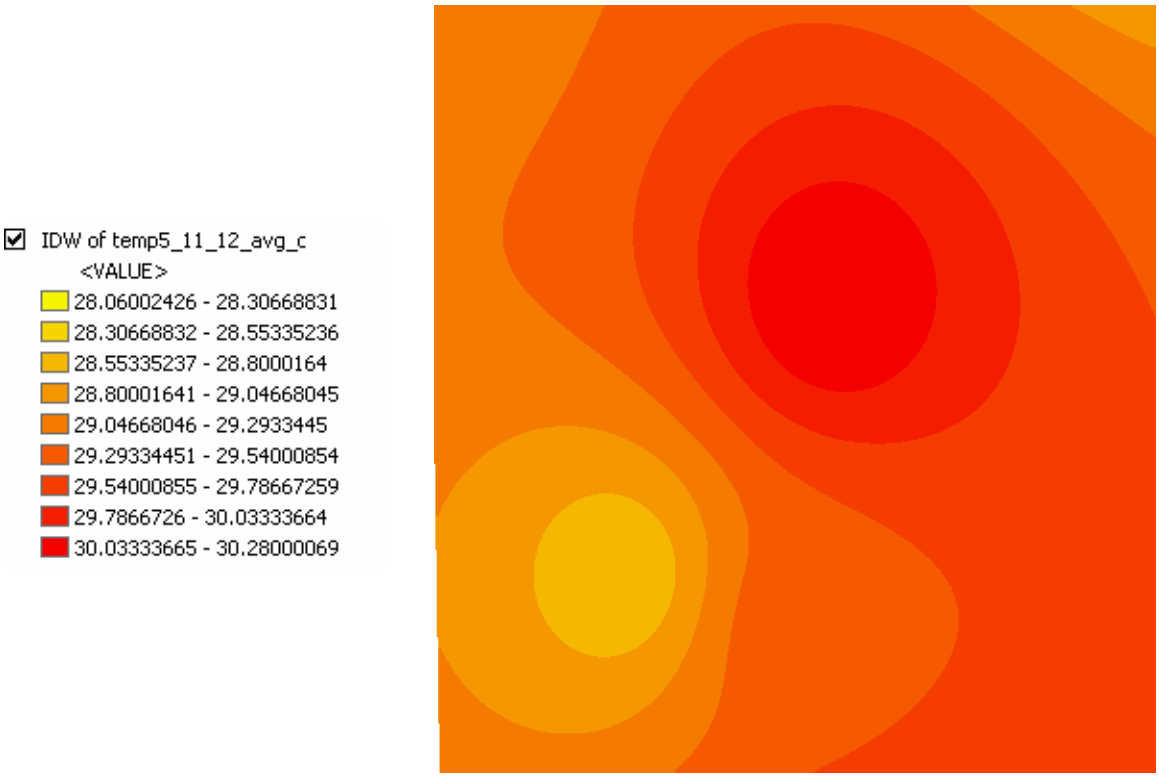

Figure 5.1: The Surface UHI (T_a-derived UHI) during 11-12 May 1998 Represented as a Continuous Surface

When compared to the spatial resolution of the ATLAS dataset, the surface depicted in Figure 5.1 does not portray an accurate representation of distinct changes in surface temperature across the study area. For example, Figure 5.2 represents the ATLAS remotely-sensed surface of which a temperature range of approximately 57 C° is depicted. This is further explored in Figures 5.3 and 5.4 with overlays of surface temperature contours plotted against temperature as a continuous surface. In Figure 5.3, the contours representing the T_a-derived UHI are plotted at a 3.5 Cº interval against the remotely-sensed SHI. In Figure 5.4, the contours representing the remotely-sensed SHI are plotted at a 10.0 Cº interval against the T_a-derived UHI surface.

The ATLAS area of coverage extends to approximately 2600 km^2 at a spatial resolution of 10 m and within this coverage, only four meteorological stations provide daily maximum T_a recordings. The locations of these stations are shown in Figure 5.5. When a spatial interpolation

is performed to compare the spatial pattern of the T_a-derived UHI to that of the remotely-sensed, surface temperature-derived SHI, it is evident that the spatial resolution of the current network of surface meteorological stations cannot accurately portray the many micro-SHIs (or hot spots) throughout the study area.

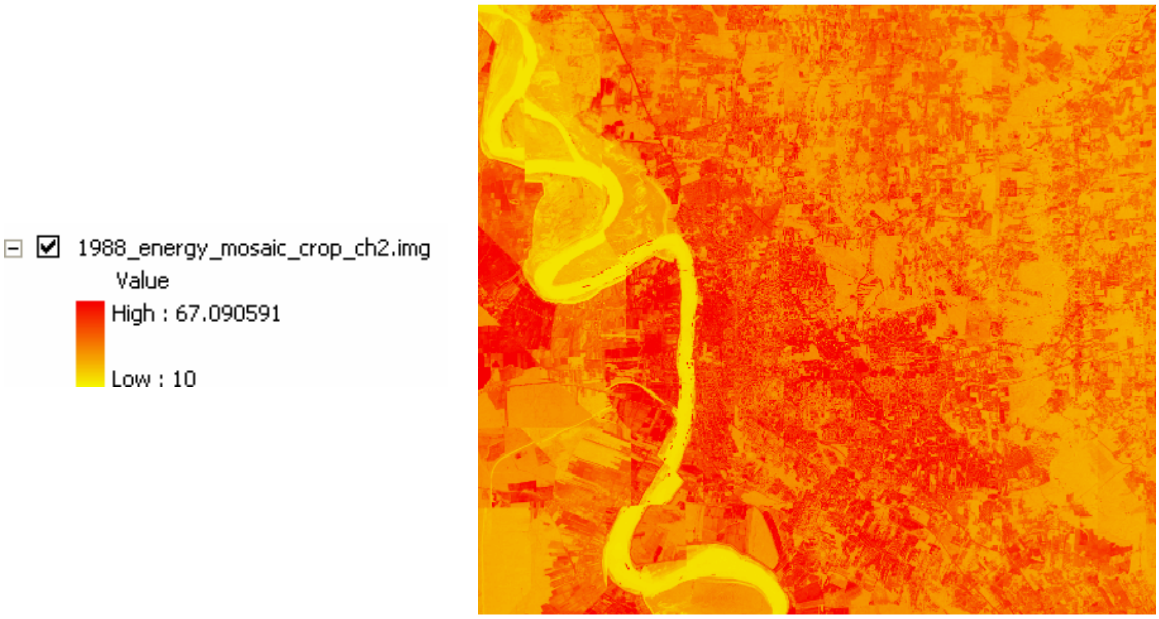

Figure 5.2: The ATLAS Remotely-Sensed SHI
11-12 May 1998

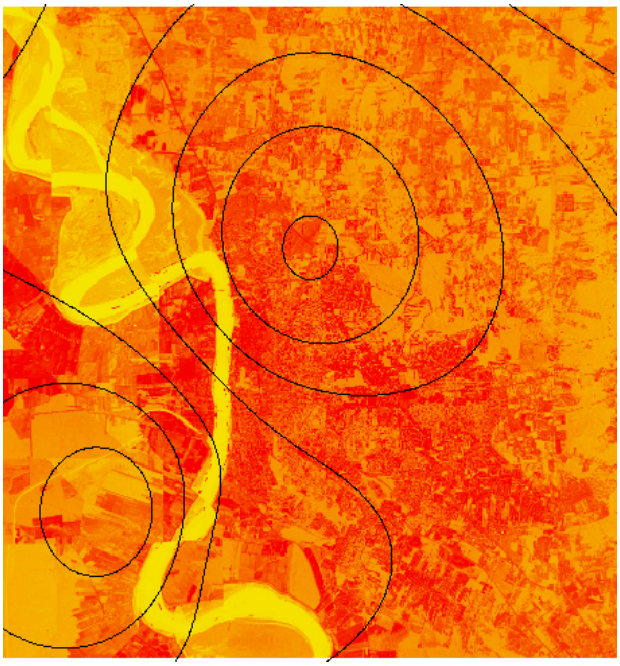

Figure 5.3: T_a-derived UHI Contours Plotted against the Remotely-sensed SHI

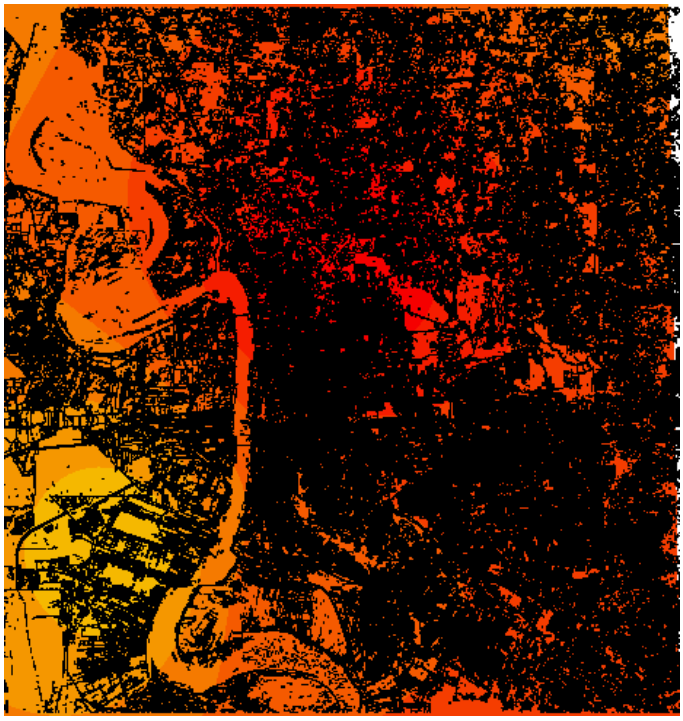

Figure 5.4: Remotely-sensed SHI Contours plotted against the T_a-derived UHI

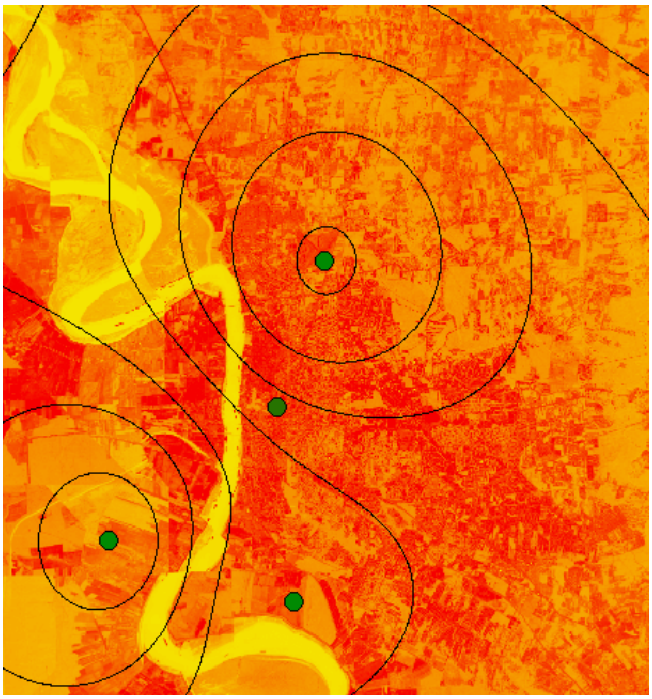

Figure 5.5: Locations of Meteorological Stations Providing Daily Maximum T_a Recordings

5.4 TEMPORAL ANALYSIS OF THE UHI *VS*. SHI

To evaluate the SHI as a function of land cover, and to investigate the thermal efficiency of urban land cover with respect to the potential impact of tree growth within the study area, five land classification categories are delineated within the study area: urban, bare land, vegetation-forest, vegetation-non-forest, and water. To begin the classification process, an NDVI calculation provides the initial means to differentiate vegetation from non-vegetation. From a visual comparison of NDVIs for 1988 and 2003, it is hard to determine whether are not vegetation amounts have changed over the fifteen-year study period (Figure 5.6).

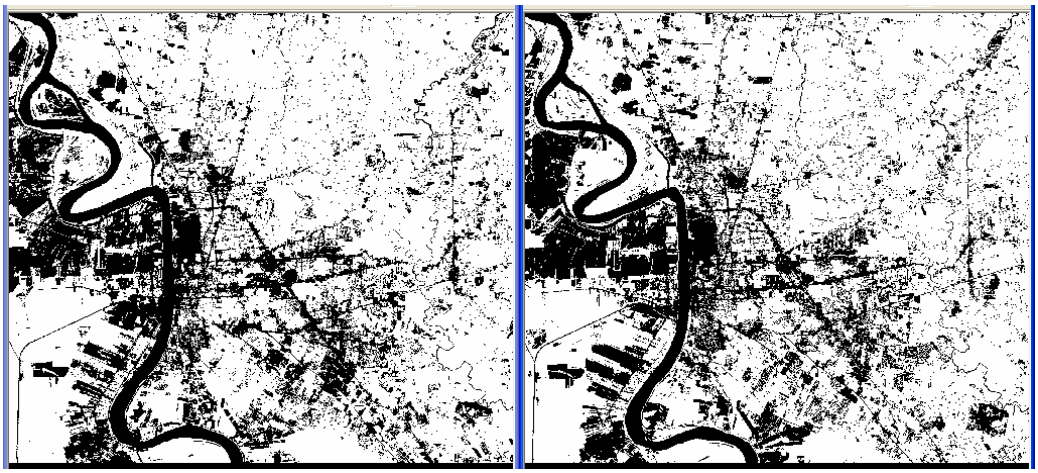

Figure 5.6: LANDSAT NDVIs for 1988 (left) and 2003 (right)

From previous processing steps described in Chapter 4, the NDVI images for both 1988 and 2003 are recoded. Non-vegetated pixels are assigned a value of one and vegetated pixels are assigned a value of two. A closer evaluation of the histogram and area (square miles) values from Figure 5.7 below validates that net vegetation cover has remained somewhat constant over the fifteen-year study period.

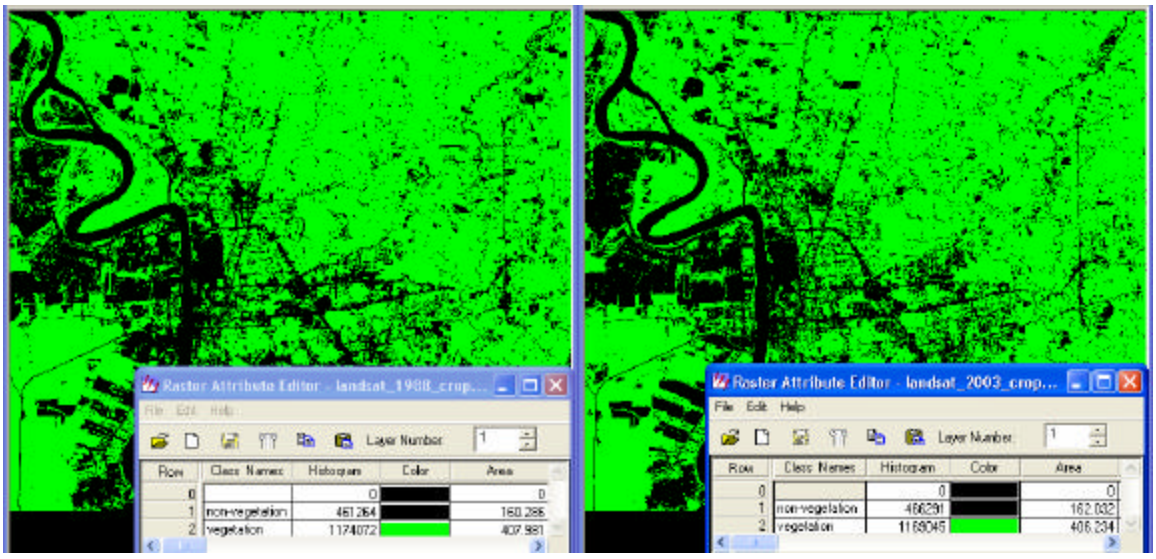

Figure 5.7: LANDSAT Vegetation Amounts for 1988 (left) and 2003 (right)

The NDVI products allow for the creation of vegetation and non-vegetation masks to be applied during the classification process of both LANDSAT datasets. The classification of only vegetated pixels allows for the determination between vegetation-forest and vegetation-non-forest. From a visual comparison of the vegetated classifications for 1988 and 2003, it appears that vegetation-forest has increased in area over the fifteen-year study period (Figure 5.8). However, a closer evaluation of the histograms and area calculations for these images also indicates a decrease in vegetation-non-forest.

Using the non-vegetation mask to classify only non-vegetated pixels allows for the determination of water, urban area, and bare land. From a comparison of the histograms and area calculations for these images, there is a decrease in water and urban land areas and an increase in bare land. Figure 5.9 depicts the change within the non-vegetated land cover classes between 1988 and 2003.

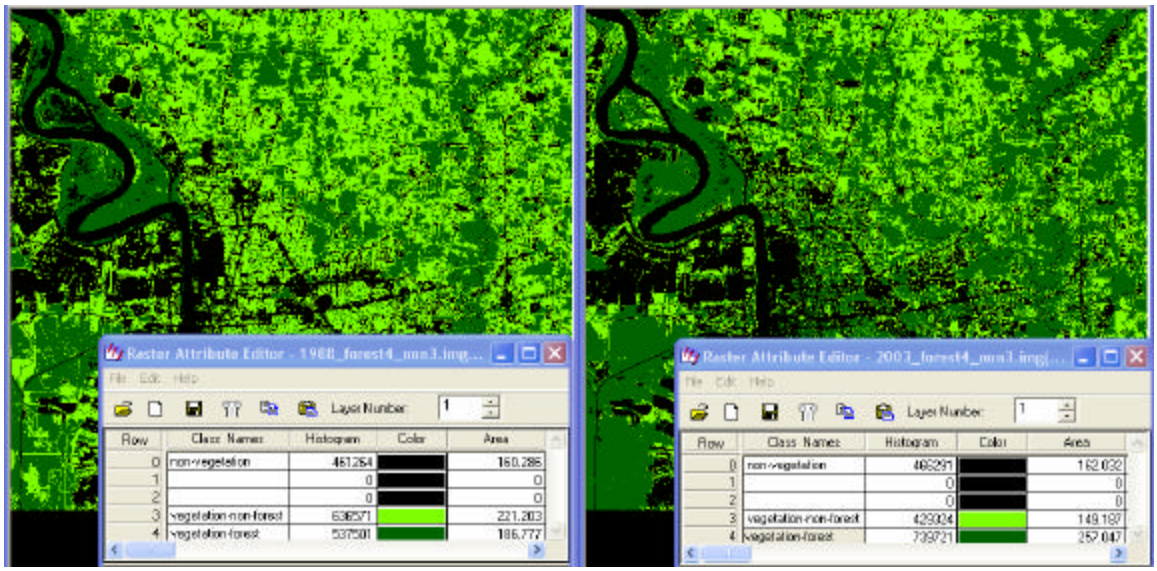

Figure 5.8: Vegetation-forest (light green) and Vegetation-non-forest (dark green) for LANDSAT 1988 (left) and 2003 (right)

Although the overall classification accuracies for both the 1988 and 2003 LANDSAT classification schemes were good (87.5 and 83 percent, respectively), the individual accuracies for urban and bare land are not (Tables 5.1 and 5.2). This offers one explanation of the anomalous finding that urban land cover has decreased over the study period. Furthermore, all image data sets for this study were each acquired during mid-May when tree canopy is prevalent throughout the study area. This is one possible factor for the under-representation of urban classes, especially within suburban areas.

Corresponding changes in land surface temperature during this 15-year study period are evaluated by applying regression equations to predict surface temperature from known NDVI values. From the 1998 ATLAS regression equations for each land cover type (Table 5.3), surface temperatures (y) for corresponding 1988 and 2003 LANDSAT land cover polygons are predicted based upon their corresponding NDVI values (x).

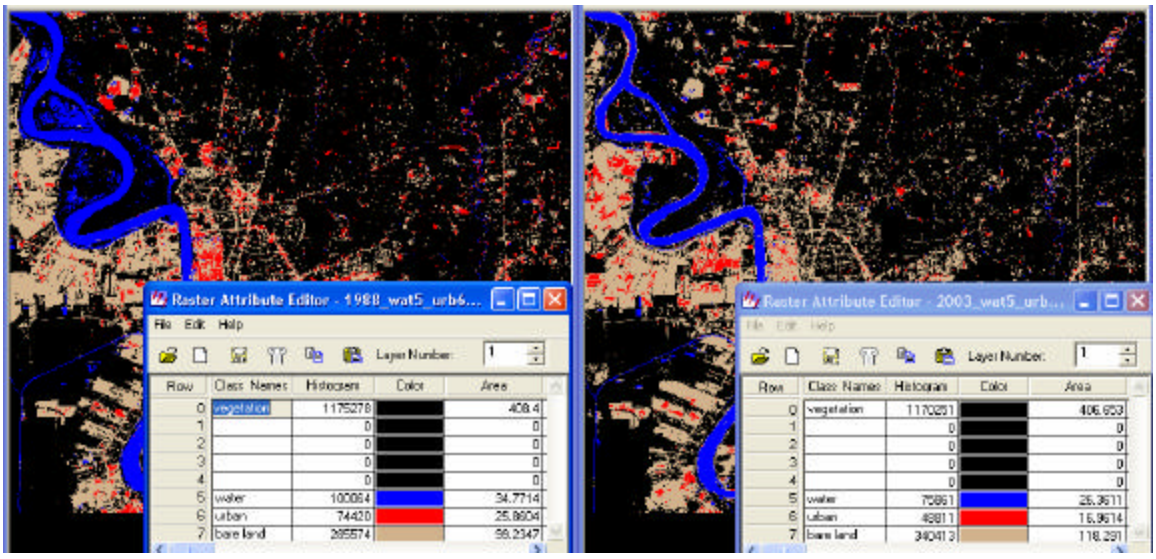

Figure 5.9: Water as Blue, Urban as Red, and Bare Land as Tan
for LANDSAT 1988 (left) and 2003 (right)

Table 5.1: 1988 Land Classification Accuracy Table

Class Name	Reference Totals	Classified Totals	Number Correct	Producers Accuracy (%)	Users Accuracy (%)
Veg Non-Forest	89	87	84	94.38	96.55
Veg Forest	59	63	57	96.61	99.48
Water	13	13	12	92.31	92.31
Urban	17	13	7	41.18	53.85
Bare Land	22	24	15	68.18	62.50

Table 5.2: 2003 Land Classification Accuracy Table

Class Name	Reference Totals	Classified Totals	Number Correct	Producers Accuracy (%)	Users Accuracy (%)
Veg Non-Forest	52	46	41	78.85	89.13
Veg Forest	105	111	98	93.33	88.29
Water	7	7	6	85.71	85.71
Urban	13	4	2	15.38	50.00
Bare Land	23	32	19	82.61	59.38

Although no assumptions were violated, it is important to note the limitation of the regression equations used in this study. The prediction of surface temperatures for 1988 and 2003 is based upon the 1998 surface temperature acquired at one particular point in time. Although all image data from both the ATLAS and LANDSAT sensors were acquired in mid-May, we must be cautious to assume that different daily meteorological conditions would not affect local surface temperatures and thus obscure the NDVI-surface temperature correlation. Regardless, for the study area as a whole, individual land conversion did in fact play a role in the overall effect on surface temperature. This is illustrated in the 1988 and 2003 predicted surface temperatures in Figure 5.10.

5.5 EVALUATING THE RESEARCH HYPOTHESES

This study relied on the theoretical premise that increases in surface thermal emissions are directly related to increases in near-surface atmospheric temperatures, and even though UHIs can be measured as either atmospheric or surface phenomena, this study used remotely-sensed

Table 5.3: Results from 1998 ATLAS Regression Equations

Land Cover	1988 Regression Equation ºC	1988 Minimum Temperature ºC	2003 Minimum Temperature ºC	1988 Maximum Temperature ºC	2003 Maximum Temperature ºC
Water n=1060 r^2=0.026	Y = 2.94x + 22.41	20	19	21	23
Forest n=2737 r^2=0.0008	Y = -0.47x + 31.32	31	31	31	31
Veg-Non Forest n=105 r^2=0.074	Y = -8.67x + 44.35	39	38	43	41
Bare Land n=4815 r^2=0.112	Y = 7.58x + 50.82	47	47	49	53
Urban n=6565 r^2=0.005	Y = -9.26x + 47.64	48	44	51	48

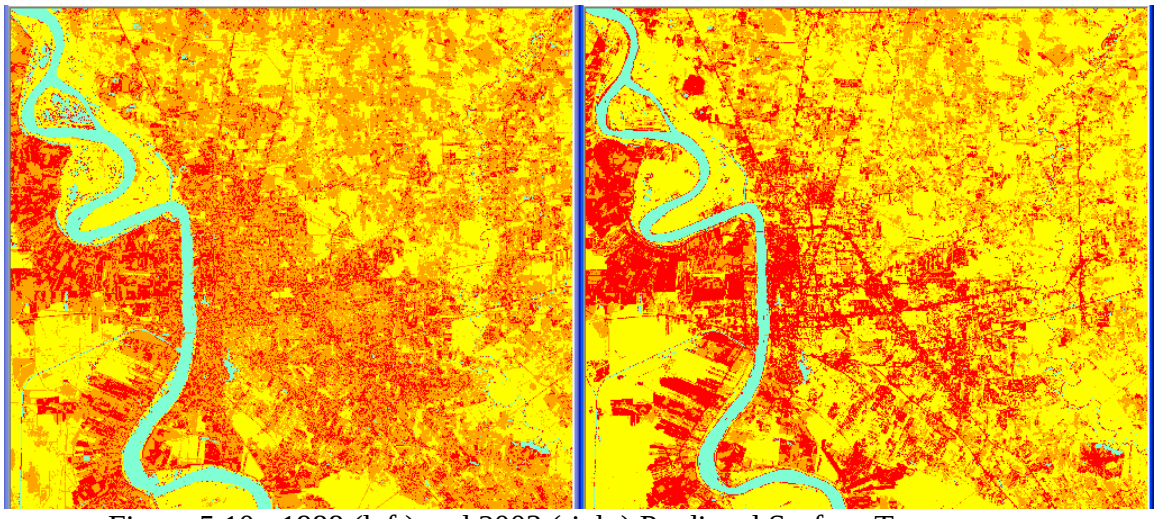

Figure 5.10: 1988 (left) and 2003 (right) Predicted Surface Temperatures

data to analyze the heat islands that are manifested through an elevation in the surface thermal emission of urban regions. Therefore, the main research hypotheses for this study were:

1. A temporal evaluation of the MSE of surface air will provide a more appropriate indicator of the UHI presence over time than surface air measurements.
2. The spatial pattern of the remotely-sensed, surface temperature-derived SHI will be similar to the surface air temperature-derived UHI.
3. The spatial resolution of the remotely-sensed, surface temperature-derived SHI will reveal microscale differences that the surface air temperature-derived UHI is unable to depict.
4. Altering amounts of vegetation within a given land cover over time will reveal changes in surface temperature values, thus providing a means to reconstruct and predict future SHIs.

Upon completion of this research endeavor, an evaluation of each research hypothesis is as follows:

1. A decreasing temporal trend in MSE was identified throughout the study period whereas no significant linear trend occurred in air temperature. Therefore, given that the study area was indeed undergoing land conversion, MSE appears to be a better indicator of the UHI over time, thus confirming the research hypothesis. This is supported by the change detection rates generated from a comparison of the 1988 and 2003 LANDSAT data sets, as well as the range in 1988 and 2003 predicted surface temperatures (as a function of land cover).
2. The spatial resolution of the 1998 air temperature-derived UHI compared to the 1998 remotely-sensed, surface temperature-derived SHI was so poor that the spatial pattern

between the two datasets was unrecognizable. Therefore, the second hypothesis was not confirmed. This is further supported in the analysis of the temperature range of each data set. The surface air temperature-derived SHI showed a temperature range of 57 C^{o}, whereas the air temperature-derived UHI only depicted a temperature range of 2 C^{o}.

3. The surface air temperature-derived UHI did not portray an accurate representation of distinct changes in surface temperature across the study area. When compared to the 10-meter spatial resolution of the remotely-sensed thermal data set, a meteorological network of 4 stations reporting maximum temperature throughout the study area simply could not provide the means to accurately assess the UHI at the micro-scale level. Therefore, the third hypothesis was confirmed.
4. Finally, this study validated the hypothesis that altering amounts of vegetation within a given land cover over time will reveal changes in surface temperature values, thus providing a means to reconstruct and predict future SHIs. However, the land cover classification process revealed some anomalous findings that must be investigated further.

5.6 SUGGESTED FUTURE RESEARCH

Although the ASOS temperature did not indicate a trend over time, it is possible that a single station is not indicative of air temperatures throughout an entire study area. Therefore, MSE and air temperature correlations for numerous locations throughout the study area should be performed in order to better validate the MSE parameter. Furthermore, in order to test the spatial pattern of the remotely-sensed, surface temperature-derived SHI against that of a known

meteorological network more accurately, there must be a greater population of surface air temperature recording stations within such network.

Finally, the relationship between altering land cover and its associated impact on UHI creation needs to be further explored. This study did not evaluate the effects of the changing UHI due to the inter-relationships of land cover conversion. For example, what are the effects of a parcel of land being converted from vegetation-forest to urban as compared to being converted from vegetation-forest to bare land? Furthermore, this study did not evaluate the effects of urban forest regeneration. Future studies could easily quantify the effects on surface temperature from land conversions such as urban parcels being reforested, thus helping to mitigate the UHI.

CHAPTER 6. CASE STUDY: EVALUATING THE THERMAL EFFICIENCY OF URBANIZATION IN BATON ROUGE, LOUISIANA

6.1 OVERVIEW

As the natural land cover of an urban area is converted to various land cover types, the measure of additional longwave radiant energy that is emitted from the surface is an indicator of the thermal efficiency of the new land cover. Holding regional meteorological conditions constant, every excess watt of energy emitted from an urban land cover type contributes to the formation of a SHI. Therefore, the SHI effect can be defined more accurately as the excess quantity of heat (in W m^{-2}) emitted relative to adjacent rural regions (Stone and Rodgers 2001). Given that the natural land cover of the Baton Rouge urban area was originally comprised of forest, determining the radiant flux density of the current land cover and subtracting from that quantity the radiant flux density estimated to be generated by a forest of equal size will yield the net thermal effect of the current land cover.

6.2 DATA AND METHODS

Calculating the net thermal efficiency of urban land cover types first requires that the average radiant flux density (W m^{-2}) be determined for each land cover polygon. Average radiant flux density values (channel four of the 1998 ATLAS energy data set) are computed for each representative land cover polygons previously used in Ch 4. These values are assigned to each land cover polygon generated from the 1988 and 2003 LANDSAT classification. The forest radiant flux density for the study area is determined using an average of radiant flux density values at Burden Research Center, an area of approximately 81 hectares (200 acres) of natural forest in the middle of the study area dating back to the turn of the 20th century. The

radiant flux density at Burden is then extrapolated to the total area of the land cover polygons (m^2) to produce the estimated natural land cover radiant flux (W) of each land cover polygon prior to land cover conversion (urbanization).

Total radiant flux energy (W) for each land cover polygon is calculated by multiplying land cover area (m^2) by its corresponding radiant flux density ($W\ m^{-2}$). The net thermal efficiency of each land cover type, for both the 1988 and 2003 LANDSAT data sets, is determined by subtracting the natural land cover radiant flux (W) from its total radiant flux energy (W). The resulting measure of net thermal emissions estimates the contribution of individual land cover to the Baton Rouge SHI.

6.3 RESULTS AND DISCUSSION

From Chapter 4, land cover types within the ATLAS 1998 data set are represented as individual area of interest (AOI) layers. The boundary of each AOI is used to spatially subset channel four of the 1998 ATLAS energy data set (radiant flux density) into five separate images, one representing each land cover type. The 1998 average radiant flux density for each land cover, as well as the 1988 and 2003 area calculations for each land cover (m2), is noted in Table 6.1.

Table 6.1: ATLAS Average Radiant Flux Density and LANDSAT Area Calculations

Land Cover	1998 ($W\ m^{-2}$)	1988 (m^2)	2003 (m^2)
Urban	269.86	66,978,128.53	43,929,824.33
Water	382.542	90,057,512.58	68,274,935.58
Bare Land	246.477	257,016,693.13	306,372,283.56
Vegetation -Non-forest	288.641	572,913,139.97	386,392,556.22
Vegetation-Forest	329.212	83,750,209.28	665,748,673.8

From the 1998 ATLAS data set, a polygon representing the Burden Research Center is created through onscreen digitizing. Through image statistics, the average radiant flux density value for the Burden polygon is determined from channel four of the ATLAS energy data set. This value (323.678 W m^{-2}) is multiplied by the 1988 and 2003 land cover areas. This yields the estimated natural land cover radiant flux energy (W) of each land cover polygon. The results are depicted in Table 6.2.

Table 6.2: 1988 and 2003 Natural Land Cover Radiant Flux Energy

Land Cover	1988 Natural Land Cover (W)	2003 Natural Land Cover (W)
Urban	21679346686.33	14219117679.49
Water	29149635556.87	22099094598.66
Bare Land	83190649198.93	99165967998.13
Veg-Non-forest	185439379319.21	125066769812.18
Veg-Forest	27108100239.33	215488199238.24

Total radiant flux energy (W) for each land cover type within the 1988 and 2003 LANDSAT data set is calculated by multiplying land cover area (m^2) by its corresponding radiant flux density (W m^{-2}). The results are shown in Table 6.3.

Table 6.3: 1988 and 2003 Land Cover Radiant Flux Energy

Land Cover	1988 (W)	2003 (W)
Urban	18074717765	11854902394
Water	34450780977	26118030407
Bare Land	63348703473	75513721335
Veg-Non-forest	1.65366E+11	111528733820
Veg-Forest	27571573897	21917245240

The net thermal efficiency of each land cover type, for both the 1988 and 2003 LANDSAT data sets, is determined by subtracting the natural land cover radiant flux energy (Table 6.2) from its total radiant flux energy (Table 6.3). The resulting measure of net thermal emissions estimates the contribution of individual land cover to the Baton Rouge SHI. The results are shown in Table 6.4.

Table 6.4: 1988 and 2003 Net Thermal Emissions

Land Cover	1988 Net Thermal Emissions	2003 Net Thermal Emissions
Urban	-3604628921.23	-2364215285.79
Water	5301145420.51	4018935807.98
Bare Land	-19841945726.33	-23652246663.12
Veg-Non-forest	-20073157685.13	-13538035992.28
Veg-Forest	463473658.16	3684253160.81

To conclude, "…thermal efficiency accounts for both the rate of radiant emissions per unit of area and the total area across which this radiant energy is being emitted" (Stone and Rodgers 2001). However, when spatially applying radiant flux density values of one data set to another, it is imperative that both data sets are of high spatial accuracy. The ATLAS four-band mosaic energy file, of which channel four represents radiant flux density values, is geometrically distorted throughout the study area. Because the LANDSAT 1988 and 2003 land cover AOIs were applied to the 1998 ATLAS mosaic energy file, it is believed that radiant flux density values for each land cover were not accurately portrayed, thus resulting in inaccurate predicted radiant flux energy values and prohibiting accurate net thermal emission calculations. To date, other studies (Luvall *et*. al 2005) using the 1998 ATLAS data set for Baton Rouge partitioned land surfaces based upon land use categories (industrial, central business district, residential, and park). Therefore, no true comparison of radiant flux density values from this research endeavor can currently be made to an existing study.

CHAPTER 7. CASE STUDY: THE IMPACT OF TREE GROWTH ON SURFACE TEMPERATURE IN BATON ROUGE, LOUISIANA

7.1 OVERVIEW

The procedures discussed in Chapter 3 allows for a multitude of "spin off" studies that can address some important issues related to future development and mitigation of the UHI problem in an already hot-summer climate. For instance, what is the potential impact of preservation of forested areas in terms of mitigating the UHI impact, as the trees grow over time? While the entire study area provides an adequate sampling of trees within various stages of their life cycle, two areas in particular provide a representation of hardwoods spanning various periods of tree growth during the past century: 1) the Burden Research Center, with trees dating back to the turn of the 20th century, and 2) oaks planted during the 1940s on the LSU campus. The two locations analyzed in the study area represent hardwood stands in two distinct life cycle stages.

An analysis of increased tree canopy over this time period provides an evaluation of the effect of increased vegetation on surface temperature. Therefore, the contribution of increasing vegetation to decreasing the local SHI is evaluated, thus quantifying the contribution of increasing tree canopy in the future to mitigate the SHI.

7.2 DATA AND METHODS

From the 1998 ATLAS data set, polygons representing each area noted above are created through onscreen digitizing. The corresponding average surface temperature and average NDVI for each location (polygon) is computed and used to derive a regression equation based upon the 1998 ATLAS data set. The same locations are extracted from the 1988 and 2003 LANDSAT data sets and average NDVIs for each 1988 and 2003 location are computed. Utilizing the 1998

regression equation, the average surface temperature for the 1988 and 2003 locations are estimated. A comparison of surface temperatures for each location from 1988 to 2003 indicates the net change in tree canopy and the contribution of tree growth to mitigating the SHI is quantified, with respect to the age of the hardwood stand.

7.3 RESULTS AND DISCUSSION

Within the 1998 ATLAS data set, area of interest (AOI) polygons representing the Burden Research Center and the oaks within the LSU campus are created. Each AOI is used as a boundary to crop the ATLAS and LANDSAT NDVI data sets. Surface temperature and NDVI values from the ATLAS data set and NDVI values from the 1988 and 2003 LANDSAT data set are extracted for each cropped image. Figures 7.1 through 7.3 represent the extracted AOI polygons for the Burden Research Center and Figures 7.4 through 7.6 represent the extracted AOI polygons for the oaks within the LSU campus. Image statistics are calculated for all polygons and results are noted in Table 7.1. From the 1988 ATLAS polygon values for surface temperature and NDVI, the following regression equation is applied to the 1988 and 2003 LANDSAT NDVI polygon values to predict corresponding surface temperatures (Table 7.2):

$$y = -34.5146(x) + 45.44064$$

where y = surface temperature (ºC)

and x = NDVI

Table 7.1: Image Statistics for the AOIs (Averages)

Location	ATLAS Temp	ATLAS NDVI	1988 NDVI	2003 NDVI
Burden Research Center	33.26 ºC	0.353	0.331	0.594
LSU Oaks	43.92 ºC	0.044	-0.030	0.316

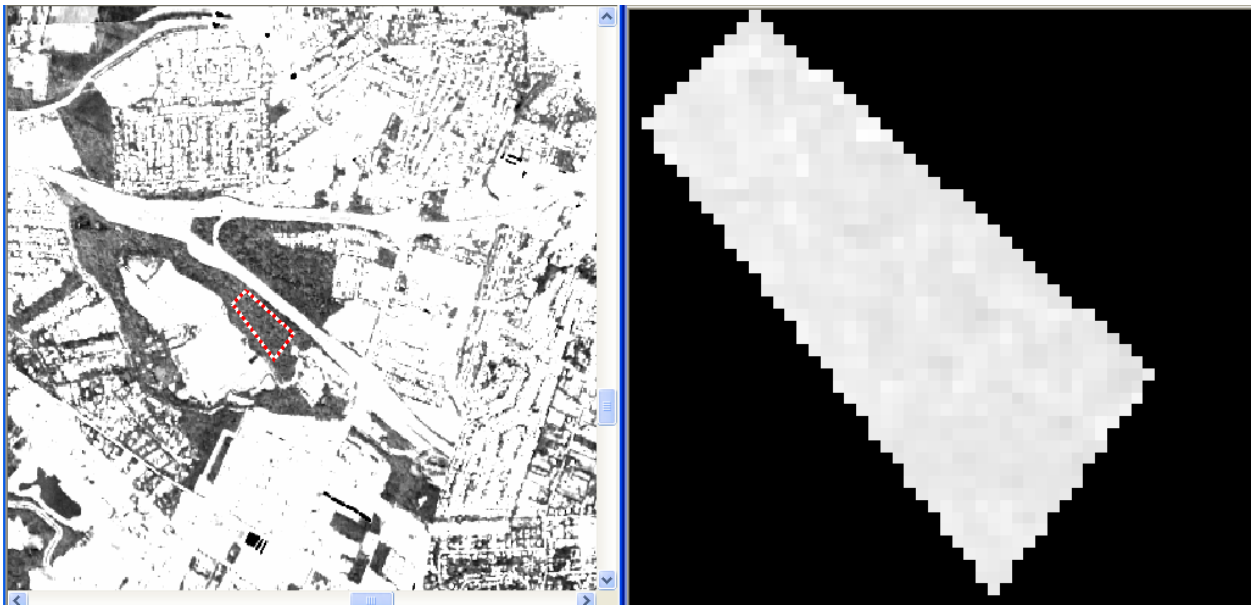

Figure 7.1: 1998 ATLAS Data for the Burden Research Center

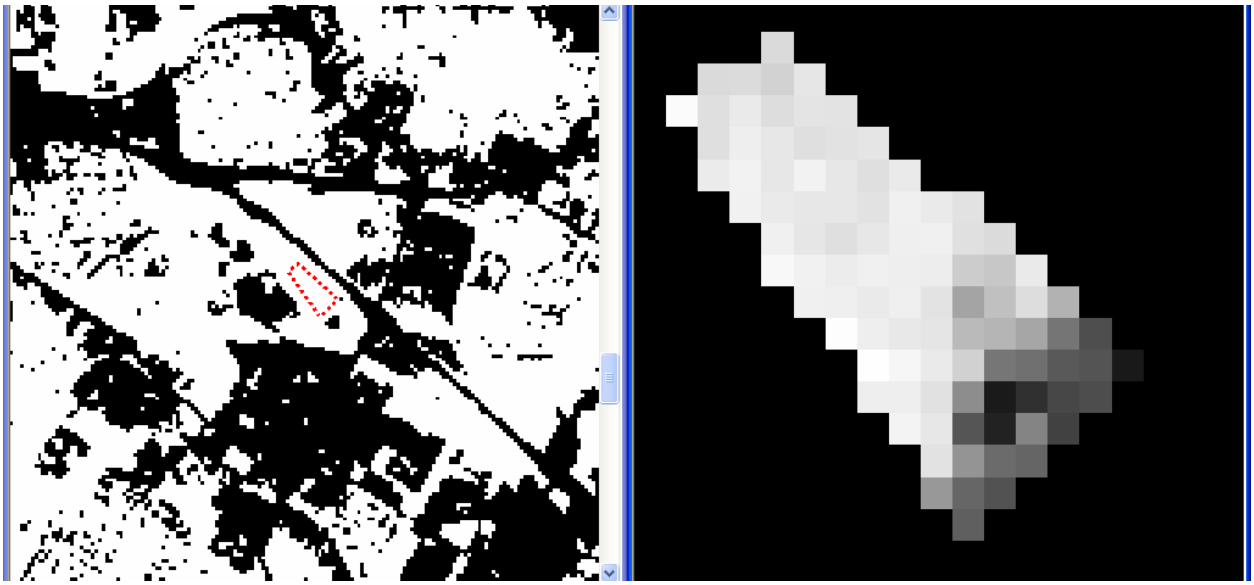

Figure 7.2: 1988 NDVI Data for the Burden Research Center

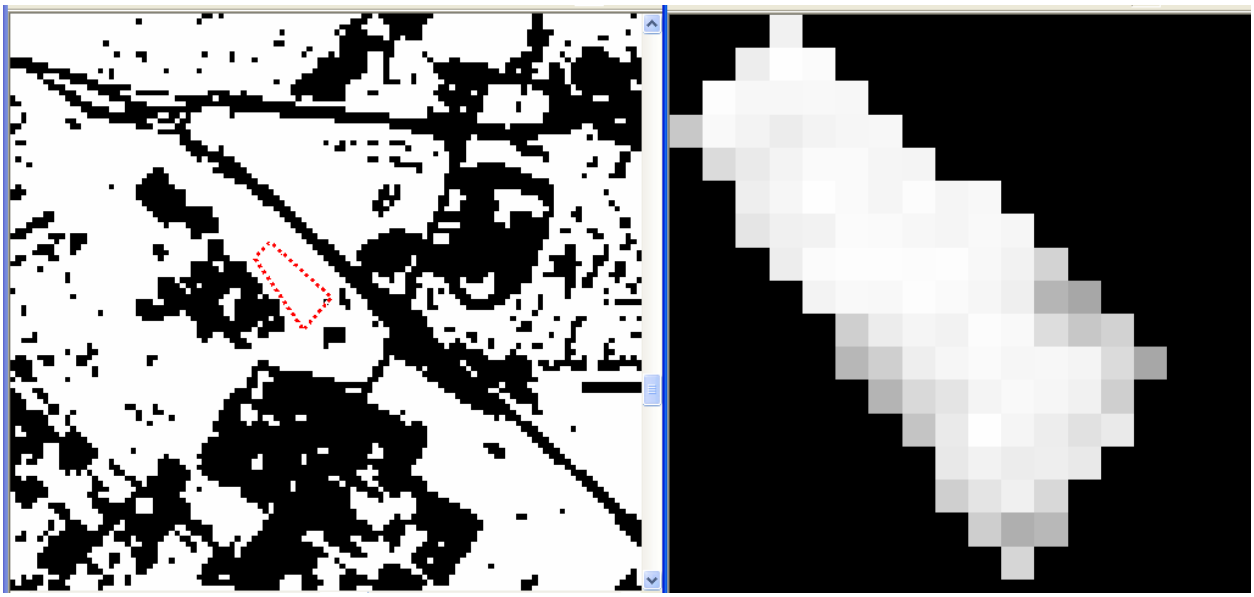

Figure 7.3: 2003 NDVI Data for the Burden Research Center

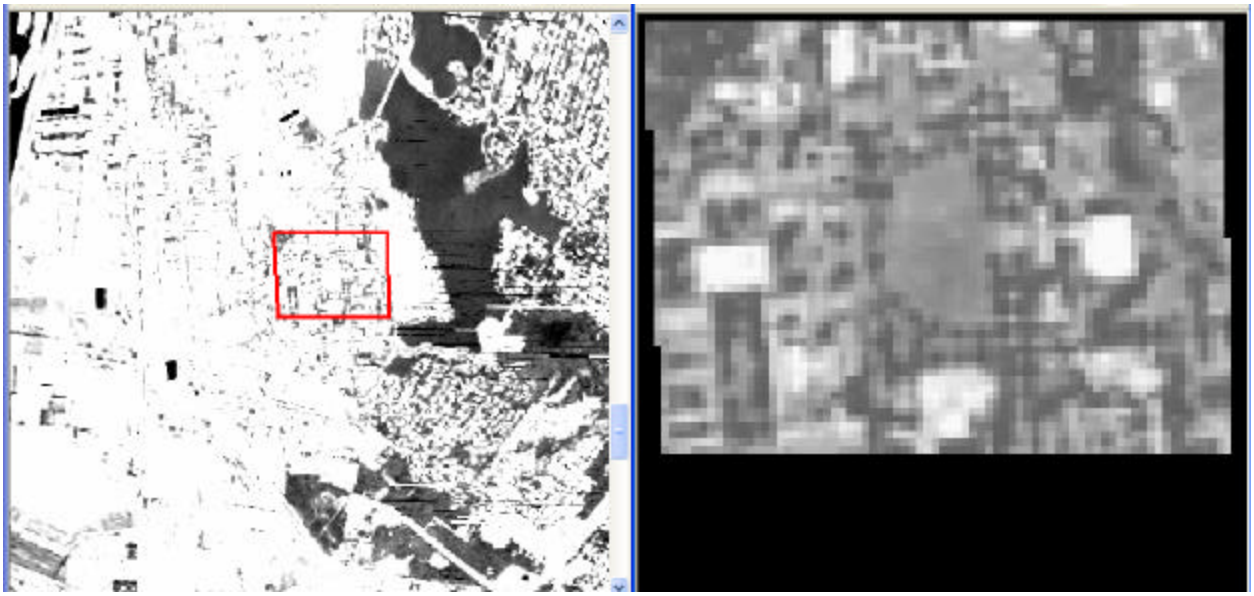

Figure 7.4: 1998 ATLAS Data for the Oaks within the LSU Campus

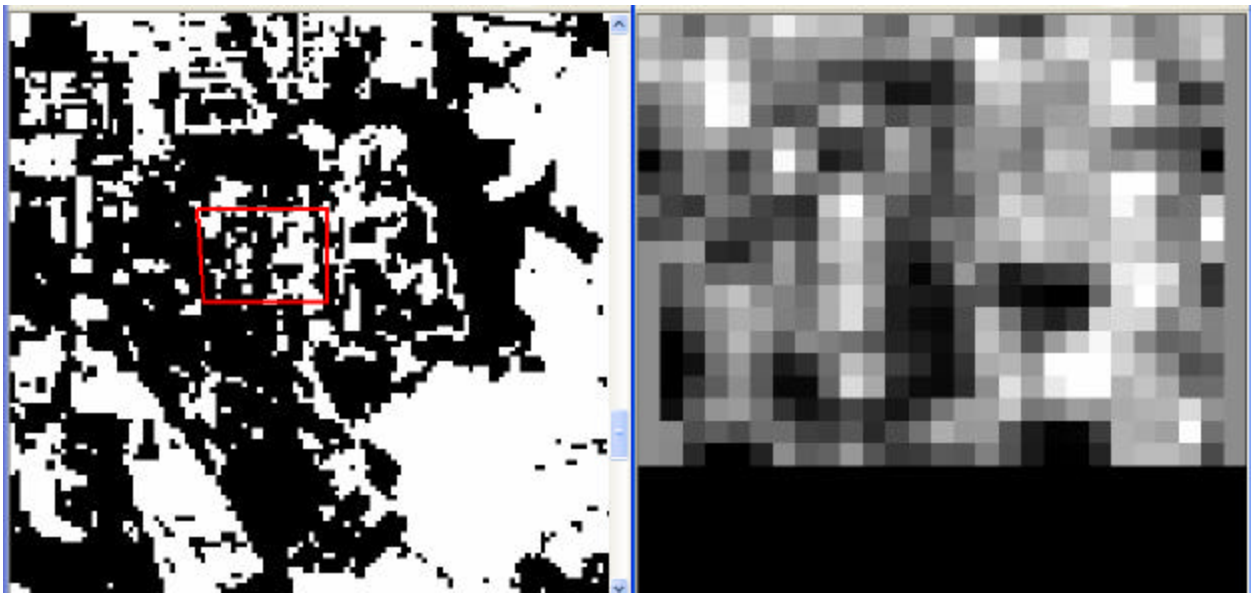

Figure 7.5: 1988 NDVI Data for the Oaks within the LSU Campus

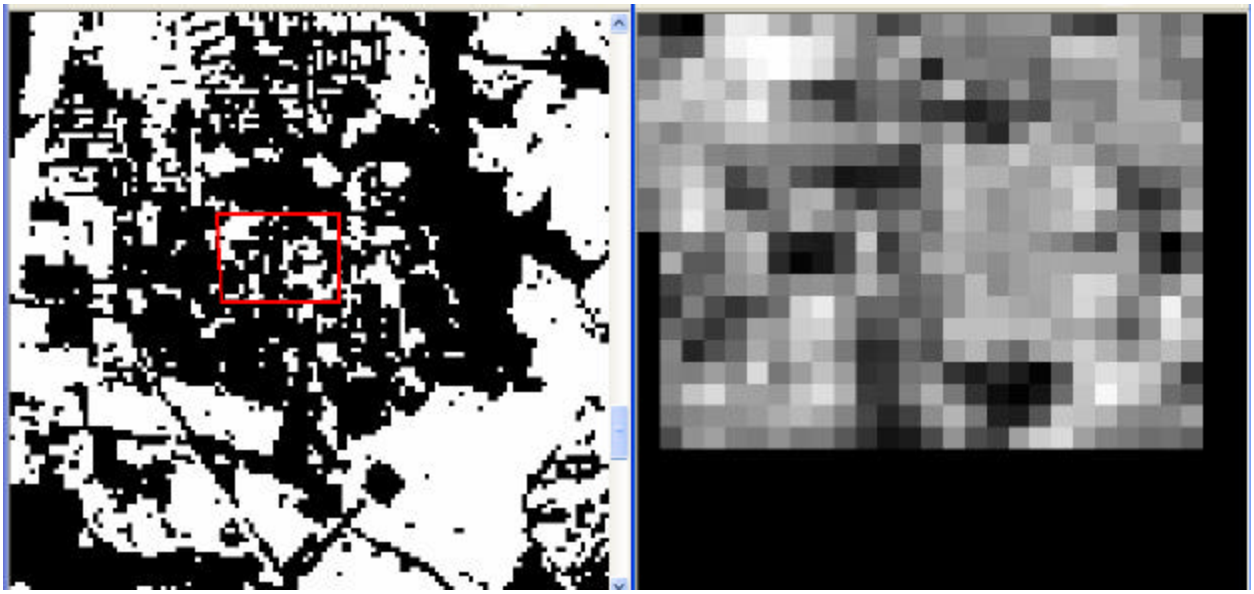

Figure 7.6: 2003 NDVI Data for the Oaks within the LSU Campus

Table 7.2: Surface Temperature Comparisons for the AOIs

Location	Burden Research Center	LSU Oaks
1988 Predicted LANDSAT Temp	34.01 ºC	46.48 ºC
1998 ATLAS Temp	33.26 ºC	43.92 ºC
2003 Predicted LANDSAT Temp	24.94 ºC	34.53 ºC

A comparison of surface temperature for each location from 1988 to 2003 indicates the net change in tree canopy (increased NDVI values) can decrease surface temperature, thus providing means to mitigate the SHI. At the Burden Research Center from 1988 – 1998, there was a net decrease of surface temperature of 0.75 Cº and a decrease of 8.32 Cº from 1998 – 2003. Within the LSU campus from 1988 – 1988, there was a net decrease of surface temperature of 2.56 Cº and a decrease of 9.39 Cº from 1998 – 2003. Further research is needed to quantify the greater increase in tree canopy at both locations over the last 5 years of this study period, as compared to the previous decade. With respect to the age of the hardwood stand (over a 40 year span throughout the study period), no comparison can be made regarding to the age of the tree stand and its ability to mitigate the SHI. The younger trees within the LSU campus did in fact show a greater net decrease in surface temperature within both time periods. However, a longer study period (greater than 15 years) is needed to support any conclusion. However, because both locations have shown an increase in vegetation, this research supports both urban forest regeneration and forest preservation efforts. Regardless of whether new trees are introduced, or existing trees are allowed to remain, as their tree canopy increases over time they will have a positive impact on the ability to mitigate the SHI.

REFERENCES

Anderson, S.E., 1992: Determination of water surface temperature based on the use of thermal infrared multispectral scanner data. *Geocarto International* 3, 3-8.

Aniello, C., K. Morgan, A. Busbey, and L. Newland, 1995: Mapping micro-urban heat islands using Landsat TM and a GIS. *Computers and Geosciences* 21(8), 965-967.

Arnfield, A.J., 1998: Micro-and mesoclimatology. *Progress in Physical Geography* 22(1), 103-113.

_____, 2003: Two decades of urban climate research: A review of turbulence, exchanges of energy and water, and the urban heat island. *International Journal of Climatology* 23(1), 1-26.

Asaeda, T. and V.T. Ca, 1993: The subsurface transport of heat and moisture and its effect on the environment: a numerical model. *Boundary Layer Meteorology* 65, 159-179.

_____, and A.Wake, 1996: Heat storage of pavement and its effect on the lower atmosphere. *Atmospheric Environment* 30(3), 413-427.

Atkinson, B.W., 2003: Numerical modelling of urban heat-island intensity. *Boundary-Layer Meteorology* 109(3), 285-310.

Avissar, R., 1996: Potential effects of vegetation on the urban thermal environment. *Atmospheric Environment* 30(3), 437-448.

Ball, J.R., 2003: The cost of green. *Business Report* Sept.16, 2003.

Balling, R.C., and S.W. Brazel, 1988: High-resolution surface temperature patterns in a complex urban terrain. *Photogrammetric Engineering and Remote Sensing* 54(9), 1289-1293.

_____, 1992: *The Heated Debate.* Pacific Research Institute for Public Policy, San Fransisco, CA, p57-59.

Belaid, M.A., 2003: Urban-rural land use change detection and analysis using GIS and technologies. *2nd FIG Regional Conference,* Marrakech, Morocco, December 2-5.

BenDor, E. and H. Saaroni, 1997: Airborne video thermal radiometry as a tool for monitoring microscale structures of the urban heat island. *International Journal of Remote Sensing* 18(14), 3039-3053.

Berk, A., G.P. Anderson, P.K. Acharya, J.H. Chetwynd, L.S. Bernstein, E.P. Shettle, M.W. Matthew, and S.M. Adler-Golde, 1999: *MODTRAN4 Users Manual.* Air Force Research Laboratory, Space Vehicles Directorate, Air Force Material Command, Anscom Air Force Base, Ma 01731-3010.

Beverley, A.M. and P.G. Penton, 1989: *ELAS , Earth Resources Laboratory Applications Software User Reference*. Earth Resource Lab, NSTL, Mississippi, Report No 183, Vol 2.

Blankenstein, S. and W. Kuttler, 2004: Impact of street geometry on downward longwave radiation and air temperature in an urban environment. *Meteorologische Zeitschrift* 13(5), 373-379.

Borghi, S., G. Corbetta, and L. De Biase, 2000: A heat island model for large urban areas and its application to Milan. *Geophysics and Space Physics* 23(5), 547-566.

Bottyan, Z. and J. Unger, 2003: A multiple linear statistical model for estimating the mean maximum urban heat island. *Theoretical and Applied Climatology* 75(3-4), 233-243.

Brazel, A.J., H.J. Verville, and R. Lougeay, 1993: Spatial-temporal controls on cooling degree hours - an energy demand parameter. *Theoretical and Applied Climatology* 47(2), 81-92.

Brandsma, T., G.P. Können, H.R.A. Wessels, 2003: Emperical estimation of the effect of urban heat advection on the temperature series of De Bilt (The Netherlands). *International Journal of Climatology* 23(7), 829-845.

Brovkin, V., 2002: Climate-vegetation interaction. *Journal de Physique IV* 12(10), 57-72.

Ca, V.T., T. Asaeda, and E.M. Abu, 1998: Reductions in air conditioning energy caused by a nearby park. *Energy and Buildings* 29(1), 83-92.

_____, and Y. Ashie, 1999: Development of a numerical model for the evaluation of the urban thermal environment. *Journal of Wind Engineering and Industrial Aerodynamics* 81, 181-196.

Carlson, T.N., J.A. Augustine, and F.E. Boland, 1977: Potential application of satellite temperature measurements in the analysis of land use over urban areas. *Bulletin of the American Meteorological Society* 58(12), 1301-1303.

_____, J.K. Dodd, S.G. Benjamin, and J.N. Cooper, 1981: Satellite estimation of the surface-energy balance, moisture availability and thermal inertia. *Journal of Applied Meteorology* 20(1), 67-87.

Chandler, T.J., 1968: Urban climates. *Proceedings of the Symposium on Urban Climates and Building Climatology, Brussels, October 1968*, World Meteorological Organization, Technical Note 1(108).

_____, 1976: *Urban Climatology and its Relevance to Urban Design*. World Meteorological Organization, Publication 438, Technical Note 149, 61pp.

Changnon, S.A., K.E. Kunkel, and B.C. Reinke, 1996: Impacts and responses to the 1995 heat wave: A call to action. *Bulletin of the American Meteorological Society* 77(7), 1497-1506.

Chen, L., W. Zhu, X. Zhou, and Z. Zhou, 2003: Characteristics of the heat island effect in Shanghai and its possible mechanism. *Advances in Atmospheric Sciences* 20(6), 991-1001.

Choi, Youngeun, 1998: *Urban Effects on Precipitation in the Southern United States of America*. Ph.D. Dissertation, Louisiana State University, 148pp.

Chow, S.D., 1992: The urban climate of Shanghai. *Atmospheric Environment*, Part B-Urban Atmosphere, 26(1), 9-15.

Chudnovsky, A., E. Ben-Dor, and H. Saaroni, 2004: Diurnal thermal behavior of selected urban objects using remote sensing measurements. *Energy and Buildins* 36(11), 1063-1074.

Chung, U., J. Choi, and J.I. Yun, 2004: Urbanization effect on the observed change in mean monthly temperatures between 1951-1980 and 1971-2000 in Korea. *Climatic Change* 66(1-2), 127-136.

Clarke, J.F. and J.T. Peterson, 1972: The effect of regional climate and land use on the nocturnal heat island. *Conference on Urban Environment and Second Conference on Biometeorology*, American Meteorological Society, Philadelphia, 147-52.

Comrie, A., 2000: Mapping a wind-modified urban heat island in Tucson, Arizona. *Bulletin of the American Meteorological Society* 81(10), 2417-2431.

Condella, V., 1998: Climate islands. *Earth* 7(1), 54-56.

Dixon, P.G. and T. Mote, 2003: Patterns and causes of Atlanta's urban heat island–initiated precipitation. *Journal of Applied Meteorology*. 42(9), 1273–1284.

Dousset B. and F. Gourmelon, 2003: Satellite multi-sensor data analysis of urban surface temperatures and landcover. ISPRS Journal of Photogrammetry and Remote Sensing 58(1-2), 43-54.

Ducksworth, F.S. and J.S. Sandberg, 1954: The effect of cities upon horizontal and vertical temperature gradients. *Bulletin of the American Meteorological Society* 35, 198-207.

Fan, H.L. and D.J. Sailor, 2005: Modeling the impacts of anthropogenic heating on the urban climate of Philadelphia: a comparison of implementation in two PBL schemes. *Atmospheric Environment* 39(1), 73-84.

Federation for American Immigration Reform, 2004: Metro Area Factsheet: Baton Rouge, Louisiana MSA. http://www.fairus.org/Research/Research.cfm?ID=795&c=9.

Fedotov, A.Y., 1991: Anthropogenic aerosols and its role in formation of the urban heat-island. *Academy of Sciences, USSR, Atmospheric and Oceanic Physics.* 27(8), 842-846.

Ford, K., 1979: *Remote Sensing for Planners.* Center for Urban Policy Research. New Brunswick, NJ, 219pp.

Friedl, M.A. and F.W. Davis, 1994: Sources of variation in radiometric surface-temperature over a tallgrass prairie. *Remote Sensing of Environment* 48(1), 1-17.

Fujibe, F., 2003: Long-term surface wind changes in the Tokyo metropolitan area in the afternoon of sunny days in the warm season. *Journal of the Meteorological Society of Japan* 81(1), 141-149.

Gallo, K.P., A.L. Mcnab, T.R. Karl, J.F. Brown, J.J. Hood, and J.D. Tarpley, 1993: The use of a vegetation index for assessment of the urban heat-island effect. *International Journal of Remote Sensing* 14(11), 2223-2230.

_____, and J.D. Tarpley, 1996: The comparison of vegetation index and surface temperature composites for urban heat-island analysis. *International Journal of Remote Sensing* 17(15), 3071-3076.

_____ and T.W. Owen, 1999: Satellite-based adjustments for the urban heat island temperature bias. *Journal of Applied Meteorology* 38(6), 806-813.

_____, J.O. Adegoke, T.W. Owen, and C.D. Elvidge, 2002: Satellite-based detection of global urban heat-island temperature influence. *Journal of Geophysical Research-Atmospheres* 107(D24), 4776.

Goward, S.N., 1981: Thermal behavior of urban landscapes and the urban heat island. *Physical Geography* 2(1), 19-33.

Graham, M.H., B.G. Junkin, N.T. Kalcic, R.W. Pearson, and B.R. Seyfarth, 1986: *ELAS-Earth Resources Laboratory Applications Software*. NASA/NSTL/ERL Report 183.

Grimmond, C.S.B., C. Souch, and M.D. Hubble, 1996: Influence of tree cover on summertime surface energy balance fluxes, San Gabriel Valley, Los Angeles. *Climate Research* 6(1), 45-57.

Giridharan, R., 2004: Daytime urban heat island effect in high-rise and high-density residential developments in Hong Kong. *Energy and Buildings* 36(6), 525-534.

Grosskopf, K.R., 2003: Investing in "green" building alternatives: U.S. consumer willingness-to-pay. *The Future of Sustainable Construction*. International e-Journal of Construction, http://www.bcn.ufl.edu/iejc/pindex/107/grosskopf.pdf, 8pp.

Hafner, J. and S.Q. Kidder, 1999: Urban heat island modeling in conjunction with satellite-derived surface/soil parameters. *Journal of Applied Meteorology* 38(4), 448-465.

Haltiner, G.J., and R.T. Williams, 1980: *Numerical Prediction and Dynamic Meteorology, 2nd Edition*. John Wiley and Sons, New York, 477pp.

Hawkins, T.W., W.L. Stefanov, W. Bigler, and E.M. Saffell, 2004: The role of rural variability in urban heat island determination for Phoenix, Arizona. *Journal of Applied Meteorology* 43(3), 476-486.

Heilman, J.L. and R.W. Gesch, 1991: Effects of turfgrass evaporation on external temperatures of buildings. *Theoretical and Applied Climatology* 43(4), 185-194.

Hinkel, K.M., F.E. Nelson, A.F. Klene, and J.H. Bell, 2003: The urban heat island in winter at Barrow, Alaska. *International Journal of Climatology* 23(15), 1889-1905.

Hinkle, D.E., W. Wiersma, and S.G. Jurs, 1994: *Applied Statistics for the Behavioral Sciences*. Houghton Mifflin Company, Princeton, NJ, 712pp.

Hirano, Y., Y. Yasuoka, and T. Ichinose, 2004: Urban climate simulation by incorporating satellite-derived vegetation cover distribution into a mesoscale meteorological model. *Theoretical and Applied Climatology* 79, 175-184.

Hogan, A.W. and M.G. Ferrick, 1998: Observations in nonurban heat islands. *Journal of Applied Meteorology* 37(2), 232-236.

Hsu, S.A., 1988: *Coastal Meteorology*. Academic Press, San Diego, CA, 260pp.

Hudson, J.L., 1996: Global warming skeptic. *Weatherwise* 49(7).

Hwang, F-K, 2004: Department of Physics, National Taiwan Normal University. http://www.phy.ntnu.edu.tw/java/emWave/emWave.html

Jager, J., 1993: *Climate and Energy Systems: A Review of their Interactions.* John Wiley and Sons, New York, 231pp.

Jauregui, E., 1997: Heat island development in Mexico City. *Atmospheric Environment* 31(22), 3821-3831.

Jensen, J., 1996: *Introductory Digital Image Processing, A Remote Sensing Perspective* Prentice Hall, Upper Saddle River, NJ, 316pp.

Johnson, G.L., J.M. Davis, T.R. Karl, A.L McNab, K.P. Gallo, J.D. Tarpley, P. Bloomfield. Estimating urban temperature bias using polar-orbiting satellite data. *Journal of Applied Meteorology* 33(3), 358-369.

Jones, P. D., S. C. B. Raper, C. M. Goodess, B. S. G. Cherry and T. M. L. Wigley, 1986: *A gridpoint surface air temperature data set for the southern hemisphere.* U.S. Dept. of Energy, Carbon Dioxide Research Division, Washington, DC, Technical report, TR027, 73pp.

_____, P.M. Kelly and C.M. Goodess, 1989: The effect of urban warming on the Northern Hemisphere temperature average. *Journal of Climate* 2(3), 285-290.

_____, P.Y. Groisman, M. Coughlan, N. Plummer, W.C. Wangl, and T.R. Karl, 1990: Assessment of urbanization effects in time series of surface air temperatures over land. *Nature* 347(6289), 169-172.

Kalnay, E. and M. Cai, 2003: Impact of urbanization and land-use change on climate. *Nature* 423(6939), 528-531.

Karl, T.R., Diaz, H.F., and G. Kukla, 1988: Urbanization: Its detection and effect in the United States climate record. *Journal of Climate* 1, 1099-1123.

Khan, S.M. and R.W. Simpson, 2001: Effect of a heat island on the meteorology of a complex urban airshed. *Boundary-Layer Meteorology* 100(3), 487-506.

Kim, H.H., 1992: Urban Heat Island. *International Journal of Remote Sensing* 13(12), 2319- 2336.

Kloer, B.R., 1994: *Hybrid Parametric/Non-parametric Image Classification*. Paper presented at the ACSM-ASPRS Annual Convention, April 1994, Reno Nevada.

Kukla, G., J. Gavin and T.R. Karl, 1986: Urban Warming. *Journal of Climate and Applied Meteorology* 25(9), 1265-1270.

Lam, N., 1983: Spatial Interpolation Methods: A Review. *The American Cartographer* 10(2), 129-149.

Landsberg, H.E. and T.N. Maisel, 1972: Micrometeorological observations in an area of urban growth. *Boundary Layer Meteorology* 2, 365-70.

_____, 1976: *Weather, Climate and Human Settlements.* World Meteorological Organization, Publication 448, Special Environmental Report 7, 45pp.

Laverne, R.J. and G.M. Lewis, 2000: Trees and building energy use. *Global Climate Change and The Urban Forest.* Franklin Press, Inc., Baton Rouge, LA, 58-69.

Lemonsu, A. and V. Masson, 2002: Simulation of a summer urban breeze over Paris. *Boundary-Layer Meteorology* 104(3), 463-490.

Lo, C.P. and D.A. Quattrochi, 2003: Land-use and land-cover change, urban heat island phenomenon, and health implications: A remote sensing approach. *Photogrammetric Engineering and Remote Sensing* 69(9), 1053-1063.

_____, and J.C. Luvall, 1997: Application of high-resolution thermal infrared remote sensing and GIS to assess the urban heat island effect. *International Journal of Remote Sensing* 18(2), 287-304.

Louisiana Oil Spill Coordinators Office (LOSCO), 1999: Parish Boundaries of Louisiana from LDOTD source data, Geographic NAD83, LOSCO (2000) [pshgeog3dpdot].

Louisiana Oil Spill Coordinator's Office (LOSCO) and United States Geological Survey (USGS), 2000: Color Infrared Orthophotography of Louisiana, LOSCO, USGS.

Luvall, J.C., D. Quattrochi, D. Rickman, and M. Estes, 2005: *Urban Heat Island Pilot Project*, EPA/NASA.

Magee, N., J. Curtis, and G. Wendler, 1999: The urban heat island effect at Fairbanks, Alaska. *Theoretical and Applied Climatology* 64(1-2), 39-47.

McKellip, R., 1998: *Post-Mission Flight Report, ATLAS Mission M9811*, Lockheed Martin Stennis Operations, NASA/MSFC/GCHC.

McPherson, G.E., 2000: Urban Forests and Climate Change. *Global Climate Change and the Urban Forest.* Franklin Press, Inc., Baton Rouge, LA, 58-69.

Mihalakakou, G., M. Santamouris, N. Papanikolaou, C. Cartalis, and A. Tsangrassoulis, 2004: Simulation of the urban heat island phenomenon in Mediterranean climates. *Pure and Applied Geophysics* 161(2), 429-451.

Moll, G., 1997: America's Urban Forests: Growing Concerns. *American Forests* 103(3), 15-18.

Narisma, G.T. and A.J. Pitman, 2003: The impact of 200 years of land cover change on the Australian near-surface climate. *Journal of Hydrometeorology* 4(2), 424-436.

Nichol, J.E., 1994: A GIS-based approach to microclimate monitoring in Singapore's high-rise housing estates. *Photogrammetric Engineering and Remote Sensing* 60(10), 1225-1232.

_____, 1996: High-Resolution surface temperature patterns related to urban morphology in a tropical city: a satellite-based study. *Journal of Applied Meteorology* 35(1), 135-146.

National Oceanic Atmospheric Administration (NOAA), 2004: http//nndc/noaa.gov

Noto, K., 1996: Dependence of heat island phenomena on stable stratification and heat quantity in a calm environment. *Atmospheric Environment* 30(3), 475-485.

Oke, T.R. and R.F. Fuggle, 1972: Comparison of urban/rural counter and net radiation at night. *Boundary Layer Meteorology* 2, 290-307.

_____, 1973: City size and the urban heat island. *Atmospheric Environment* 7(8), 769-779.

_____, 1976: The distinction between canopy and boundary-level heat islands. *Atmosphere* 14, 268-277.

_____, 1979: *Review of Urban Climatology, 1973-1976*. World Meteorological Organization, Publication 539, Technical Note 169, 100pp.

_____, 1982: The energetic basis of the urban heat-island. *Quarterly Journal of the Royal Meteorological Society* 108(455), 1-24.

_____, A. Spronken-Smith, E. Jauregui, and C.S.B. Grimmond, 1999: The energy balance of central Mexico City during the dry season. *Atmospheric Envirionment* 33(24-25), 3919-3930.

Owen T.W, T.N. Carlson, and R.R. Gillies, 1998: An assessment of satellite remotely-sensed land cover parameters in quantitatively describing the climatic effect of urbanization. *International Journal of Remote Sensing* 19(9), 1663-1681.

Park, H-S, 1986: Features of the heat island in Seoul and its surrounding cities. *Atmospheric Environment* 20(10), 1859-1866.

Philandras, C.M., D.A. Metaxas, and P.T. Nastos, 1999. Climate variability and urbanization in Athens. *Theoretical and Applied Climatology* 63(1-2), 65-72.

Pielke Sr., R.A. 2003: Heat storage within the earth system. *Bulletin of the American Meteorological Society* 84(3), 331-335.

Pinho, O.S. and M.D.M. Orgaz, 2000: The urban heat island in a small city in coastal Portugal. *International Journal of Biometeorology* 44(4),198-203.

Quattrochi, D.A. and M.K. Ridd, 1998: Analysis of vegetation within a semi-arid urban environment using high spatial resolution airborne thermal infrared remote sensing data. *Atmospheric Environment* 32(1), 19-33.

_____, 1994: Measurement and Analysis of thermal energy responses from discrete urban surfaces using remote sensing data. *International Journal of Remote Sensing* 15(10), 1991-2022.

_____ and J.C. Luvall, 1999: Thermal infrared remote sensing for analysis of landscape ecological processes: methods and applications. *Landscape Ecology* 14(6), 577-598.

Rao, P.S., A.G. Gavane, S.S. Ankam, M.F. Ansari, V.I. Pandit, and P. Nema, 2004: Performance evaluation of a green belt in a petroleum refinery: a case study. *Ecological Engineering* 23(2), 77-84.

Roth, M., T.R. Oke, and W.J. Emery, 1989: Satellite-derived urban heat islands from three coastal cities and the utilization of such data in urban climatology. *International Journal of Remote Sensing* 10(11), 1699-1720.

Rozoff, C.M., W.R. Cotton, and J.O. Adegoke, 2003: Simulation of St. Louis, Missouri, land use impacts on thunderstorms. *Journal of Applied Meteorology* 42(6), 716-738.

Saaroni H., E. Ben-Dor, A. Bitan, and O. Potchter, 2000: Spatial distribution and microscale characteristics of the urban heat island in Tel-Aviv, Israel. *Landscape and Urban Planning* 48(1-2), 1-18.

Sailor, D.J. and H.L Fan, 2002: Modeling the diurnal variability of effective albedo for cities. *Atmospheric Environment* 36(4), 713-725.

Saitoh, T.S., T. Shimada, and H. Hoshi, 1996: Modeling and simulation of the Tokyo urban heat island. *Atmospheric Environment* 30(20), 3431-3442.

Sakakibara, Y., 1996: A numerical study of the effect of urban geometry upon the surface energy budget. *Atmospheric Environment* 30(3), 487-496.

Schlatter, T. and C. Wilson, 1997: Heat islands. Weatherwise 49(46).

Schuman, S.H., C.P. Anderson, and J.T. Oliver, 1964: Epidemiology of successive heat waves in Michigan, 1962 and 1963. *Journal of American Medical Association* 189(10), 733-8.

Shafir, H. and P. Alpert, 1990: On the urban orographic rainfall anomaly in Jerusalem-A numerical study. *Atmospheric Environment, Part B-Urban Temperature* 24(3), 365-375.

Skinner, W.R. and J.A. Majorowicz, 1999: Regional climatic warming and associated twentieth century land-cover changes in north-western North America. *Climate Research* 12(1), 39-52.

Shudo, H., J. Sugiyama, N. Yokoo, and T. Oka, 1997: A study on temperature distribution influenced by various land uses. *Energy and Buildings* 26(2), 199-205.

Southern Regional Climate Center, 2005: http://www.srcc.lsu.edu/southernClimate/atlas/climograph?id=160549, 9/20/2005.

Spronken-Smith, R.A. and T.R. Oke, 1998: The thermal regime of urban parks in two cities with different summer climates. *International Journal of Remote Sensing* 19(11), 2085-2104.

Stallings, J.A., 2004: Characteristics of urban lightning hazards for Atlanta, Georgia. *Climatic Change* 66(1-2), 137-150.

Stone, B.S. and M.O. Rodgers, 2001: Urban form and thermal efficiency. *Journal of the American Planning Association* 67(2), 186-198.

Streutker D.R., 2002: A remote sensing study of the urban heat island of Houston, Texas. *International Journal of Remote Sensing* 23(13), 2595-2608.

Suits. G.H., 1983: The Nature of Electromagnetic Radiation. *Chapter 2 in Manual of Remote Sensing.* American Society of Photogrammetry. Falls Church, VA.

Tayanc, M. and H. Toros, 1997: Urbanization effects on regional climate change in the case of four large cities of Turkey. *Climate Change* 6(1), 59-69.

Terjung, W.H. and S.S-F. Louie, 1973: Solar radiation and urban heat islands. *Annals of the Association of American Geographers* 63(2), 181-207.

_____, 1976: Climatology for geographers. *Annals of the Association of American Geographers* 66(2), 199-222.

Torok, S. J., C.J.G. Morris, C. Skinner, and N. Plummer, 2001: Urban heat island features of southeast Australian towns. *Australian Meteorological Magazine* 50(1), 1-13.

Tou, J.T. and R.C. Gonzalez, 1974: *Pattern Recognition Principles.* Addison-Wesley. Reading, Mass.

Tso, C.P., 1996: A survey of urban heat island studies in two tropical cities. *Atmospheric Environment* 30(3), 507-519.

Unger, J., Z. Sumeghy, A. Gulyas, Z. Bottyan, and L. Mucsi: 2001: Land-use and meteorological aspects of the urban heat island. *Meteorological Applications* 8(2), 189-194.

Viterito, A., 1991: Future warming for United States cities. *Population and Environment* 13(2), 101-111.

Voogt J.A. and T.R. Oke, 2003: Thermal remote sensing of urban climates. *Remote Sensing of Environment* 86(3), 370-384.

Vukovich, F.M.,1983: An analysis of the ground temperature and reflectivity pattern about St. Louis, Missouri, using HCMM satellite data. *Journal of Climate and Applied Meteorology* 22(4), 560-571.

Weng, Q.H., 2001: A Remote Sensing-GIS evaluation of urban expansion and its impact on surface temperature in the Zhujiang Delta, China. *International Journal of Remote Sensing* 22(10), 1999-2014.

_____, 2003: Fractal analysis of satellite-detected urban heat island effect. *Photogrammetric Engineering and Remote Sensing* 69(5), 555-566.

_____, D.S. Lu, and J. Schubring, 2004: Estimation of land surface temperature-vegetation abundance relationship for urban heat island studies. *Remote Sensing of Environment* 89(4), 467-483.

_____, and S.H Yang, 2004: Managing the adverse thermal effects of urban development in a densely populated Chinese city. *Journal of Environmental Management* 70(2), 145-156.

Wong, K.K. and R.A. Dirks, 1978: Mesoscale perturbations on air-flow in urban mixing layer. *Journal Of Applied Meteorology* 17(5), 677-688.

Xu H.Q. and B.Q. Chen, 2004: Remote sensing of the urban heat island and its changes in Xiamen City of SE China. *Journal of Environmental Sciences-China* 16(2), 276-281.

Yamashita, S. and K. Sekine, 1991: Some studies on the earth's surface conditions relating to the urban heat island. *Energy and Buildings* 15(1-2), 279-288.

_____, K. Sekine, M. Shoda, K. Yamashita, and Y. Hara, 1986: On relationships between heat island and sky view factor in the cities of Tama River basin, Japan. *Atmospheric Environment* 20(4), 681-686.

Yang, L.M., 2000: Integration of a numerical model and remotely sensed data to study urban/rural land surface climate processes. *Computers and Geosciences* 26(4), 451-468.

Zhao M. and X.M. Zeng, 2002: A theoretical analysis on the local climate change induced by the change of landuse. *Advances in Atmospheric Sciences* 19(1), 45-63.

Zhou, L.M., R.E. Dickinson, Y.H. Tian, J.Y. Fang, Q.X. Li, R.K. Kaufmann, C.J. Tucker, R.B. Myeni, 2004: Evidence for a significant urbanization effect on climate in China. *Proceedings of the National Academy of Sciences of the United States of America* 101(26), 9540-9544.

VITA

Lynn Copeland Hardegree earned a Bachelor of Science degree in meteorology from the University of South Alabama in 1996. She earned a Master of Science in geography at the University of Alabama in 1998. She is currently a Physical Scientist with the United States Army Corps of Engineers and is assigned to the Engineering Infrastructure Intelligence Reachback Center within the Mobile District, Mobile, Alabama.